Extended x-ray absorption fine structure—its strengths and limitations as a structural tool

P. A. Lee, P. H. Citrin, P. Eisenberger, and B. M. Kincaid

Bell Laboratories, Murray Hill, New Jersey 07974

The authors review the development of extended x-ray absorption fine structure (EXAFS) within the last decade. Advances in experimental techniques have been largely stimulated by the availability of synchrotron radiation. The theory of EXAFS has also matured to the point where quantitative comparison with experiments can be made. The authors review in some detail the analysis of EXAFS data, starting from the treatment of raw data to the extraction of distances and amplitude information, and they also discuss selected examples of applications of EXAFS chosen to illustrate both the strength and limitations of EXAFS as a structural tool.

CONTENTS

I. INTRODUCTION

The term extended x-ray absorption fine structure (EXAFS) refers to oscillations of the x-ray absorption coefficient on the high-energy side of an absorption edge. Such oscillations can extend up to 1000 eV above the edge and may have a magnitude of 10% or more. As an example, the absorption spectrum near the K edge in crystalline Ge is shown in Fig. 1. The phenomenon of EXAFS has been known for about half a century, and the basic physical explanation has been provided by Kronig, who says that these oscillations are due to modification of the final state of the photoelectron by the crystal (Kronig, 1931) or, in the case of gaseous molecules, by atoms surrounding the excited atom (Kronig, 1932). However, when this field was last reviewed in this journal (Azaroff, 1963), a great deal of confusion still existed over the question of whether a long-range order theory formulated in

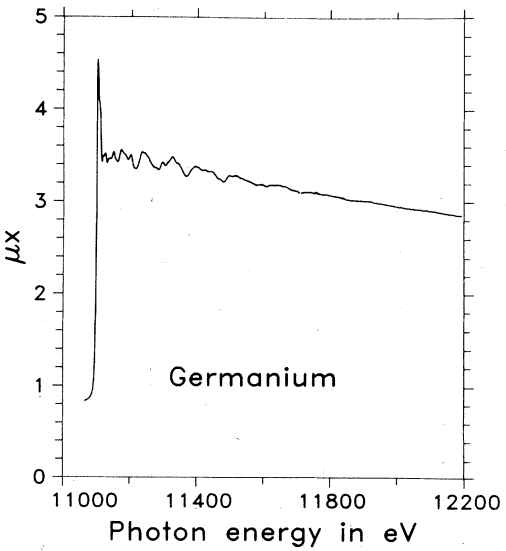

FIG. 1. X-ray absorption spectrum of crystalline germanium at a temperature of 100 K. The sharp rise in μ near 11 keV is the K edge and the modulation in μ above the edge is the EXAFS.

terms of Bloch waves (Kronig, 1931) or a short-range order theory in terms of scattering by neighboring atoms (Kronig, 1932, Hartree *et al.*, 1934, Shiraiwa *et al.*, 1958) is more appropriate. A major source of the confusion was that quantitative comparison between theory and experiment was nonexistent.

Over the past few years a dramatic improvement in our theoretical understanding of EXAFS has occurred. As we shall see, it is now established that a single scattering short-range order theory is adequate under most circumstances. The oscillatory part of the absorption coefficient $\Delta\mu$, normalized to the structureless (atomlike) background μ_0, is given by

$$\chi(k)=\frac{\Delta\mu}{\mu_0}=-\sum_j \frac{N_j}{kr_j^2}|f_j(k,\pi)| \times \sin[2kr_j+\psi_j(k)]e^{-2\sigma_j^2k^2}e^{-2r_j/\lambda_j(k)} \tag{1.1}$$

for excitations of an *s state* in a system in which the orientation of the sample has been *spherically averaged.* Equation (1.1) describes the modification of the photoelectron wave function at the origin due to scattering by N_j neighbors located at a radial distance r_j away. This is illustrated in Fig. 2 where the outgoing wave is shown backscattered by a neighboring atom. The backscattering amplitude is given by

$$f(k,\pi)=|f(k,\pi)|e^{i\phi(k)} = \frac{1}{2ik}\sum_l (2l+1)(e^{2i\delta_l}-1)(-1)^l, \tag{1.2}$$

where $\delta_l(k)$ are the scattering phase shifts. The photoelectron wave vector k is defined as

$$k=\hbar^{-1}[2m(\hbar\omega-E_0)]^{1/2}, \tag{1.3}$$

where ω is the x-ray frequency and E_0 is the threshold energy. It is clear that the electron wave will be phase shifted by $2kr_j$ by the time it makes the return trip to the neighbor. To this we must add the total phase function $\psi_j(k)$ given by

$$\psi_j(k)=\phi_j(k)+2\delta_1'(k). \tag{1.4}$$

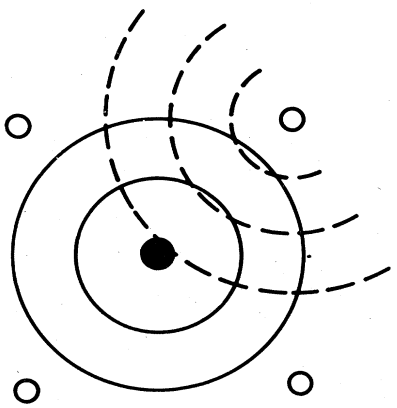

FIG. 2. Outgoing photoelectron waves (solid lines) propagate to neighboring atoms represented by open circles. The backscattered waves (dashed lines) modify the wave function at the central atom and give rise to EXAFS.

The first term $\phi_j(k)$ is the phase shift due to the backscattering from the jth neighboring atom as defined in Eq. (1.2), while the second term is twice the central-atom phase shift $\delta_1'(k)$ to account for the potential of the central atom through which the $l=1$ photoelectron wave (excited from an $l=0$ state) has traversed (the prime denotes that the central atom is photoexcited and is, in general, different from the neutral neighbor). The wave function at the origin is modulated according to this total phase factor and this accounts for the sinusoidal term in Eq. (1.1). In addition, we have to account for the fact that the atoms are not stationary. Thermal vibrations will smear out the EXAFS oscillations, and in the harmonic approximation this can be accounted for by a Debye-Waller-type term $\exp(-2\sigma_j^2k^2)$. Finally, electrons that have suffered inelastic losses will not have the proper wave vector to contribute to the interference process. This is crudely accounted for by an exponential damping term $\exp[-2r_j/\lambda_j(k)]$. It is the limited range of the photoelectrons in the energy region of interest (50–1000 eV) imposed by this damping term which permits a short-range order description of EXAFS even in crystalline materials.

The renewed interest in EXAFS within the last several years began with the work of Sayers, Stern, and Lytle (1971). They emphasized that if EXAFS can be described by Eq. (1.1), it should be possible to invert the problem and obtain the distances r_j from an analysis of EXAFS data. In particular, they performed a Fourier transform in k space of EXAFS data on crystalline and amorphous Ge and showed that peaks in the transform correspond to various atomic shells. The advantages of EXAFS versus conventional x-ray diffraction are obvious, and indeed some of the features were already appreciated by Hartree *et al.* (1934). EXAFS permits the determination of the local structure of each individual atomic species. Single crystals are not required. Applications that immediately come to mind are complicated biological molecules, alloys and amorphous materials, solution chemistry, catalysts, etc. At the same time, however, it is also clear that before EXAFS can be established as a viable structural tool, certain problems must first be overcome. We see from Eq. (1.1) that in order to go from the data to distances r_j, it is essential to have information on the k dependence of the phase shift ψ and, to a lesser extent, information on the backscattering amplitude $|f(k,\pi)|$ and the Debye-Waller and inelastic loss factors. Furthermore, there is the important question of the extent to which different distances can be resolved by EXAFS analysis. A discussion of the progress towards answering these questions makes up the bulk of this review.

So far we have discussed only the theoretical question of data analysis. In the past few years there has also been a dramatic improvement on the experimental side. EXAFS requires a continuously tunable x-ray source. The conventional source has been the bremsstrahlung background from x-ray tubes, and an EXAFS spectrum of statistics suitable for accurate distance determinations may require several weeks of data accumulation. Synchrotron radiation in the x-ray

range has become available and proves to be the ideal source for EXAFS experiments. As demonstrated in studies of Br_2, $GeCl_4$, and Cu, the $\sim 10^5$ increase in photon flux means that most conventional spectra can be taken in a matter of minutes (Kincaid and Eisenberger, 1975; Kincaid, Eisenberger, and Sayers, unpublished). Since that time there has been an explosion in the amount of data available in both simple and complicated systems. In particular, detailed studies of simple systems with known distances have enabled the phase shifts $\psi(k)$ to be extracted experimentally, which are then used to predict distances with an accuracy of <0.02 Å (Citrin *et al.*, 1976). Such data have, in turn, inspired considerable theoretical work so that quantitative comparison between theory and experiment can now successfully be made (Lee and Beni, 1977).

The outline of this review is as follows. In Sec. II the recent advances in experimental techniques, particularly with regard to synchrotron radiation, are described. In Sec. III we review the theory of EXAFS, and discuss in considerable detail the basic ingredients of the theory and the comparison of calculated spectra with experiments. Section IV is a thorough account of the analysis of EXAFS data, leading to phase shift and distance determinations. In Sec. V we review a number of examples of recent applications of EXAFS. A complete bibliography of EXAFS-related research is not attempted; the field has grown too large and crosses too many disciplines for that to be a fruitful endeavor. Rather, a number of examples are chosen to illustrate the successes, as well as the limitations, of EXAFS as a structural tool. In Sec. VI we review some related techniques and promising developments.

II. EXAFS EXPERIMENTAL TECHNIQUES

In the 1930's x-ray absorption spectra were taken in transmission with low-power conventional tubes, a dispersive Bragg spectrometer, and film as a detector (Kossel, 1920; Kronig, 1931, 1932). Very few measurements were made in the 1940's and 1950's. In the late 1960's the measurement of x-ray absorption spectra was revived, this time using modern counting and automation techniques (Lytle, 1966). The replacement of conventional x-ray tubes with synchrotron radiation signaled the beginning of rapid changes and variations in measurement techniques (Kincaid and Eisenberger, 1975; Kincaid, Eisenberger, and Sayers, unpublished). A transmission technique utilizing a channel-cut monochromator and ion chamber was developed, followed shortly by the development of a fluorescence technique based on a solid-state detector (Jaklevic *et al.*, 1977), and then one based on an array of scintillation and solid-state detectors. In 1976 a new mirror-monochromator system was developed which provided an increased factor of 30 in flux and about 300 in intensity. This system made possible the first successful study utilizing Auger electron detection for surface science studies (Citrin *et al.*, 1978). Very recently a new graphite crystal array detection system was developed by Hastings *et al.* (1979) which extended the limit of EXAFS experiments on dilute systems by an order of magnitude—or potentially two. An improved version of the fluorescence technique through the use of absorption filters to decrease the scattering background has also been successfully developed (Stern and Heald, 1979). The synchrotron-related developments have been responsible for the renewed interest in conventional rotating anode x-ray sources coupled with curved crystal monochromators to perform laboratory-based transmission experiments (Knapp *et al.*, 1978). In this section we describe each of the aforementioned experimental developments in x-ray absorption measurements since 1972 and compare their strengths and weaknesses for specific types of studies.

A. Description of experimental techniques

In Fig. 3 a schematic generalized experimental apparatus is shown to illustrate the various components comprising an x-ray absorption experiment.

1. Sources

A general review of various photon sources is already available (Brown, 1974; Haensel and Kunz, 1967; Lea, 1978; Winick, 1980), so we concentrate here only on how they impact on EXAFS measurements. The two sources of continuous x radiation used for EXAFS studies are the bremsstrahlung output from a rotating anode x-ray tube and the synchrotron radiation produced from electron storage rings or synchrotrons (the output from a synchrotron is less desirable because of its varying characteristics with

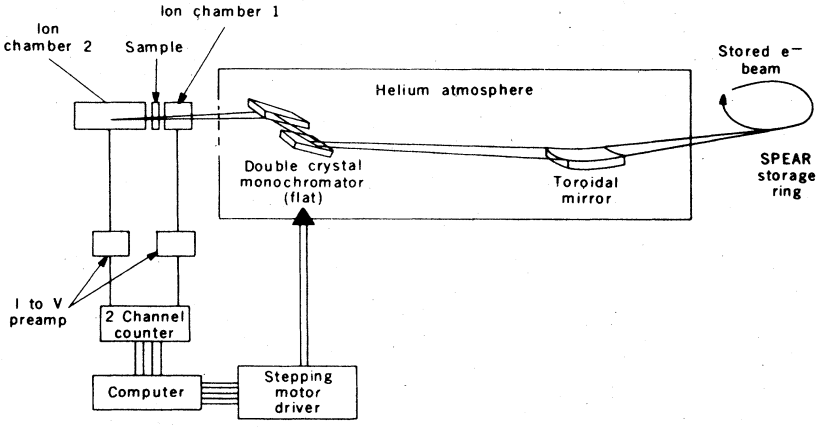

FIG. 3. Schematic apparatus for an x-ray absorption experiment.

time). A comparison of the outputs available from rotating anode sources and storage rings is given in Fig. 4.

Several characteristics of this figure deserve mentioning. Even though the brightness of synchrotron radiation is of the order 10^6 greater than that of bremsstrahlung radiation, it is not immediately obvious that the fluxes available for actual experiments are that much larger. For example, at the Stanford synchrotron many experiments are performed with only about 1 mrad^2 of radiation due to both the large collimation of the beam and the long distance from the experimental apparatus to the source. Using bent crystal optics with bremsstrahlung radiation, as much as 100–1000 mrad^2 can be collected and thus the 10^6 greater brightness of synchrotron radiation is reduced to only a 10^3–10^4 flux enhancement. On the other hand, rotating anode sources are now near their limit in output power due to heat limitations in the target, while new or existing storage ring sources are being designed or modified for flux enhancements by as much as 10^2–10^4. This increase will come from higher stored currents in dedicated storage rings, from collection of larger horizontal divergences with focussing mirrors, and from utilization of coherent wigglers (Kincaid, 1977; Winick, 1980). Thus the theoretical factor of 10^5–10^6 between identical experiments with the two different sources should, in fact, be realistic. Today, with the Stanford synchrotron running at 3 GeV and using a mirror to collect 6 mrad of horizontal divergence, about 10^{11} photons/sec eV are obtained in the 7 keV energy region. In the future about 10^{15} photons/sec eV should be possible.

In addition to considerations of flux there is also the question of radiation purity. The spectrum of radiation from a storage ring is very smooth, while that from an x-ray tube contains characteristic lines originating from the target material and contaminants. These can seriously deteriorate the quality of certain EXAFS measurements.

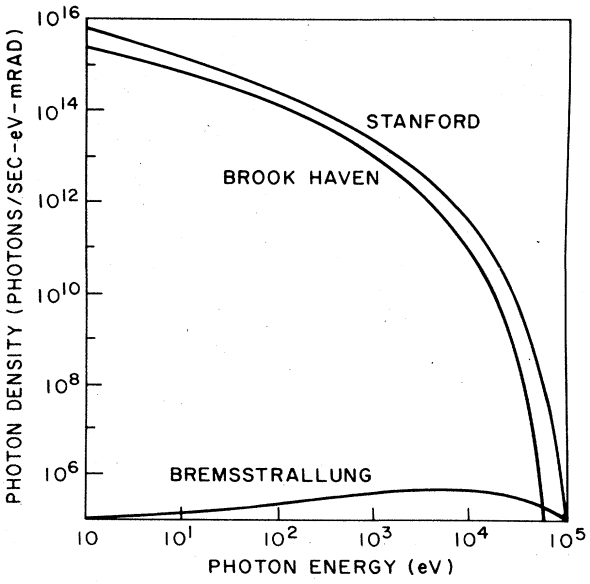

FIG. 4. Comparison between rotating anode x-ray source and synchrotron storage ring.

In spite of the obvious disadvantages of flux and purity, however, there are two offsetting factors that make conventional sources extremely attractive. The first is that even with the considerably lower photon fluxes provided by conventional sources, approximately 10^8 photons/sec in a 10 eV bandwidth, this is still adequate for high concentration studies. The second factor is that conventional sources are readily accessible and available for continuous experimentation while synchrotron sources are sparsely distributed and available for the general scientific community on only a limited basis.

A succinct assessment of the above comparison, then, is that studies of systems which are dilute and/or complex and/or which require particularly high accuracy (large k range) are best performed with synchrotron radiation, while studies of concentrated systems can easily be performed using bremsstrahlung radiation.

2. Monochromators

In general, the two optical elements used for monochromatization in the x-ray region are single crystals and mirrors. Mirrors, generally curved, are used to focus the radiation and to change the angular and spatial characteristics of the beam. They operate on the basis of total external reflection. The index of refraction at x-ray frequencies is approximately given by

$$n = 1 - \delta = 1 - \frac{\lambda^2 e^2}{\pi m c^2} \sum_a N_a Z_a = 1 - \frac{\omega_p^2}{\omega^2}, \tag{2.1}$$

where Z_a is the number of electrons on atom a for which there are N_a such atoms per unit volume. Total external reflection at a given energy will occur for all angles less than the critical angle θ_c. From Snell's law we have

$$\cos\theta_c = 1 - \delta \quad \text{or} \quad \theta_c = \sqrt{2\delta}, \tag{2.2}$$

which for $\delta \sim 10^{-6}$ implies a $\theta_c \sim 10^{-3}$ rad. At a given angle $\theta < \theta_c$ there is a high energy "cutoff" given by

$$\hbar\omega_c = \frac{\hbar\omega_p}{\theta}. \tag{2.3}$$

Below that cutoff energy the reflectivity can be as high as 80–90%. The high energy cutoff can make mirrors useful as low pass filters. Because of the small angular range of total external reflection the radius of curvature is quite large. Also, the finite angular range makes mirrors more useful for the highly collimated synchrotron radiation than for conventional x-ray sources. The first application of a mirror with synchrotron radiation is described by Horowitz and Howell (1976). Since that time mirrors have been successfully utilized by others.

Bragg crystal spectrometers can be used in a variety of configurations, each of them characterized by a different emittance (James, 1965; Hastings, 1977; Deslattes, 1980). We briefly describe the parallel double-crystal spectrometer, which is the configuration most frequently used for current sychrotron research. A schematic diagram is shown in Fig. 5. The type of crystal deter-

mines the efficiency and resolution of the spectrometer. There are two general classes of crystals, mosaic and perfect, and as of this writing only the latter have been used. A perfect crystal can be characterized by a Darwin reflection width $\delta\theta_\omega$ and an efficiency ϵ, which in most cases is greater than 90% for highly collimated monochromatic radiation. When used for EXAFS research on a storage ring, the inherent collimation of the radiation $\delta\theta_r$ is typically greater than $\delta\theta_\omega$. The general set of equations describing the performance of a perfect parallel crystal spectrometer with Bragg plane spacing d and a vertical scattering plane is

$$\lambda = 2d\sin\theta_B ,$$

$$\frac{\Delta\lambda}{\lambda} = \frac{\Delta E}{E} = \cot\theta_B \delta\theta_r \quad \text{if } \delta\theta_r > \delta\theta_\omega ,$$

$$\delta\theta_\omega = \frac{2n\lambda^2 F e^2}{\pi \sin 2\theta_B mc^2} ,$$

$$\frac{I_r}{I_0} = \epsilon \frac{\delta\theta_\omega}{\delta\theta_r} \quad \text{for } \delta\theta_r > \delta\theta_\omega , \tag{2.4}$$

where λ is central wavelength reflected when the beam makes the angle θ_B with the Bragg planes. The resolution $\Delta\lambda/\lambda$ is determined (to leading order) by the angular range of incident radiation in the plane of scattering, and the extinction width $\delta\theta_\omega$ is determined by the scattering power F of the crystal. The fraction of incident radiation within the bandwidth $\Delta\lambda$ that is reflected, I_r/I_0, is determined both by the efficiency ϵ of the reflection and by the acceptance mismatch $\delta\theta_\omega/\delta\theta_r$. This last factor is due to photons arriving with wavelength λ but at an angular deviation from θ_B greater than $\delta\theta_\omega$. Since $\delta\theta_r$ is $\sim 3\times 10^{-4}$ rad and $\delta\theta_\omega$ is typically 5×10^{-5}, an order of magnitude of intensity is lost from this mismatch. Mosaic crystals are a possible approach towards reducing such losses. These crystals reflect over a larger angular range $\delta\theta_\omega$ at the expense of their efficiency's being lower because of larger photon penetration depths (greater absorption losses). Initial uses of such crystals have not been successful, due most probably to the increased loss (i.e., lower ϵ) of mosaic crystals. In the future either crystals with a larger $\delta\theta_\omega$ (i.e., InSb or W), slightly curved crystals, or mirrors should be used to correct the current factor of 5–10 mismatch which exists between $\delta\theta_\omega$ and $\delta\theta_r$. In particular, curved crystals offer the possibility of greater collection efficiency without a loss in resolution.

The resolution required for EXAFS is not very great.

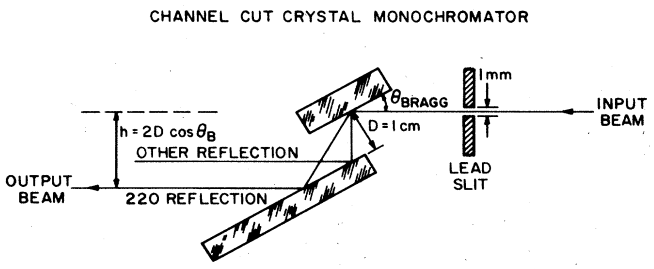

FIG. 5. Illustration of a channel-cut crystal monochromator.

For typical measured distances r less than 5 Å, the energy separation between peaks, given approximately by

$$2r\Delta k = \pi ,$$
$$\Delta E\ (\text{eV}) \sim 7k\Delta k\ (\text{Å}^{-1}) , \tag{2.5}$$

is 5 eV at $k = 2$ Å^{-1} and 25 eV at $k = 10$ Å^{-1}. Since for most systems the r accessible to EXAFS analysis is no greater than ~3 Å and generally data with $k > 3$ Å are analyzed, the smallest energy separation between peaks is about 15 eV. To avoid distortions in the data a resolution no poorer than ~5 eV should be used. Inadequate resolution may have serious effects on the analysis of more distant shells, a problem which has been discussed by Lengeler and Eisenberger (1980). On the other hand, it does not pay to have much higher resolution since such studies have not revealed additional structure. Also, higher resolution necessarily results in a smaller photon flux. Ultimately structure on a fine energy scale will be broadened by the core hole decay rate which varies from fractions of an eV for light atoms to tens of eV for heavy ones (see Sec. III.D).

A second reflection either in the form of a monolithic channel-cut crystal or an independent second crystal (see Fig. 5) is used to insure that the monochromatized beam always propagates in the same direction as the incident beam. This scheme results in a vertical displacement between the monochromatized and the incident beam of $h = 2D\cos\theta_B$. To keep the samples centered on the beam, therefore, it need only be translated small distances if D is small (typical values are 1 cm). Recently, more ingenious schemes for two crystal spectrometers with fixed entrance and exit beam positions have been designed (Cerino *et al.*, 1980; Golovchenko *et al.*, 1981).

One advantage of two independent crystals over a channel-cut crystal is that the second reflection can be slightly mistuned from the first. This technique can be used to diminish the higher harmonics because of the narrower Darwin width of the higher order reflections.

The double crystal spectrometer is most often used with synchrotron radiation because of the source's well defined collimation. Conventional x-ray sources, which are divergent and are thus about 10^6–10^9 less bright, require curved crystal spectrometers because radiation over solid angles as large as 0.1 steradians can be collected. Discussion of the different resolution and intensity criteria for curved crystals is given by Berreman (1979).

3. Sample chamber

Two general considerations in the design of an EXAFS sample chamber are the small size of the signal compared to the background absorption and the preservation of the sample's chemical integrity during the course of the measurement. Both dictate great care in sample preparation, characterization, and positioning. To accommodate the wide variety of samples that are measured with EXAFS, Dewars, ovens, pressure vessels, high vacuum chambers, flow chambers, and gas cells are generally standard parts of an experi-

mental apparatus. The use of such equipment in EXAFS is not significantly different from their use in other experiments. The only special criteria for consideration are (a) low-loss coupling of the photon beam to the sample and (b) the detector (see next section). Since photoabsorption varies approximately as $Z^4\lambda^3$, a low Z window is desirable. Beryllium is usually the first choice, but in some applications Kapton is acceptable. Teflon can also be used for study of reactive materials (it is available in films bonded to Kapton). At sufficiently low photon energies (< 3 keV) even the thinnest self-supporting window is too strongly absorbing and direct coupling of the experimental chamber to the beam port is necessary.

The requirements of size, thickness, and other physical and chemical properties of the sample vary greatly depending upon whether transmission, fluorescence, or other detection schemes are used. In the next section we describe these detection schemes and their sample requirements more fully, but for now we make one general comment. The smallness of the EXAFS signal with respect to the total absorption requires that systematic effects be minimized, and the most likely cause for this is sample inhomogeneity. Even if all beam harmonics are removed and the sample tracks the beam perfectly, the intensity distribution across the beam can change due to competing reflections or monochromator inhomogeneities. For an inhomogeneous sample, this change in incident beam intensity is manifested as an absorption fluctuation. Various powdering techniques or dried solutions are often used to produce homogeneous samples. These considerations are most severe for transmission measurements and become particularly troublesome when studying dilute, low Z atoms in nonmetallic (nonrollable) materials such as biological proteins. The K edge absorption length for monoatomic samples is nearly constant, requiring thicknesses for transmission experiments of about 10^{-3} cm. However, for Fe in hemoglobin, samples up to 1 mm thick can be used due to the weak absorption of the low Z atoms of the protein at the Fe absorption wavelength. For Ca in a protein, on the other hand, thicknesses of 10^{-2} to 10^{-3} cm are required and this greatly increases the difficulty of obtaining a uniform sample.

4. Detectors

The goal of an x-ray absorption experiment is to measure the absorption of the sample as a function of energy. This can be accomplished in several ways, either directly by measuring the attenuation of the incident beam in a transmission experiment, or indirectly by measuring the products of absorption, namely, the fluorescent radiation or the nonradiative Auger or secondary electrons. Generally speaking, transmission is advantageous for concentrated samples where one is, so to speak, weighing very precisely the ship with and without the captain. For dilute systems, in which the precision of the measurement is limited by the number of absorbing atoms, the "captain" is weighed directly by selectively measuring the absorption by-product of the constituent atom of interest. Considerations of signal-to-noise ratio for the various techniques is given in the next section.

Regardless of detection scheme, it is necessary to measure the incident intensity in order to remove the effect of a varying source intensity. This must be done in a manner that depletes only a small fraction of the incident intensity. Ion chambers have so far been the universal choice in the x-ray regime. Filled with a gas or mixture of gases contained by two thin windows, an ion chamber works on the principle of measuring photoion current. It is thus best suited for high signal level experiments. The ion chamber also has the desirable feature of being able to have its gas mixture readily adjusted such that either the incident or transmitted detector's absorption is optimum.

The measurement of secondary products requires a separate detector capable of selecting only those products characteristic of the atom of interest. Discrimination against unwanted products is usually done on the basis of energy. For the case of fluorescent photons a scintillation detector, a nondispersive solid-state detector, either of the two with an absorption filter, or a combination of a curved crystal analyzer and a scintillation detector is used. The respective resolution of the scintillation, solid-state, and crystal detector at 8 keV is approximately 2 keV, 200 eV, and 20 eV. Two other important parameters for describing the effectiveness of these various approaches are the solid angle acceptance and the data rate capability. Arrays of scintillators, solid-state detectors, or crystals can be used to increase the solid angle, with cost being the main limitation. The data rate capacity of the individual detectors is approximately 200 000 counts/sec for the scintillation detectors, 40 000 counts/sec for the solid-state detector, and essentially unlimited for the crystal. For any of these photon counting schemes the data accumulation rate on any individual detector should not exceed the electron bunch repetition frequency ($\sim 10^6$/sec) of the storage ring in order to avoid two photons arriving within a single synchrotron radiation pulse. This form of saturation ultimately limits the simple photon counting approach. For presently realized data rates this has so far not posed a serious problem. With (future) increased data rates the problem of saturation can be remedied simply by increasing the number of detectors. Also, more elaborate electronic counting schemes (fast integrators) could surmount the pulse repetition problem.

Detection of the Auger or secondary electron by-products of the absorption process requires a high vacuum environment and an electron detector. The detector can be either an energy analyzer or a secondary electron multiplier, the former giving higher resolution and the latter generally giving larger solid angle detection. Electron multipliers are suitable for total and partial secondary electron yield detection, while energy analyzers are best suited for Auger electron measurements. Both systems are susceptible to saturation due to limitations in data rate capabilities and, as with the case of photon detectors, this problem can be overcome. Both systems require separate measurement of the incident photon intensity. If the sample under study has an absorption edge $\gtrsim 3$ keV, the vacuum system can be isolated from the storage ring with a Be

window and a conventional ion chamber can be used. If the absorption edge is $\lesssim 3$ keV, a separate electron multiplier system mounted near a high transmission grid coated with an element of smoothly varying absorption in the energy region of interest can be used to monitor the incident flux.

B. Signal-to-noise evaluation of the different detection schemes

The development of a wide variety of experimental approaches for measuring EXAFS has arisen from the almost limitless range of samples that can be studied. These include gases, solids, or liquids containing absorbing atoms of either high or low Z which are distributed either uniformly in thin or thick (bulk) samples or nonuniformly in thin (surface) layers supported by bulk material. In this section we first discuss in general terms each of the various EXAFS detection schemes according to their application to uniform and nonuniform samples and then consider which approach is best suited for representative examples.

With a source of brightness B in photons/sec eV mrad^2 mm^2 and a mirror-monochromator system with a bandwidth $\Delta E(E)$, a solid angle collection of $\delta\Omega$ onto an area A with an efficiency $\epsilon(E)$ (including absorption in the transport system), the photon flux I_0 incident on the first detector is given by

$$I_0(\text{photons/sec}) = B\Delta E(E)\delta\Omega A\epsilon(E) . \tag{2.6}$$

The detector measuring I_0 (usually an ion chamber) absorbs a small fraction of the incident intensity such that the photon flux detected by the first ion chamber (with gas mixture of thickness x and absorption μ) is given by

$$I_d = I_0(1 - e^{-(\mu x)_d}) , \tag{2.7}$$

while the flux hitting the sample is given by

$$I_{\text{inc}} = I_0 e^{-(\mu x)_d} . \tag{2.8}$$

To cancel out fluctuations of the source all measurements are made as a ratio of the signal (transmitted, fluorescent, or nonradiative intensity) to I_d. Except in transmission the signal-to-noise ratio is not significantly affected by I_d but rather by the statistics of the much smaller fluorescent or nonradiative signal. For simplicity we therefore assume that I_d has no noise for the fluorescent and nonradiative detection schemes (modifications introduced by considering its contribution to the noise are described). The fraction I_d/I_0, which optimizes a given type of experiment, is also specified. Finally, we initially assume that the fluorescence and nonradiative experiments are performed without contribution from any background signal.

The above discussion ignores the existence of "glitches" in the ratio of the signal to I_{inc}. These glitches are due to multiple Bragg reflections being satisfied simultaneously. In most cases the amplitude change remains after taking the ratio of the signal and I_{inc} because of differences in the two detection channels (i.e., speed of detectors, beam positioning, etc.). For two identical detection channels a glitch can still arise because the multiple reflection changes the frequency spectrum of the "monochromatic" beam due to the fact that different reflections are not centered at the same energy. Thus there is a dispersive aspect to glitches in addition to amplitude changes. If the ratio has a slope as a function of energy, the dispersive effect will cause a derivativelike glitch.

1. Uniform sample

For a uniform sample the total absorption coefficient can be divided into the absorption of the atom of interest μ_A and that of the other atoms μ_B, such that

$$\begin{aligned} \mu_T &= \mu_A + \mu_B , \\ \mu_A &= N_A\sigma_A(E) , \\ \mu_B &= \sum_i N_i\sigma_i(E) . \end{aligned} \tag{2.9}$$

Here N_i is the concentration in atom/cm^3 of the ith atomic species and σ is the atomic absorption cross section in cm^2. Only μ_A is expected to have structure in the energy region being studied.

a. Transmission

For a sample of thickness X the intensity of transmitted photons detected by the second ion chamber is given by

$$I_t(\text{photons/sec}) = I_{\text{inc}} e^{-\mu_T X} . \tag{2.10}$$

The *total* signal is the ratio I_d/I_t. Since we are only interested in the contribution of μ_A, specifically the modulations $\Delta\mu_A$ which carry the structural information, we write the EXAFS signal as

$$S = \frac{\partial(I_d/I_t)}{\partial\mu_A}\Delta\mu_A = \Delta\mu_A X\frac{I_d}{I_t} . \tag{2.11}$$

The noise is simply given by

$$\begin{aligned} N &= \frac{I_d}{I_t}\left[\left(\frac{\Delta I_d}{I_d}\right)^2 + \left(\frac{\Delta I_t}{I_t}\right)^2\right]^{1/2} \\ &= \frac{I_d}{I_t}\left(\frac{1}{I_d} + \frac{1}{I_t}\right)^{1/2} , \end{aligned} \tag{2.12}$$

with the resulting signal-to-noise ratio for a one second integration time being

$$\frac{S}{N} = \Delta\mu_A X I_0^{1/2}\left(\frac{1}{1 - e^{-(\mu x)_d}} + \frac{1}{e^{-\mu_T X}e^{-(\mu x)_d}}\right)^{-1/2} . \tag{2.13}$$

Maximizing the signal-to-noise ratio with respect to $(\mu x)_d$ and $\mu_T X$, we obtain

$$(\mu x)_d = 0.245 , \quad \mu_T X = 2.55 , \tag{2.14}$$

which yields

$$\frac{S}{N} = 0.556\,\frac{\Delta\mu_A}{\mu_T} I_0^{1/2} . \tag{2.15}$$

Had we ignored the fluctuations of I_d, the result would be (with $\mu_T X = 2$)

$$\frac{S}{N} = 0.736\,\frac{\Delta\mu_A}{\mu_T} I_{\text{inc}}^{1/2} . \tag{2.16}$$

Since in practice $I_0 \approx I_{\text{inc}}$, we shall ignore fluctuations in I_d for the rest of the section.

b. Fluorescence

For the case of a uniform sample we assume that it is infinitely thick and that the incident and fluorescent beams enter and leave the front surface symmetrically, i.e., at 45°. The intensity of fluorescent radiation in the second detector with solid angle acceptance $\Omega/4\pi$ is given by

$$I_f = \frac{I_{\rm inc}\epsilon_f(\Omega/4\pi)\mu_A(E)}{\mu_T(E)+\mu_T(E_f)}, \tag{2.17}$$

where ϵ_f is the fluorescence yield, E is the energy of the incident photon, and E_f is the characteristic fluorescence energy. The EXAFS signal is again the variation in μ_A and is given by

$$S = \frac{\partial(I_f/I_d)}{\partial\mu_A}\Delta\mu_A = \frac{I_{\rm inc}}{I_d}\left(\frac{\epsilon_f(\Omega/4\pi)\Delta\mu_A}{\mu_T(E)+\mu_T(E_f)}\right). \tag{2.18}$$

The noise, ignoring the contribution of I_d and background, is given simply by

$$N = \frac{\sqrt{I_f}}{I_d}. \tag{2.19}$$

The S/N is then

$$\frac{S}{N} = \left(\frac{I_{\rm inc}\epsilon_f(\Omega/4\pi)\mu_A(E)}{\mu_T(E)+\mu_T(E_f)}\right)^{1/2}\frac{\Delta\mu_A}{\mu_A}. \tag{2.20}$$

Unless the fluorescence signal approaches the incident intensity, the noise of I_d is negligible. Typical I_d/I_f ratios are greater than 10^3 for thick samples, so for I_d/I_0 between 0.1 and 0.01 the S/N will not be measurably affected. The background arising from quasielastic and inelastic scattering processes can be reduced by the use of an absorption filter or a crystal detector, or by energy discrimination of the photon detector. As the dilution of absorbing atoms increases, and depending upon the detection scheme chosen, the background intensity I_b could exceed the fluorescence signal, whereby the S/N deteriorates to

$$\frac{S}{N} = \left(\frac{I_{\rm inc}\epsilon_f(\Omega/4\pi)\mu_A(E)}{\mu_T(E)+\mu_T(E_f)}\right)^{1/2}\frac{\Delta\mu_A}{\mu_A}\left(\frac{1}{1+I_b/I_f}\right)^{1/2}. \tag{2.21}$$

In the limit when $I_b \gg I_f$ this reduces to

$$\frac{S}{N} = \left(\frac{I_{\rm inc}\epsilon_f(\Omega/4\pi)\mu_A(\epsilon)}{\mu_T(E)+\mu_T(E_f)}\right)\frac{\Delta\mu_A}{\mu_A}I_b^{-1/2}. \tag{2.22}$$

c. Nonradiative

Considerations about nonradiative (Auger and secondary electron) detection are the same as for fluorescence except that here the sampling depth is not determined by $[\mu_T(E)+\mu_T(E_f)]^{-1}$ but rather is limited by the Auger and secondary electron escape depths, which are typically much smaller. Denoting the exponential attenuation of the nonradiative signal by $n(E)$ and the nonradiative yield by $\epsilon_n(=1-\epsilon_f)$, we obtain

$$\frac{S}{N} = \left(\frac{I_{\rm inc}\epsilon_n(\Omega/4\pi)\mu_A(E)}{\mu_T(E)+n(E)}\right)^{1/2}\frac{\Delta\mu_A}{\mu_A}. \tag{2.23}$$

The S/N can be slightly improved by going to an asymmetric geometry, i.e., the angle of incidence being smaller than the angle of nonradiative detection. The same considerations as applied to the fluorescence case concerning background hold for the nonradiative detection experiment, resulting in

$$\frac{S}{N} = \left(\frac{I_{\rm inc}\epsilon_n(\Omega/4\pi)\mu_A(E)}{\mu_T(E)+n(E)}\right)^{1/2}\left(\frac{\Delta\mu_A}{\mu_A}\right)\left(\frac{1}{1+I_b/I_n}\right)^{1/2}. \tag{2.24}$$

2. Nonuniform sample

The simplest example of a nonuniform sample is a thin film of thickness X with absorption of interest μ_A supported on a flat substrate of thickness X_B with background absorption μ_B. For the fluorescence and nonradiative detection schemes this problem can be treated for any value of X_B since only a background is contributing to the total signal, but for transmission the signal of interest is attenuated by the substrate and thus the problem is no longer general. How thin the substrate is, i.e., how much the substrate absorbs relative to the thin film, therefore quite sensitively determines the signal-to-noise.

a. Transmission

From simple extension of Sec. II.B.1.a above, and ignoring the noise contribution from I_d, we obtain

$$\frac{S}{N} = \mu_A X e^{-\mu_A X/2} I_{\rm inc}^{1/2} e^{-\mu_b X_b/2}\left(\frac{\Delta\mu_A}{\mu_A}\right), \tag{2.25}$$

where μ_b is the (background) absorption coefficient of the substrate. In the limit $\mu_A X \ll 1$, we obtain

$$\frac{S}{N} = \mu_A X e^{-\mu_b X_b/2} I_{\rm inc}^{1/2}(\Delta\mu_A/\mu_A). \tag{2.26}$$

b. Fluorescence

The general expression for the fluorescence signal strength (again ignoring fluctuations in I_d) of arbitrary sample thickness X is given by

$$I_f = I_{\rm inc}\frac{\epsilon_f(\Omega/4\pi)\mu_A(E)}{\mu_A(E)+\mu_A(E_f)}(1-e^{-[\mu_A(E)+\mu_A(E_f)]X}). \tag{2.27}$$

In the small thickness limit this reduces to

$$I_f = I_{\rm inc}\epsilon_f(\Omega/4\pi)\mu_A(E)X. \tag{2.28}$$

Including the background contribution I_b from the substrate, the signal-to-noise ratio becomes

$$\frac{S}{N} = \left(\frac{I_{\rm inc}\epsilon_f(\Omega/4\pi)\mu_A(E)X}{(1+I_b/I_f)}\right)^{1/2}\frac{\Delta\mu_A}{\mu_A}. \tag{2.29}$$

c. Nonradiative

For the thin film regime and the same conditions as assumed for the fluorescence case above, Eq. (2.29) applies (with I_f replaced by I_n), so long as $n(E)X \ll 1$.

C. Comparison of different detection schemes

A summary of the previous sections is given in Tables I and II. It is obviously beyond the scope of this work to consider all the possible variations of parameters that would determine in a particular case which technique to use and whether or not it would have sufficient sensitivity to perform the desired experiment. Nevertheless, various general trends can be described.

We first focus on the uniform case for transmission

TABLE I. Signal-to-noise ratio for various experiments.

	Uniform sample	Nonuniform sample ($\mu_A X \ll 1$)
transmission	$0.736\frac{\mu_A(E)}{\mu_T(E)}\left(\frac{\Delta\mu_A(E)I_{\rm inc}^{1/2}}{\mu_A(E)}\right)$	$\epsilon^{-\mu_b X_b/2}\mu_A(E)X\,\frac{\Delta\mu_A(E)I_{\rm inc}^{1/2}}{\mu_A(E)}$
fluorescence	$\left(\frac{\epsilon_f(\Omega_f/4\pi)\,\mu_A(E)}{(1+I_b/I_f)[\mu_T(E)+\mu_T(E_f)]}\right)^{1/2}\left(\frac{\Delta\mu_A(E)I_{\rm inc}^{1/2}}{\mu_A(E)}\right)$	$\left(\frac{\epsilon_f(\Omega_f/4\pi)\mu_A(E)X}{1+I_b/I_f}\right)^{1/2}\left(\frac{\Delta\mu_A(E)I_{\rm inc}^{1/2}}{\mu_A(E)}\right)$
nonradiative	$\left(\frac{\epsilon_n(\Omega_n/4\pi)\,\mu_A(E)}{(1+I_b/I_n)[\mu_T(E)+n(E)]}\right)^{1/2}\left(\frac{\Delta\mu_A(E)I_{\rm inc}^{1/2}}{\mu_A(E)}\right)$	$\left(\frac{\epsilon_n(\Omega_n/4\pi)\mu_A(E)X}{(1+I_b/I_n)}\right)^{1/2}\left(\frac{\Delta\mu_A I_{\rm inc}^{1/2}}{\mu_A}\right)$

versus fluorescence and nonradiative detection. Generally speaking, and assuming (I_b/I_f or I_b/I_n)<1, if the total efficiency of the fluorescence or electron detector $\epsilon\Omega/4\pi$ is greater than μ_A/μ_T, the transmission technique is not preferred. More specifically, for a given efficiency we can determine the absorbing atom concentration at which the fluorescence or nonradiative approaches become more favorable. For simplicity we consider only fluorescence. For $Z=20$ to $Z=100$, ϵ_f ranges between 0.1 and 1 (it is essentially 1 for $Z>50$). For a modest value of $\Omega_f/4\pi\sim10^{-2}$, the fluorescence signal-to-noise ratio is greater than that of transmission when $\mu_T/\mu_A>10^2$–10^3 (this depends on the Z of the atom). Since

$$\frac{\mu_T}{\mu_A}=\frac{N_B\sigma_B}{N_A\sigma_A}\,, \tag{2.30}$$

we have for the simple case $\sigma_B=\sigma_A$ that at greater than 10^{-2}–10^{-3} dilution the fluorescence approach is preferred. For a low Z atom in a high Z material, $\sigma_B>\sigma_A$, and fluorescence is even more favorable at such concentrations. The converse is true for the case of a high Z atom in a low Z material. This is often encountered in biological studies in which a transition metal like Fe in hemoglobin has an absorption σ_A about 100 times the background absorption σ_B due to the N, O, and C atoms. In that case dilutions of 10^{-4} to 10^{-5} are required before fluorescence is preferred.

The nonradiative detection scheme for (thick) uniform samples suffers greatly from the fact that the exponential attenuation of electrons $n(E)$ is so large. A crude expression for $n(E)$ is

$$n(E)\ (\mathrm{cm}^{-1})=2\times10^8[E(\mathrm{eV})]^{-1/2}\,, \tag{2.31}$$

which gives attenuation lengths of 5 Å at 100 eV and 50 Å at 10^4 eV. For a mean value of $n(E)=5\times10^6$ cm^{-1} and $\mu_T=1000$ cm^{-1} the nonradiative technique becomes advantageous over fluorescence only if the dilution factors is about 10^3–10^4 less than that desirable for fluorescence. Even for low Z atoms where $\epsilon_f/\epsilon_n\ll1$ it is unlikely that the nonradiative technique will be useful for thick dilute samples. However, for concentrated low Z systems electron detection might be favorable over transmission due to the difficulty of preparing a uniform sample of sufficient thickness (see Sec. II.B.1.c).

The above discussion assumed (I_b/I_f or I_b/I_n)$\ll1$. As this assumption breaks down, i.e., as the absorbing atom concentration becomes so small in the uniform thick sample that the background contribution is no longer negligible, the secondary detection schemes lose their advantage over transmission and the EXAFS experiment becomes very difficult. Which detection scheme to use in such a situation depends upon the details of the particular system. Generally speaking, as the concentration of the absorbing atoms in a thick uniform sample decreases, the choice of desired technique will change from fluorescence using a scintillator, to scintillator using a filter, to solid-state detector using a filter, and finally (in the most dilute case) to the crystal array.

We now turn our attention to a (thin) nonuniform sample such as the case of an overlayer on a substrate. Simply ignoring the substrate contribution in transmission, i.e., $\mu_b X_b\cong0$ (this is often not possible in practice), and again assuming (I_b/I_f or I_b/I_n)$\ll1$, we have the condition that for typical values of $\epsilon_n\Omega_n/4\pi$ or $\epsilon_f\Omega_f/4\pi$ of about 10^{-2}–10^{-3}, $\mu_A X$ must be less than 10^{-2}–10^{-3} in order for the fluorescence or nonradiative techniques to be advantageous over transmission. For Fe $\mu_A\sim2000$ cm^{-1}, and we determine that for X less than 10^{-5}–10^{-6} cm the fluorescence approach will be preferred over transmission. As already mentioned, the attenuation of the nonradiative signal is so strong that the sample cannot be considered to be thin until X is less than ≈20 Å. For samples thinner than 20 Å the

TABLE II. Signal-to-noise ratio for various detection schemes.

Ratio	Uniform sample	Nonuniform sample
$\frac{\text{fluorescence}}{\text{transmission}}$	$\left(\frac{\epsilon_f(\Omega_f/4\pi)\mu_T(E)}{1.08\mu_A(E)(1+I_b/I_f)}\right)^{1/2}$	$\left(\frac{\epsilon_f(\Omega_f/4\pi)e^{\mu_b X_b}}{\mu_A(E)X(1+I_b/I_f)}\right)^{1/2}$
$\frac{\text{nonradiative}}{\text{transmission}}$	$\left(\frac{\epsilon_n(\Omega_n/4\pi)\mu_T^2(E)}{0.54n(E)\mu_A(E)(1+I_b/I_n)}\right)^{1/2}$	$\left(\frac{\epsilon_n(\Omega_n/4\pi)e^{\mu_b X_b}}{\mu_A(E)X(1+I_b/I_f)}\right)^{1/2}$
$\frac{\text{fluorescence}}{\text{nonradiative}}$	$\left(\frac{\epsilon_f\Omega_f\,[\mu_T(E)+n(E)](1+I_b/I_n)}{\epsilon_n\Omega_n\ 2\mu_T(E)(1+I_b/I_f)}\right)^{1/2}$	$\left(\frac{\epsilon_f\Omega_f\,(1+I_b/I_n)}{\epsilon_n\Omega_n\,(1+I_b/I_f)}\right)^{1/2}$

choice of nonradiative versus fluorescence detection will depend upon whether $\epsilon_f\Omega_f$ is greater or less than $\epsilon_n\Omega_n$.

Having decided which technique to use, the researcher must next decide whether or not there is adequate S/N to perform the desired experiment. Current storage rings have a sufficiently large I_0 to permit the doing of any transmission EXAFS experiment in principle. The only question to consider is the minimum concentration of absorbing atoms that can be analyzed using the fluorescence or nonradiative detection scheme. With an I_0 of 10^{11} photons/sec currently available at the Stanford synchrotron, a value of $\epsilon_f\Omega_f/4\pi$ or $\epsilon_n\Omega_n/4\pi$ of 10^{-3}, and assuming a value of $\Delta\mu_A/\mu_A = 10^{-2}$, a concentration of $N_A\sigma_A/N_B\sigma_B = 10^{-4}$ is sufficient to achieve an S/N of 1:1 in one second. This concentration is roughly an order of magnitude smaller than the minimum value at which fluorescence is preferable over transmission (i.e., for the same value of the detector efficiency). In particular, for the case of Fe in a protein where $\sigma_A/\sigma_B \sim 100$, we have $N_A/N_B \sim 10^{-6}$ or $N_A \sim 10^{17}/\text{cm}^3$, which is in the millimolar concentration regime. For the case of a thin nonuniform sample and again assuming $I_0 = 10^{11}$ photons/sec, $\epsilon\Omega/4\pi = 10^{-3}$, and $\Delta\mu_A/\mu_A = 10^{-2}$, we have from Table I that $\mu_A X = 10^{-4}$ is sufficient to give $S/N = 1$ in one second. Since μ_A is about 1000 cm^{-1}, monolayer and submonolayer concentrations are indeed feasible with longer counting time.

Of course the assumption of $\Delta\mu_A/\mu_A = 10^{-2}$ limits the range in k over which a signal can be obtained, and there are situations when greater accuracy is undoubtedly required. Nevertheless, the above discussion adequately represents the general features of the various techniques.

III. THEORY OF EXAFS

A. The basic EXAFS formula

In the introduction we indicated that the single scattering formula for EXAFS, Eq. (1.1), could be derived intuitively by considering the scattering of photoelectron waves from surrounding atoms back towards the excited atom at the origin. Sayers *et al.* (1971) derived this formula by assuming that the atoms are point scatters. More formal derivations based on Green's function and generalization to muffin-tin scattering potentials can be found in Ashley and Doniach (1975) and Lee and Pendry (1975). Schaich (1973) has made a careful comparison of the short-range and long-range order theories based on Bloch waves in crystalline materials. He concluded that the two are formally identical provided inelastic damping effects are taken into account. It seems clear that since EXAFS is an interference effect involving the final-state wave function, it is the modulation in the matrix element that is important, and not the density of states (Stern, 1974). While a long-range order theory is possible in principle, in practice it requires calculations of all possible matrix elements and is prohibitively expensive, particularly for increasing photoelectron energy.

In this section we outline an alternative derivation of the EXAFS formula that is physically more transparent (Lee, 1976). Consider a situation in which a single neighbor is located at $\mathbf{r}_1$ relative to the atom that absorbed the x-ray. The probability of emitting an electron in the direction $\hat{k}$ is given by

$$P(\hat{k}) = D\left|\hat{\epsilon}\cdot\hat{k} + \frac{f(\theta)}{r_1}e^{ikr_1(1-\cos\theta)}\hat{\epsilon}\cdot\hat{r}_1\right|^2. \tag{3.1}$$

In this equation $\hat{\epsilon}$ is the polarization direction of the x-ray and D is a proportionality constant. As illustrated in Fig. 6(a) the two terms in Eq. (3.1) describe the interference of the direct beam with the beam that propagates first to $\mathbf{r}_1$ and is then scattered through the angle θ (the angle between $\hat{k}$ and $\hat{r}_1$) with scattering amplitude $f(\theta)$. The difference in the interference path length is $r_1(1-\cos\theta)$. Now, if we integrate over all $\hat{k}$, we should get the total absorption coefficient. While this is not immediately apparent, it can be explicitly demonstrated as follows. The nontrivial term is the cross term, which we write as

$$\int\frac{d\hat{k}}{4\pi}\left(\hat{\epsilon}\cdot\hat{k}\,\frac{f(\theta)}{r_1}e^{ikr_1(1-\cos\theta)}\,\hat{\epsilon}\cdot\hat{r}_1 + \text{c.c.}\right)$$

$$= 2\,\text{Re}(e^{ikr_1}\hat{\epsilon}\cdot\hat{r}_1 I/r_1), \tag{3.2}$$

where

$$I = \int\frac{d\hat{k}}{4\pi}\,\hat{\epsilon}\cdot\hat{k}e^{-ikr_1\cos\theta}f(\theta). \tag{3.3}$$

We choose $\hat{r}_1$ to be the z axis and use the identity

$$\hat{\epsilon}\cdot\hat{k} = \sum_m\frac{4\pi}{3}\,Y^*_{1m}(\hat{k}\cdot\hat{r}_1)Y_{1m}(\hat{\epsilon}\cdot\hat{r}_1). \tag{3.4}$$

The azimuthal angle integration is straightforward, leaving the $m=0$ term alone:

$$I = \hat{\epsilon}\cdot\hat{r}_1\tfrac{1}{2}\int d\cos\theta\cos\theta e^{-ikr_1\cos\theta}f(\theta). \tag{3.5}$$

This integration can be done using the standard expansions

$$e^{-ikr_1\cos\theta} = \sum_l(2l+1)(-i)^l j_l(kr_1)P_l(\cos\theta) \tag{3.6}$$

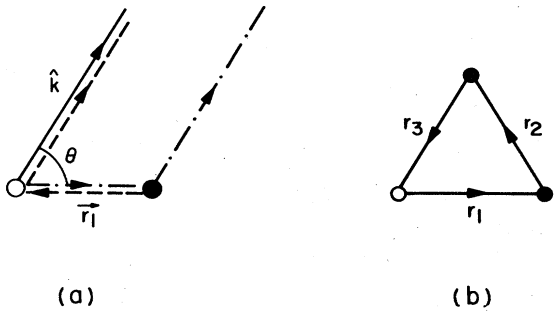

FIG. 6. (a) Interference between direct beam (solid line) from the absorbing atom (open circle) and (i) the beam (dash-dot line) scattered by the neighbor (closed circle located at $\mathbf{r}_1$ and (ii) the beam (dashed line) backscattered by the neighbor atom. Integration over the angle θ gives EXAFS and process (ii) is responsible for the appearance of the central atom phase shift $2\delta_1$ in the EXAFS formula. (b) Multiple-scattering contribution to EXAFS in which the photoelectron is scattered by two neighbors.

and

$$f(\theta)=\sum_l f_l P_l(\cos\theta), \tag{3.7}$$

where

$$f_l=\frac{1}{2ik}(2l+1)(e^{2i\delta_l}-1). \tag{3.8}$$

Then

$$I=\sum_l \hat{\epsilon}\cdot\hat{r}_1 i\,\frac{\partial}{\partial(kr_1)}[(-i)^l j_l(kr_1)]f_l. \tag{3.9}$$

We use the asymptotic form

$$j_l(kr)\to\frac{1}{kr}\sin(kr-\tfrac{1}{2}l\pi) \tag{3.10}$$

to obtain

$$I=\frac{\hat{\epsilon}\cdot\hat{r}_1}{kr_1}\frac{1}{2}i[f(k,\pi)e^{ikr_1}+f(0)e^{-ikr_1}]. \tag{3.11}$$

The first term produces $f(k,\pi)e^{2ikr_1}$ in the EXAFS formula. Interestingly, the second term is exactly cancelled by the square of the second term in Eq. (3.1) using the optical theorem

$$\mathrm{Im}f(0)=\frac{k}{4\pi}\int d\phi\, d\cos\theta|f(\theta)|^2, \tag{3.12}$$

with the final result that

$$\frac{\Delta\mu}{\mu_0}=-3\,\frac{(\hat{\epsilon}\cdot\hat{r}_1)^2}{kr_1^2}\,\mathrm{Im}[f(k,\pi)e^{2ikr_1}]. \tag{3.13}$$

The cancellation of the square term is important for the following reason. If we have more than one neighbor, the square term can in principle produce terms like $\exp[2ik(r_1-r_2)]$, etc. If these terms exist the EXAFS spectra will be enormously complicated. Fortunately, all these cross terms exactly vanish. While we have demonstrated it here only for the case with one neighbor, it can be shown more generally using the Green's function technique that such difference terms do not exist (Ashley and Doniach, 1975; Lee and Pendry, 1975). One way of understanding this cancellation is to note that the terms in question are second order in the scattering amplitude and that there are corrections to the same order in the normalization of the final-state wave function.

The above derivation of Eq. (3.12) can be found in Massey (1969) and is equivalent to the formula originally written down by Kronig (1932) and used by Shiraiwa *et al.* (1958). However, we now know that it is in error upon comparison with Eq. (1.1) because the central-atom phase shift $2\delta_1'$ is missing. The importance of the central-atom phase shift was recognized by Kostarev (1941) and Kozlenkov (1961) and was incorporated in a point-scattering theory by Sayers *et al.* (1971). In our present way of looking at the problem it is clear in the above derivation that the direct beam and the scattered beam suffer the same phase shift δ_1', which is *cancelled* in calculating the interference path length. We can regain this term only by going to a higher order scattering process. Specifically, it is the process shown in Fig. 6(a), whereby the electron goes out to the atom at $\mathbf{r}_1$, is backscattered by the neighbor, and is scattered again by the central atom in the direction $\hat{k}$. This probability amplitude is given by

$$A_2(\hat{k})=\hat{\epsilon}\cdot\hat{r}_1\,\frac{e^{2ikr_1}}{r_1^2}\,f(k,\pi)f'(k,2\pi-\theta), \tag{3.14}$$

where f' is the scattering amplitude by the central atom. This term must be added to the amplitude in Eq. (3.1) and then squared. The leading term involves a product of $\hat{\epsilon}\circ\hat{k}$ with A_2, which upon integration over all $\hat{k}$ directions projects out only the $l=1$ component of the scattering amplitude f'. Using Eq. (3.8), we obtain the following additional contribution to the probability

$$P_2=-\mathrm{Im}\left((e^{2i\delta_1'}-1)f(k,\pi)\,\frac{e^{2ikr_1}}{kr_1^2}\right). \tag{3.15}$$

This term combines with Eq. (3.13) to give us back exactly the central-atom phase shift, so that

$$\chi(k)=-3\,\frac{(\hat{\epsilon}\cdot\hat{r}_1)^2}{kr_1^2}\,\mathrm{Im}[e^{2ikr_1+2i\delta_1'}f(k,\pi)]. \tag{3.16}$$

B. Multiple scattering: EXAFS versus other techniques

Now that EXAFS has been reduced to the problem of the scattering of photoelectrons by atoms, we are led to draw comparisons with low-energy electron diffraction (LEED) in which an electron beam with energy of several hundred eV is scattered by a crystal. Indeed, EXAFS is similar to LEED except that the electron source and detector are at the same point—the central atom (also, the EXAFS source emits spherical rather than plane waves). This immediately raises the question of the adequacy of the single scattering description for EXAFS, since it is well known that multiple scattering is very important in the interpretation of LEED data (Jona, 1977). We see in deriving Eq. (3.16) that the EXAFS formula already includes one particular multiple-scattering correction, i.e., that involving the central atom. The reason for including this particular one is that this is the only process with the phase factor $2kr_1$. In fact, it has been shown (Lee and Pendry, 1975) that each multiple-scattering process can be described by an effective interference path length equal to the sum of the scattering paths. For example, the double scattering process shown in Fig. 6(b) is characterized by the path length $r_1+r_2+r_3$, rather than $2r_1$, as for the single scattering process. In general, these path lengths are long and involve (highly unlikely) successive large-angle scattering events. In k space they give rise to rapidly oscillating terms which tend to average out. It is only very near the absorption edge that multiple scattering (band-structure effects) becomes important. This is because at low energy the scattering becomes more isotropic and the electron mean free path becomes very long. However, the near-edge structure is usually discarded in EXAFS analysis. Alternatively, if we Fourier transform the data, the multiple-scattering contributions will show up farther out in the transformed spectrum. In particular, these contributions will have no influence on the nearest-neighbor distance. It is for these reasons that multiple scattering is much less important in

EXAFS than in LEED.

It is worth pointing out, however, one special case where multiple scattering is important in EXAFS. It was found that the fourth shell in the Cu EXAFS has an anomalously large amplitude and phase shift. The explanation is that in an fcc lattice a nearest-neighbor atom is directly in the line of sight of the fourth-shell atom. The outgoing electron is strongly forward scattered, thereby enhancing the electron amplitude in the fourth shell (Lee and Pendry, 1975). This effect, which can be likened to an amplifying relay system, has also been observed in Mo EXAFS from $Mo(CO)_6$ and $Mo(NCS)_6^{3-}$ (Cramer, Hodgson, Steifel, and Newton, 1978), in Ni EXAFS from the molecule nickel carbonyl, $Ni(CO)_4$ (Teo, 1981), and has been used to detect the presence of Br_3 complex in doped $(SN)_x$ polymer (Morawitz *et al.*, 1979).

Our derivation of Eq. (3.16) also brings out the relation between EXAFS and angular resolved photoemission from core states. Liebsch (1974) has proposed that angular resolved photoemission from the core state of an adsorbed atom may be a good way of determining adsorbate structure. This experiment is intermediate between EXAFS and LEED in that the electron source is the adsorbate atom, whereas the detector is outside the sample. The angular dependence of the photoemission from the 1*s* level of O adsorbed on Cu(001) (Kono *et al.*, 1978) and from the core levels of Te and Na adsorbed on Ni(001) (Woodruff *et al.*, 1978) have been reported. Theoretical calculation of the angular dependence is complicated by the fact that the angular pattern changes with photoelectron energy and is therefore sensitive to the scattering potential, a problem made more serious at the relatively low photoelectron energies at which the data are available. The energy dependence of the photoemission normal to the surface has also been measured [Kevan *et al.* (1978); Williams *et al.* (1979)]. Initially these experiments were believed to be more similar to LEED in that multiple-scattering corrections are essential to the interpretation of the data (Liebsch, 1976). However, recent work by Li and Tong (1979) indicates that for photoelectron energy above 50 eV or so, the normal emission spectrum can be well described by a single backscattering (EXAFS-like) process plus multiple-scattering corrections in the forward direction. Such a simplification of the theory, together with the structural sensitivity of the technique, may turn normal photoemission into a more useful surface structural tool.

It is worth mentioning that the angular average of the photoemission from an adsorbate is *not* EXAFS. This is because the adsorbed atom is in an intrinsically asymmetric situation, with all the neighboring atoms on one side. The averaging can be done at most only over 2π steradians outside the sample, which clearly is not equivalent to a 4π average. Lee (1976) has looked at the photoemission process from the viewpoint of summing interference paths. With a single exception, the path lengths are given by the radial distance plus a projection which gives rise to oscillations quite different from the $2kr$ oscillations in EXAFS. The single exception is the scattering event shown in Fig. 6(a) where the electron is backscattered towards the adsorbed atom. While the oscillation period is $2kr$, the phase shift is not $2\delta_1'$ as in EXAFS. It is, rather, the phase of the scattering amplitude f', which in general involves phase shifts in all the angular momentum channels. As of this writing, there has not been a systematic experimental study of this question on adsorbed systems.

C. *L* edge spectra

So far we have discussed photoexcitation of only an *s*-state electron. Excitation from a *p* state or from any other state is more complicated. The general formula for excitation of an L_0-core state is given by (Lee and Pendry, 1975; Lee, 1976)

$$\chi(k) = \sum_j \sum_{m_0 L L''} N_j 4\pi \langle L_0|\hat{\epsilon}\cdot\mathbf{r}|L''\rangle Y^*_{L''}(-\hat{r}_j) Y_L(\hat{r}_j) \langle L|\hat{\epsilon}\cdot\mathbf{r}|L_0\rangle i^{l''-l} \times \sin[2kr_j + \delta_l'(k) + \delta_{l''}'(k) + \phi_j(k)] |f_j(k,\pi)| \frac{e^{-2\sigma_j^2 k^2} e^{-2r_j/\lambda_j(k)}}{kr_j^2} \left(\sum_{m_0}\sum_{L} |\langle L_0|\hat{\epsilon}\cdot\mathbf{r}|L\rangle|^2\right)^{-1}, \tag{3.17}$$

where we have used the notation $L_0 = (l_0, m_0)$. This describes the excitation of a L_0 state to an outgoing wave with angular momentum L which propagates in the direction $\hat{r}_j$ with probability amplitude $Y_L(\hat{r}_j)$. It is backscattered and the reflected wave is expanded in spherical harmonics about the origin with amplitude $Y^*_L(-\hat{r}_j)$. We note that the backscattering amplitude $|f(k,\pi)|$ and phase $\phi(k)$ do not depend on whether we have *K*- or *L*-shell excitation. We also point out that we can simplify Eqs. (3.17) using the identity

$$Y_{L''}(-\hat{r}) = (-1)^{l''} Y_{L''}(\hat{r}) = (-1)^{l_0+1} Y_{L''}(\hat{r}).$$

For $l_0 = 0$ this accounts for the negative sign in front of Eq. (1.1). This $(-1)^{l_0+1}$ factor has its origin in the convention chosen for the definition of the scattering phase shift $\delta_l(k)$.

Let us focus on the excitation of *p* states, for which the final state can be $l = 0$ or 2. It is convenient to choose $\hat{\epsilon}$ to be the *z* axis, in which case $m' = m'' = m_0$. The matrix element $\langle L|\hat{\epsilon}\cdot\mathbf{r}|L_0\rangle$ has an angular part which integrates to a simple number and a radial part which depends on the particular atomic level. [We should remark that in many cases spin-orbit coupling is important and the initial states are split according to $j = \frac{3}{2}$ and $j = \frac{1}{2}$. However, if we assume that the photoelectron spin is not changed by the scattering process with the atom, it can be shown that summing over the j_z initial state for either $j = \frac{3}{2}$ or $j = \frac{1}{2}$ is equivalent to taking $l_0 = 1$ and summing over the initial m_0 values, as is done in Eq. (3.17)]. Heald and Stern (1977) noted that $\chi(k)$ is by definition a second rank tensor and the angular dependence cannot be more complicated than $\cos^2\theta$. By performing the m sum they obtain

$$\chi(k)=\sum_j N_j \frac{|f_j(k,\pi)|\,e^{-2\sigma^2k^2}}{kr_j^2} e^{-2r_j/\lambda_j(k)}\{\tfrac{1}{2}(1+3\cos^2\theta_j)M_{21}^2\sin[2kr_j+2\delta_2'(k)+\phi_j(k)]+\tfrac{1}{2}M_{01}^2\sin[2kr_j+2\delta_0'(k)+\phi_j(k)]$$
$$+M_{01}M_{21}(1-3\cos^2\theta_j)\sin[2kr_j+\delta_0'(k)+\delta_2'(k)+\phi(k)]\}(M_{21}^2+\tfrac{1}{2}M_{01}^2)^{-1}, \quad (3.18)$$

where M_{01} and M_{21} are the radial dipole matrix elements between the $l=1$ atomic wave function and the $l=0$ and $l=2$ final states. The first and second terms in Eq. (3.18) correspond to transitions to $l=2$ and $l=0$ final states, respectively. The third term is a cross term originating from the possibility of having an outgoing $l=2$ state and an incoming $l=0$ state and vice versa. Unlike the K edge, the dipole matrix elements do not cancel and three sets of phase shifts are involved. Fortunately, some simplifications are possible. For polycrystalline samples the third term in Eq. (3.18) vanishes upon angular integration. The ratio of the matrix elements M_{01}/M_{21} has been calculated (Teo and Lee, 1979) to be of order 0.2 and relatively independent of photoelectron energy. The physical reason for a small M_{01} is that the final state is orthogonal to the 1s core state and is therefore rapidly oscillatory in the region of the $2p$ wave function. The calculated value agrees with the value 0.2 ± 0.06 reported by Heald and Stern (1977) based on the angular dependence of the W L_3 edge in single-crystal WSe_2. Thus for polycrystalline samples the p-to-d transition dominates over the p-to-s transition by a factor of 50. As a result, the $L_{2,3}$ edges can be analyzed using a simple formula like Eq. (1.1), except that $\delta_1'(k)$ must be replaced by $\delta_2'(k)$ and the overall minus sign must be removed.

Lytle, Sayers, and Stern (1977) analyzed the Fourier-transformed EXAFS of the W $L_{2,3}$ edges and interpreted the observed splitting of the peaks as being due to the different k dependences of $\delta_0'(k)$ and $\delta_2'(k)$ in the first two terms in Eq. (3.18). The above discussion indicates that the p-to-s transition is unobservably small. The splitting of the peak is, rather, due to the k-dependent structures of the backscattering amplitudes of heavy elements (Teo and Lee, 1979).

D. Lattice vibration, disorder, and lifetime

Next we consider the effect of lattice vibrations. This effect was first discussed by Schmit (1961) and has since been treated more completely by Beni and Platzman (1976). EXAFS takes place on a time scale much shorter than that of atomic motion, so the measurement serves as an instantaneous snapshot of the atomic configuration. We must therefore perform an average over all such configurations. The instantaneous location of the atom is written as

$$\mathbf{r}_j=\mathbf{r}_j^0+\mathbf{u}_j, \quad (3.19)$$

where $\mathbf{r}_j^0$ is the equilibrium position taken to be zero for the central atom. Then

$$\langle e^{i2k|\mathbf{r}_j-\mathbf{r}_0|}\rangle \approx \langle e^{i2k\hat{r}_j^0\cdot(\mathbf{r}_j-\mathbf{r}_0)}\rangle$$
$$=e^{i2kr_j^0}\langle e^{i2k\hat{r}_j^0\cdot(\mathbf{u}_j-\mathbf{u}_0)}\rangle$$
$$=e^{i2kr_j^0}e^{-2k^2\sigma_j^2}, \quad (3.20)$$

where

$$\sigma_j^2=\langle[\hat{r}_j^0\cdot(\mathbf{u}_j-\mathbf{u}_0)]^2\rangle. \quad (3.21)$$

The last step in Eq. (3.20) follows for harmonic oscillators. As a result, Eq. (3.16) becomes

$$\chi(k)=-\sum_j N_j\frac{3(\hat{\epsilon}\cdot\hat{r}_1)^2}{kr_j^2}A_j(k)|f_j(k,\pi)|$$
$$\times\sin[2kr_j+2\delta_1'(k)+\phi_j(k)]e^{-2\sigma_j^2k^2}, \quad (3.22)$$

where N_j is the number of atoms in the jth shell and a factor $A_j(k)$ has been inserted to account for the losses due to inelastic scattering (discussed further below). Phenomenologically $A_j(k)$ is often written in the form $A_j(k)=A_0\exp[-2r_j/\lambda_j(k)]$.

The EXAFS Debye-Waller factor differs from the Debye-Waller factor for x-ray diffraction in an interesting way. It is the mean-square average of the difference of displacements and may, in general, be different from the mean-square displacement. Indeed,

$$\sigma_j^2(k)=\langle(\hat{r}_j^0\cdot\mathbf{u}_j)^2+(\hat{r}_j^0\cdot\mathbf{u}_0)^2\rangle-2\langle(\hat{r}_j^0\cdot\hat{u}_0)(\hat{r}_j^0\cdot\mathbf{u}_j)\rangle. \quad (3.23)$$

The last term is the correlation term and vanishes if the central atom and the scattering atom move independently. In covalently bonded systems the nearest neighbor is strongly bonded and such coherence effects are very important. For example, in the case of Ge a different Debye-Waller factor must be assigned to the first shell compared with other shells (Rabe *et al.*, 1979b). The Debye-Waller factor has been extracted by studying the temperature and the k^2 dependence of the logarithm of the EXAFS amplitude (Stern *et al.*, 1975) (see Sec. IV.F). The anisotropy in the Debye-Waller factor has also been studied for Zn (Eisenberger and Brown, 1979). Recently theoretical calculations of σ_j^2 have been made for Cu, Fe, and Pt crystals and compared with experiments (Sevillano *et al.*, 1979; Böhmer and Rabe, 1979).

For systems with strong disorder the above Gaussian treatment is inadequate. Considering each neighbor separately, the EXAFS expression (3.16) or (3.18) should be averaged over a pair-distribution function $G(r)$, giving

$$\chi(k)=-\frac{|f(k,\pi)|}{k}\int d\mathbf{r}\,3(\hat{\epsilon}\cdot\hat{r})^2\frac{G(\mathbf{r})e^{-2r/\lambda(k)}}{r^2}\sin[2kr+\psi(k)]. \quad (3.24)$$

For thermal disorder, $G(\mathbf{r})=C\exp[-u(\mathbf{r})/kT]$, where $u(\mathbf{r})$ is the interatomic potential and C is a normalization constant. Equation (3.22) is derived from Eq. (3.24) by taking the factor $\exp[-2r/\lambda(k)]/r^2$ outside the integral and replacing r by the average value r_j^0. Doing the averaging more properly (Eisenberger and Brown, 1979), even a harmonic $u(\mathbf{r})$ leads to an additional phase shift of the order $2\sigma^2(k)[1/r_j^0+1/\lambda(k)]k$. This gives an effective shift in the distance determination, which is usually small ($\lesssim0.01$ Å). More serious phase and amplitude corrections to Eq. (3.22) arise when the potential sampled in the averaging

deviates from being harmonic, e.g., when the hard-core repulsion is felt. The corrections are so large that for Zn a conventional analysis using the 20 K data as a model predicts an apparent 0.09 Å *contraction* of the nearest-neighbor distance at room temperature compared with the known 0.05 Å *expansion*. Eisenberger and Brown (1979) found that for Zn and Ag the discrepancy could be removed by correcting the phase shift up to order $k^3\langle x^3\rangle$, i.e., $\psi_j(k)$ in Eq. (1.1) is replaced by

$$\psi_j(k)=2\delta_1'(k)+\phi_j(k)+2k(2\langle x^2\rangle-\tfrac{1}{2}\langle y^2+z^2\rangle)\times[1/r_j^0+1/\lambda_j(k)]-\tfrac{8}{15}k^3\langle x^3\rangle\,, \tag{3.25}$$

where x is the distance fluctuation along the bond direction and y,z are perpendicular to the bond direction. Equation (3.25) is a reasonable approximation for $k^3\langle x^3\rangle \leq 1$. The work on Zn has been extended to include the liquid state by Crozier and Seary (1980). The effects of strong disorder are discussed further in Secs. IV and V.

In addition to the Debye-Waller factor, the finite lifetime of the hole state also smears out EXAFS. For the core states accessible by presently available x-ray sources this has not been a serious problem because the hole-state width Γ is at most a few eV. In principle, this effect is taken into account by convoluting the EXAFS formula with a Lorentzian of width Γ. There will be observable effects only if Γ is of the order of or larger than the spacings ΔE between the oscillations in energy space, where $\Delta E=(\partial E/\partial k)\Delta k=(k/m)/2r_j$. It is interesting to note that ΔE can also be written as $\Delta E=\hbar/\tau_j$, where τ_j has the interpretation of being the transit time for the photoelectron to make the round trip to the atom at $\mathbf{r}_j$. In terms of the viewpoint of angular resolved photoemission presented in Sec. II.B above, the criterion is that the lifetime of the system must be sufficiently long for the backscattered electron to interfere with the direct beam. For example, a 100 eV photoelectron (with velocity $\sim 6\times 10^{16}$ Å/sec) can travel a total of 42 Å ($=2r_j$) before a hole of width $\Gamma=1$ eV or lifetime of 7×10^{-16} sec decays; for $2r_j=6$Å, Γ must be ≤ 15 eV for interference to occur. At higher photoelectron energies, of course, Γ must be larger still.

E. Calculation of amplitude and phase functions

It is clear that a knowledge of the phase $\psi(k)=2\delta_1'(k)+\phi(k)$ is essential for obtaining distances from EXAFS data. In Sec. IV we review how $\psi(k)$ can be accurately determined by empirical means, and in view of the success of this approach it is appropriate to ask: Why even attempt to calculate these phase functions? From a purely theoretical point of view, it is desirable to know how well one can do, and there are good reasons to believe that the answer is very well. This is because photoelectrons in the energy range of interest, ~100–1000 eV, are scattered primarily by core electrons. Thus the distribution of the valence electrons, which vary according to the chemical environment, need not be taken into account very accurately. From a practical point of view, the central-atom phase shift $2\delta_1'(k)$ and the scattering phase $\phi(k)$ can be calculated separately, whereas experimentally only the combination can be measured. The calculations therefore allow phase shifts to be constructed for systems whose atom-pair phase shifts are difficult or impossible to obtain from model compound measurements.

There have been two methods for calculating electron-atom scattering phase shifts.

1. The Hartree-Fock (HF) method. Starting with the tabulated atomic wave function, the Hartree-Fock equation of the atom plus external electron system is solved by iteration. The external electron is allowed to exchange with the atomic wave functions, but the latter are held frozen. The external electron is expected to polarize the atom, but such correlation effects are not taken into account by this method.

2. The Hartree-Fock-Slater (HFS) method, or the local density functional approximation. The atom is replaced by an electron gas of varying density, allowing the exchange term to be replaced by the local potential

$$V(r)=-e^2\left(\frac{3}{\pi}\rho(r)\right)^{1/3}, \tag{3.26}$$

where $\rho(r)$ is the local density. This approximation has been well tested for low-energy electrons in band-structure calculations, and the general belief is that both exchange and correlation are taken into account. The difficulty with this approximation is that the potential $V(r)$ is assumed to be independent of the electron energy whereas in reality the exchange and correlation effects diminish as the photoelectron energy increases because the atomic electrons do not have time to respond to the fast external electron [see Hedin and Lundqvist (1969, 1971) for a review].

There have been calculations of EXAFS spectra based on both methods. The HF method was used by Lee and Pendry (1975), Kincaid and Eisenberger (1976), and Pettifer and McMillan (1977), while the HFS method has been used by Ashley and Doniach (1975) and by Lagarde (1976). Neither scheme provided very satisfactory results. One way to take the correlation effect into account is to calculate explicitly the polarization of the atom due to excitation of various core and valence levels (Beni *et al.*, 1976). This was carried out for Cu with some success. However, the calculations are too complicated to implement on a large scale. What is needed is a relatively simple scheme which interpolates between the low energy regime, where the HFS method has been tested, and the high-energy regime, where the HF approach is expected to be more reasonable. Such a scheme based on the local density functional formalism was introduced by Lee and Beni (1977). The basic idea is still to treat the atom as an electron gas with slowly varying density. At each radius the density $\rho(r)$ and the Fermi energy $E_F(r)$ are calculated from tabulated wave functions. If E is the kinetic energy of the electron, then locally the electron has a kinetic energy of

$$E_{\rm loc}(r)=E+E_F(r)\,. \tag{3.27}$$

This assumption is basically that of the Thomas-Fermi description of the atom. The self-energy $\Sigma_{\rm homo}$ of a

homogeneous electron gas of the local density is then calculated and identified with the exchange and correlation potential

$$U_{xc}(r,E)=\Sigma_{\text{homo}}(E_{\text{loc}}(r),\rho(r)). \tag{3.28}$$

The Schrödinger equation is solved to obtain a set of complex phase shifts. Note that this scheme produces an effective potential which is complex, i.e., inelastic effects are included and are dependent on the electron energy E.

The scattering amplitude is evaluated from the phase shifts using the standard formula. The absolute value $|f(k,\pi)|$ is shown in Fig. 7 for a variety of atoms. Note that for lighter atoms like C, $|f(k,\pi)|$ peaks at small k and becomes rather structureless, decreasing roughly like k^{-2} for higher k. For heavier atoms there is a peak at intermediate k due to resonance with some core electrons (i.e., some $l=0$, 1, or 2 phase shift goes through $\pi/2$). This has the same physical origin as the Ramsauer-Townsend effect at low energies (Mott and Massey, 1965). As the atomic number increases, these resonance features move to higher k. For even heavier elements like Pb, the amplitude clearly shows a two peaked structure. Such structure in the amplitude resembles beating between two distances and care must be taken not to confuse the two effects.

The phase $\phi(k)$ of the scattering amplitude is shown in Fig. 8. Note again the systematic variation with atomic number. The downturn of the phase function at low k is associated with the minimum in the amplitude shown in Fig. 7. In the complex plane the phase can vary more rapidly when the magnitude is small. This kink in the phase function is clearly observable in the analysis of heavy atoms like Pt and Au (Teo and Lee, 1979; Rabe *et al.*, 1979a) and moderately heavy atoms like Ag (Citrin *et al.*, 1978). In lighter atoms like Ge and Br, the downturn is at relatively small k where the accuracy of the theory is more suspect.

Finally, the central-atom phase shift is shown in Fig. 9. Note that it has a much stronger k dependence than $\phi(k)$. The choice of the atomic potential is complicated by the core relaxation problem. Once the core hole is created, the other atomic wave functions see an additional charge at the origin and they relax inward. This relaxation occurs on a time scale roughly given by the inverse of the binding energy of each of the outer wave functions. Without solving the full time-dependent potential problem, the argument leading to Eq. (3.16) suggests that we should use the potential appropriate for the time equal to the photoelectron transit time τ given by $\tau_j^{-1}=k/(m2r_j)$. For $k=16\,\text{Å}^{-1}$ ($E\sim900$ eV) and a nearest-neighbor distance of 2 Å, $\hbar\tau^{-1}\sim30$ eV. Thus we argue that all atomic levels bound by more than 30 eV will have sufficient time to relax in response to the core hole. In practice we have used the wave functions of a relaxed ion with a $1s$ hole to calculate our central-atom potential. The relaxation of the valence electrons and the similar question of screening by conduction electrons in metals is a more complicated question. We expect such effects will lead to differences in the potential of several eV, which will affect the phase shifts only for small k. Such errors are of the same order as the chemical

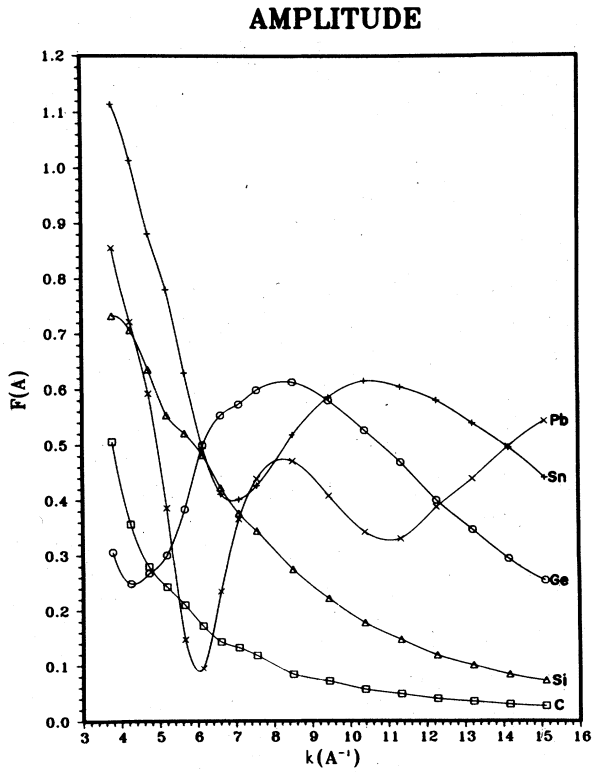

FIG. 7. Backscattering amplitude $F=|f(k\pi)|$ in Å vs k for a number of elements (from Teo and Lee, 1979).

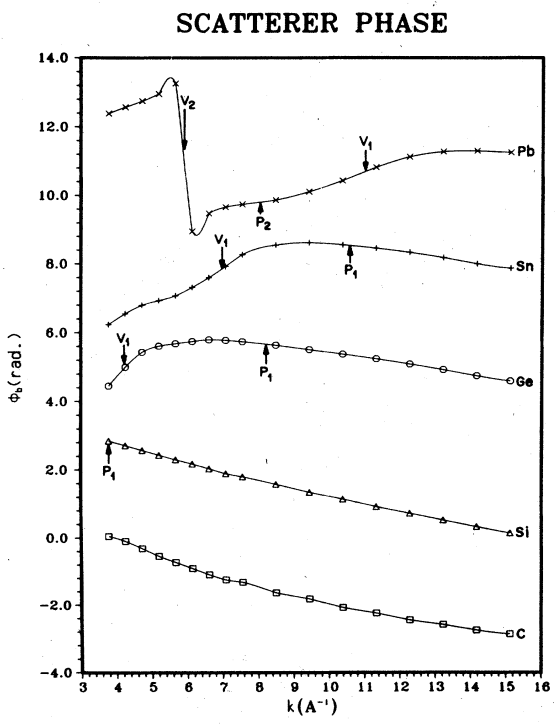

FIG. 8. Phase of the backscattering amplitude $\phi(k)$ (from Teo and Lee, 1979).

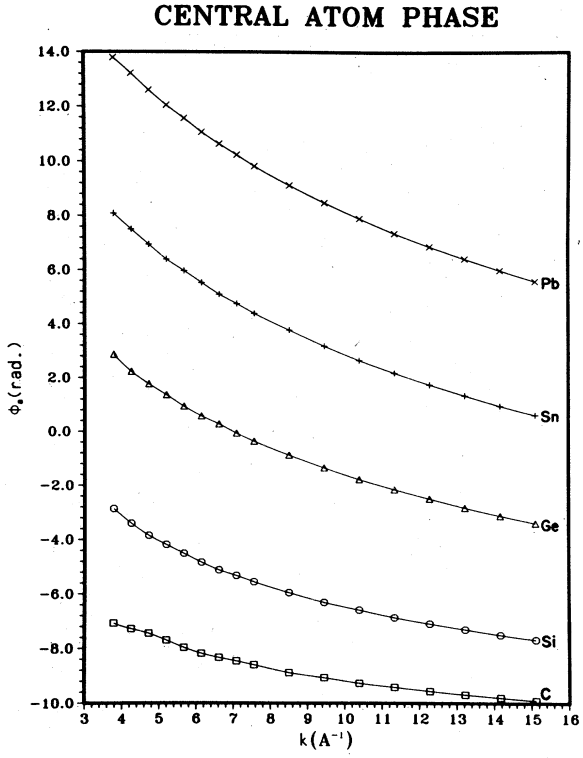

FIG. 9. Central-atom phase shift $\phi_a = 2\eta$, for excitation of an s core state. (from Teo and Lee, 1979).

bonding effects which have already been ignored.

The time dependence of the core potential in metals due to screening was very recently studied by approximating the photoelectron as a classical point charge (Noguera *et al.*, 1979). It was found that the screening time is a fraction of the plasmon period. A comparison of Al EXAFS with the calculated phase shift based on an unscreened ion shows deviation below $k \sim 6$ Å^{-1} (Fontaine, Lagarde, Raoux, and Esteva, 1979), which was interpreted as a crossover between a screened and an unscreened potential. It is desirable to perform this comparison using empirical phase shifts for Al atoms in a nonmetallic environment, since the calculated phase shift may not be very reliable at such low energy.

F. Choice of threshold energy E_0 and chemical transferability of phase shifts

We now have most of the ingredients for comparing calculated phase shifts with experiment. Before doing this, however, the data must be converted to k space, and this requires a knowledge of the threshold energy E_0. As an example for discussing this question, consider the absorption edge of Br_2. Its most prominent feature is a sharp spike separated from the absorption continuum by a few eV. The spike is attributed to the excitation from the $1s$ core level into the unfilled $4p$-derived antibonding molecular orbital of the Br atom. The binding energy of this state relative to the vacuum has been calculated to be 13 eV (Kincaid and Eisenberger, 1975). It has been pointed out by Parratt (1939) that similar structures observed in Ne can be interpreted in terms of the binding energy of the $Z+1$ atom, since the extra nuclear charge can play the role of the core hole. Applying these ideas to Br, the binding energy of the unfilled excited state should equal the ionization potential of Kr, which is 14 eV. These considerations serve to locate E_0 at roughly 14 eV above the excited state. Of course these estimates are uncertain because the chemical bonding of the Br_2 molecule (or more precisely, the Kr-Br system) has been completely ignored.

The existence of a well-defined excited state in Br_2 actually makes it one of the more favorable cases for choosing an appropriate E_0. In most solids, particularly metals, such a bound state does not exist. The understanding of the absorption edge is, in general, very complicated because of its sensitivity to the valence electron distribution. Thus, there is always an uncertainty of at least a few eV in determining E_0.

At this point it is appropriate to review the approximations that have entered into the calculation of the phase shifts. They are

(i) approximate spherical waves by plane waves,
(ii) ignore chemical bonding between the central atom and the scatterer,
(iii) approximate treatment of core relaxation.

Approximation (i) is actually unnecessary. It has been possible to compute the backscattering factor using spherical waves (Lee and Pendry, 1975). The results, of course, depend on the bond length. For Cu it was found that for the second shell the spherical wave calculation is well approximated by the plane wave, while for the first shell deviation of the order of 20% in the amplitude is observed for $k < 5$ Å^{-1}. It was found by Pettifer (1979) that the spherical wave correction to the amplitude appears to extend out to increasing k for increasingly heavy atoms. There are corrections to the backscattering phase $\phi(k)$, as well, but the corrections decrease smoothly for increasing k. Approximations (ii) and (iii) introduce similar errors. Explicit calculations show that different treatment of the valence electrons modifies the phase shift increasingly less with increasing k. The uncertainty in E_0 has exactly the same qualitative feature, and is in fact related to approximation (ii). It is then natural to use E_0 as a single adjustable parameter to incorporate all the approximations listed above. In Fig. 10 we show the central-atom phase shift for Cu calculated using two different atomic configurations to simulate difference chemical environments. The phase shifts are indeed different, reflecting the change in potential. However, by shifting E_0 by 1.9 eV it is possible to bring the two phase shifts into agreement with each other. In many ways the errors introduced by ignoring chemical bonding are similar to the change in the empirical phase shifts when atom pairs are in different chemical environments. The idea of chemical transferability of phase shifts permits the use of phase shifts extracted from one system to be used in the EXAFS analysis of a different system. The accuracy of the transferability was demonstrated by Citrin *et al.* (1976) and is discussed in Sec. IV.

In Fig. 11 we compare the theoretical and experi-

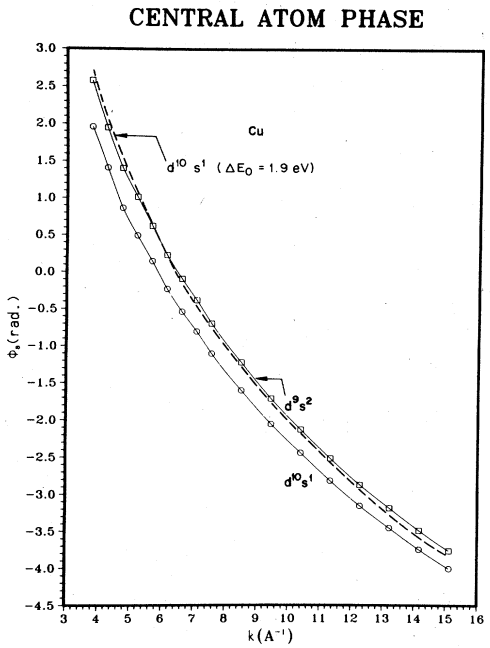

FIG. 10. Central-atom phase shift $\phi_a = 2\eta$, for copper, calculated using two atomic configurations. By a shift of E_0 of 1.9 eV the $d^{10}s^1$ result is shifted to the dashed line, which is in good agreement with the d^9s^2 results (from Teo and Lee, 1979).

mental EXAFS for Br_2. The only adjustable parameters are E_0 and the absolute magnitude. The bond length and the Debye-Waller factor are taken from independent measurements. The agreement is very satisfactory. E_0 is chosen to be 7 eV above the first allowed bound state, and is not too far off from the 13–14 eV discussed earlier. Similar agreement has been obtained for a variety of single-distance molecules. Application to crystalline solids involving more than one neighbor shows that reasonable agreement is obtained for a relatively open structure like Ge, provided the inner

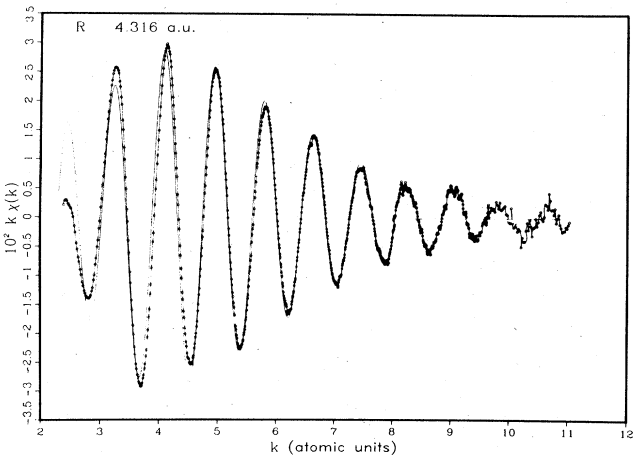

FIG. 11. Comparison between experimental EXAFS spectrum for Br_2 after background removal (dots) and theory (solid line). Theory curve stops at $k = 8$ Å^{-1}. The overall magnitude and threshold energy E_0 are the only two adjusted variables (from Lee and Beni, 1977).

potential is properly taken into account (Lee and Beni, 1977).

G. Inelastic effects and amplitude transferability

To achieve the comparison shown in Fig. 11 it was necessary to multiply the theory by a factor of 0.62. A recent remeasurement of the Br_2 absorption by Stern, Heald, and Bunker (1979) shows that the originally reported experimental amplitude (Kincaid and Eisenberger, 1975) may be too small due to corrosion of the window in the sample chamber. This changes the correction factor from 0.62 to 0.79. Inelastic processes originating in the vicinity of the neighboring atom have in principle been taken into account in the theoretical amplitude. The remaining inelastic processes that take place in the central atom are of the following two types. The first is the possibility of excitation of the central atom by the photoelectron. Since the central-atom potential is also complex, we have to replace $\delta_l'(k)$ in the phase factor $\exp[-2i\delta_l'(k)]$ by a complex phase shift $\delta_l'(k) = \delta_{l,\mathrm{Re}}'(k) + i\delta_{l,\mathrm{Im}}'(k)$. This leads to an overall factor of $\exp[-2\delta_{l,\mathrm{Im}}'(k)]$, which for the case of Br ($l = 1$) is of the order of 75%. The second type of inelastic process occurs in the creation of the core hole. It is known that the energy distribution of the photoelectron shows an "elastic" peak corresponding to leaving the atom in its completely relaxed ground state. The weight of this peak is about 74% in Ne (Meldner and Perez, 1971) and about 62% in Br_2 (Bomben *et al.*, 1980). At lower photoelectron energies there are shake-up and shake-off peaks corresponding to leaving the ion in an excited or doubly ionized state. Most of this weight is distributed in a broad continuum which extends ~40 to 140 eV below the completely relaxed peak. The contribution of the inelastically scattered photoelectrons to EXAFS will be effectively smeared out. Thus the calculated amplitude requires a reduction factor before it can be compared with the normalized experimental spectrum (Lee and Beni, 1977; Rehr *et al.*, 1978). This reduction factor can be calculated from the overlap of the atomic function with that of the ion,

$$S_0^2 = \int d\mathbf{r}_1 \cdots d\mathbf{r}_{N-1} \phi'(\mathbf{r}_1 \cdots \mathbf{r}_{N-1}) \phi(\mathbf{r}_1 \cdots \mathbf{r}_{N-1}), \tag{3.29}$$

where ϕ' and ϕ are the many-electron wave functions for the $N-1$ electrons in the ion and in the atom, respectively.

We should point out that it is incorrect simply to add these two types of inelastic processes. The final states are in fact the same, and the amplitude, not the probability, should be added. This is one reason why a quantitative calculation of the reduction factor over the entire energy range is difficult. A second reason is that inelastic processes involve excitation of the valence electrons and a more sensitive dependence on chemical bonding is expected. An understanding of the absolute EXAFS amplitude is clearly important if EXAFS is to be used to determine coordination number. In the case of Br_2 it has been found (Stern, Heald, and Bunker, 1979) that the reduction factor is relatively energy in-

dependent above $k = 8$ Å^{-1} and is close in magnitude to the overlap factor of 0.78 calculated for Br_2 molecule using Eq. (3.29) (Martin and Davidson, 1977). In view of the above discussion and the uncertainties in the calculated amplitude (see Sec. III.F), the agreement is so good that it is probably fortuitous. Indeed, a recent study on a variety of materials indicates deviations of the order of 20% in the calculated amplitude at low k from the data (Stern *et al.*, 1980).

At this point it is worthwhile to write down a generalization of Eqs. (3.22) and (3.24) for the EXAFS formula for s-core excitation,

$$\chi(k) = -\sum_j \int d\mathbf{r}_j 3(\epsilon\cdot\mathbf{r}_j)^2 S_0(\mathbf{k}) S_j(\mathbf{k}) S_{0j}(\mathbf{k}) N_j |f_j(k,\pi)| \frac{G(\mathbf{r}_j)}{kr_j^2} \sin[2kr_j + \psi_j(k)]. \tag{3.30}$$

The inelastic loss factors are $S_0(\mathbf{k})$, associated with the central atom, $S_j(\mathbf{k})$, associated with the neighbor j [it is crudely included in Lee and Beni's calculation of $f(k,\pi)$ by their use of a complex potential], and $S_{0j}(\mathbf{k})$, associated with the medium between the central atom and the jth neighbor. The spherical wave correction (Sec. III.F) may also be included in this factor. Clearly the separation into these three components is not rigorous. Furthermore, since each factor is an unknown function of k, and since S_{0j} is an unknown function of r_j, Eq. (3.30) is too general to be useful. It does, however, serve as a starting point for approximate treatment and emphasizes our ignorance of the amplitude function and its sensitivity to the chemical environment. In Sec. III.D we discussed the simplifications when $G(\mathbf{r}_j)$ is assumed to arise from a harmonic potential. In that case the integral over $\mathbf{r}_j$ is replaced by a Debye-Waller factor $\exp(-2\sigma_j^2 k^2)$. We also discussed corrections when the harmonic approximation fails. The factor $S_0(k)$ is expected to deviate from a constant below 200 eV, but its precise form is not known and presumably depends on the chemical environment. The factor $S_{0j}(k)$ is often approximated by $\exp[-r_j/\lambda(k)]$. Since inelastic losses in the medium are dominated by low-lying excitations in the system (plasmons, interband transitions, etc.), this factor is expected to be dependent on the chemistry. Stern *et al.* (1980) have suggested writing $S_{0j}(k)$ as $\exp[-r_j - \Delta)/\lambda(k)]$, where Δ is of the order of the nearest neighbor distance. By studying crystals with two components, e.g., CuBr, and analyzing the first and second nearest neighbor of Cu and Br, Stern *et al.* extracted $\lambda(k)$, the ratio of $S_0(k)$ between Br and Cu, and a similar ratio of $|f(k,\pi)|$. Their overall conclusion is that the amplitude is in general not transferable between chemically different species. A similar picture emerges from an independent study by Eisenberger and Lengeler (1980). These questions are further discussed in Sec. IV.F.

H. Structure determination using calculated phase shifts

The good agreement between experimental and theoretical phase shifts suggests that it should be possible to predict distances from calculated values. Results of such predictions (Lee and Beni, 1977) show that single nearest-neighbor distances can generally be obtained with ~0.01 Å accuracy. This accuracy is at first sight surprising and we should pause to examine why it is possible. Suppose that there exist errors in the calculated phase shift due to errors in the potential of 10 eV. The difference in phase shift $\Delta\psi(k)$ can be estimated by making an E_0 change of 10 eV. It is easy to see that $\Delta\psi(k) = 0.2$ rad for $k = 16$ Å^{-1}. Now if we use only the data at $k = 16$ Å^{-1} to extract a distance, the error in that distance is only $\Delta r = 0.2/2k = 0.006$ Å. Clearly the error is more serious for smaller k. However, by making E_0 an adjustable parameter, we can compensate for the errors in the potential and make the phase shift error small for a large range in k. The important point is that changes in E_0 produce changes in $\psi(k)$ which decrease like $1/k$, whereas errors in distance cause changes in $\psi(k)$ which increase linearly with k. By adjusting E_0 it is not possible to produce an artificially good fit of the data with the wrong distance.

The phase shifts and amplitude functions have been computed and tabulated for both the K and L shells of a large number of elements in the Periodic Table (Teo and Lee, 1979). In earlier papers (Teo *et al.*, 1977; Lee *et al.*, 1977) some of these phase shifts have been parametrized. It is to be emphasized that the parametization is intended to be correct only for $k > 4$ Å. In general, it is preferable to work with the tabulated functions rather than the parametrized ones.

I. Near-edge structure

From the point of view of structural determination, the data near the edge are generally ignored because their interpretation is complicated by multiple scattering and chemical bonding effects. On the other hand, precisely because the near-edge absorption structure contains information about the chemical environment, it is receiving increasing attention. While the study of near-edge structure in general has a long history, the improved experimental capabilities discussed in Sec. II have made possible the study of a much broader range of systems. The systematics of the edge shift with chemical environment have been studied by Shulman *et al.* (1976), Cramer, Hodgson, Gillum, and Mortenson (1978), Lytle *et al.* (1979), and Huang *et al.* (1979). Recently, the edge structure has been used to measure the fractional valence in the mixed valence systems TmSe (Launois *et al.*, 1980) and SmS alloyed with Y (Martin *et al.*, 1980). On the theoretical side, Muller *et al.* (1978) have calculated the 4*d* transition metal absorption edge structure based on band theory, i.e., no distinction was made between the potential of the excited atom with the core hole and the surrounding atom. A different approach based on the extension of the X_α cluster method to the continuum states (Dehmer and Dill, 1976) has been applied to the calculation of the near-edge structure in small molecules like $GeCl_4$ (Natoli *et al.*, 1980). The results were found to be sensitive to the treatment of the molecular po-

tential. Reasonable agreement with experiments on $GeCl_4$ was achieved with a particular recipe for the construction of the potential.

IV. EXAFS ANALYSIS

In this section we deal with the analysis of EXAFS data. Given a set of data and the basic EXAFS equation (1.1), there are clearly a large number of approaches for extracting distances and information about the phase shifts, the amplitudes, and the Debye-Waller factors. One of the earliest analyses (Sayers *et al.*, 1971) was based on the Fourier transform of the data expressed in momentum space. The absolute value of the transform was found to peak at distances shifted from the known values by several tenths of angstroms. By correcting for these shifts using systems with known distances, Sayers *et al.* extracted bond lengths. However, this method is not very accurate because the peak value of the Fourier transform depends in general on such factors as the weighting of the data and the choice of the threshold energy E_0 and because the phase shift $\psi_j(k)$, which is largely responsible for the shifted Fourier peak, is not a linear function of k. In their studies of simple molecules dominated by a single distance, Citrin *et al.* (1976) extracted the phase function $\psi_j(k)$ by direct curve fitting to Eq. (1.1) to show that these functions could be transferred to other simple systems to extract bond lengths with an accuracy of 0.01 to 0.02 Å. This approach, however, is not generally applicable to systems of more than one principal distance. The two methods of Fourier transform and curve fitting have been combined to analyze more complicated systems. The curve fitting is carried out either in Fourier space (Hayes *et al.*, 1976) or in k space by backtransforming as described in this section. We provide here a relatively detailed account of this latter data analysis method, which has been successfully applied to a large variety of systems. The principle of chemical transferability of phase shifts that was established for simple systems (Citrin *et al.*, 1976) is illustrated for more complex cases such as GeO_2 crystal. The question of resolving more than one bond length within the first coordination shell is then discussed, illustrated by the analysis of the protein rubredoxin. Finally, the problem of analyzing complicated systems containing several different bond lengths and atomic species is discussed using the analysis of hemoglobin as an illustrative example.

A. Background removal

Fig. 1 shows the absorption spectrum of crystalline Ge at a temperature of 100 K. The structure of Ge is well known and serves here only as an example of our analysis procedure. The modulations above the K edge near 11 keV are due to the EXAFS $\chi(k)$ from several shells of neighboring atoms adding together. The first step in the analysis is to isolate $\chi(k)$ from the total absorption coefficient data $\mu(E)$. Since the smooth absorption of an isolated atom $\mu_0(E)$ is not generally available experimentally and since present theoretical calculations of $\mu_0(E)$ are not sufficiently accurate for most EXAFS work (~0.01%), it is assumed that the smooth part of $\mu(E)$ represents the desired $\mu_0(E)$. Under this assumption, the remaining oscillatory part of $\mu(E)$ is used as $\Delta\mu = \mu(E) - \mu_0(E)$ to give $\chi(k) = \Delta\mu(E)/\mu_0(E)$.

One method for removing the background is to fit $\mu(E)$ (including the EXAFS) with polynomial splines or B splines (de Boor, 1968, 1972; Fox *et al.*, 1976) using a least-squares procedure. A polynomial spline or B spline is a function defined over a series of intervals with each interval containing a polynomial of some order. The ends or knots of the intervals are tied together such that the function and a specified number of derivatives are continuous across the knots. By specifying the number of intervals and the order of the polynomials a very flexible function can be defined. A least-squares fit with such a spline function readily enables the removal of low-frequency background components from $\mu(E)$ without affecting the higher frequency EXAFS oscillations. Since the number of degrees of freedom of the function is controllable, changes in the background removal can be easily tested for their effect on the EXAFS part of the data. Spline fitting is essentially a local fitting procedure in that the polynomial function within each interval is mainly determined by the local quality of the fit. In our analysis only the first derivative is required to be continuous, so the global requirement of continuity across the knots is rather weak. This enables the spline-fitting method to deal with a variety of slowly varying bumps and valleys in the background.

Other background removal methods that have been tried, such as a single polynomial fit over the whole range of the data, iterative low-order polynomial fitting combined with fitting the EXAFS, orthogonal polynomial fitting, Fourier transform filtering, and extrapolation of an assumed functional form of the background from below the absorption edge, all suffer in that a single bad data point, or noise, or end point effects can introduce systematic errors.

B. The E_0 problem

Since $\chi(k)$ in Equation (1.1) is a function of k and not photon energy, k must be computed from the experimental values of photon energy $\hbar\omega$, using

$$k = \left(\frac{2m(\hbar\omega - E_0)}{\hbar^2}\right)^{1/2}, \tag{1.3}$$

where E_0 is the threshold energy. There is no simple relation between features in the experimental spectrum and E_0 as defined by Eq. (1.3) because near threshold various complicated physical processes—chemical bonding effects, core relaxation, etc.—come into play. Several workers have fixed E_0 arbitrarily at a special feature in the spectra (such as a point of inflection) for both the model and the unknown systems and then have proceeded with the analysis (Hayes *et al.*, 1976; Cramer, Hodgson, Steifel, and Newton, 1978). If there is good reason to believe that the model system is chemically very similar to the unknown system, this procedure may yield accurate bond-length determinations. However, in general, in dealing with unknown systems, there is no *a priori* criteria for determining when a model system is sufficiently "similar." There is

clearly a problem if the model and unknown systems have different valences or ionicities. Such difficulties are easily avoided by making E_0 an adjustable parameter in the analysis. As discussed in Sec. III.F, the adjustment of E_0 compensates for the inadequacies of the simple EXAFS formula and permits the use of a wide range of model compounds or calculated phase shifts in the determination of distances.

Fig. 12(a) shows the EXAFS modulation after converting from $\hbar\omega$ to k and removing the smooth background using a spline fit. In Fig. 12(b) the curve has been multipled by k^3. This factor cancels one power of k in Eq. (1.1) and roughly cancels the $1/k^2$ behavior of $|f_j(k,\pi)|$ at large values of k. The k^3 multiplication has the effect of weighting the EXAFS oscillations more uniformly over the range of data starting at about $k=4$ Å^{-1}, corresponding to a photoelectron energy of about 60 eV above the edge. This step is important in preventing the larger amplitude oscillations from dominating the smaller ones in determining the interatomic distances, which depend only on the frequency, not the amplitude of the $\sin[2kr_j+\psi_j(k)]$ function in Eq. (1.1). Also, the k^3 weighting assures that chemical effects on the EXAFS information, which are most significant at small k, are effectively cut off. One variation of the k^3 multiplication factor that has been used (Ashley and Doniach, 1975; Lee and Beni, 1977) is to divide the experimental data in Fig. 12(a) by a theoretical calculation of $|f_j(k,\pi)|$. In principle, this should exactly equalize the EXAFS oscillations if the Debye-Waller and inelastic loss factors are also correctly included in the division.

C. Fourier transform filtering

The next step in the analysis is a Fourier transform. This isolates the contributions of the different shells of neighbors and allows the use of filtering techniques to remove much of the noise and to study each shell separately. It is possible to use curve-fitting techniques for extracting information from the unfiltered data (see Secs. IV.G and IV.H). In general, however, this is difficult because of the noise in the data, the large number of variable parameters needed, and their unavoidable correlations, which can lead (Tullius *et al.*, 1978), to false minima in the fit and misinterpretation of the results.

Fig. 13 shows the magnitude of the Fourier transform of the $k^3\chi(k)$ data in Fig. 12(b). The curve was generated by first interpolating the nonuniformly spaced data onto a uniformly spaced k mesh and then extending the data by adding 0's to a range from $k=0$ to about $k=150$ Å^{-1}. The extended data are then Fourier transformed using a fast Fourier transform algorithm (Cooley and Tukey, 1965, Rabiner and Rader, 1972). The effect of the added zeros is equivalent to transforming only the original data and then applying an interpolation formula to the resulting transform. The large peak at ~2.2 Å is the contribution from the first shell of four Ge neighbors at a distance of 2.45 Å. The Fourier transform peaks at an apparently lower distance due to the effect of the phase shift $\psi_j(k)$. Other smaller peaks visible above the noise correspond to more distant neighbors.

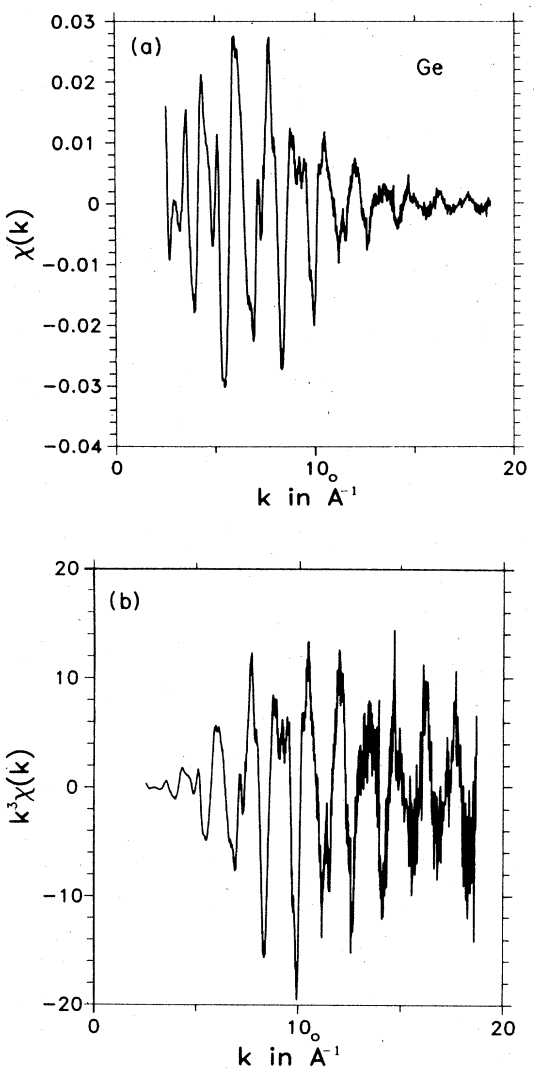

FIG. 12. (a) $\chi(k)$ derived from Fig. 1 by removing a smooth background using a polynomial spline fit. Photon energy $\hbar\omega$ has been converted to k using Eq. (1.3). (b) Data in Fig. 12(a) after multiplication by k^3. This multiplicative factor roughly equalizes the amplitudes of the EXAFS modulations.

The dashed line in Fig. 13 is a smooth filter window function for isolating the first shell EXAFS. The filter is shown applied to the magnitude of the transform, but in fact both the real and imaginary parts of the Fourier spectrum are filtered identically, so that a phase error is minimized. The essential feature of a good filter window function is that it does not produce gross distortions in the data, and almost any smoothly varying function satisfies this requirement. After filtering, the inverse transform is performed to give the solid curve in Fig. 14. Note the absence of all higher frequency variations and noise. Also note that the number of true degrees of freedom in the data has been reduced; this must be taken into account in later analysis of the filtered data. It should also be kept in mind that some amount of distortion is unavoidable in the filtering process and tests on known functions typically show that the first and last oscillations in k

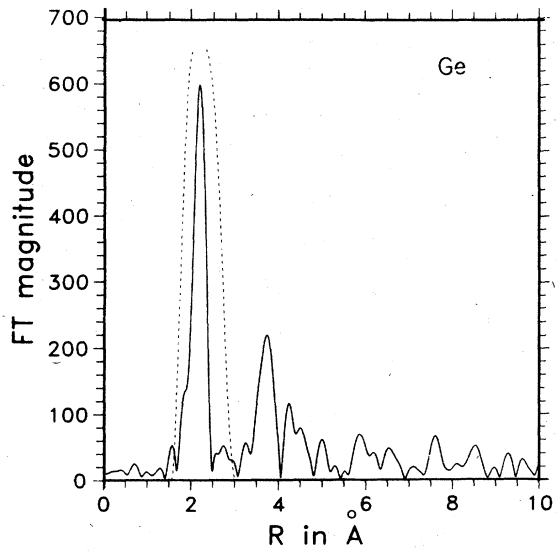

FIG. 13. Magnitude of the Fourier transform of the curve in Fig. 12(b). The transform was obtained using the fast Fourier transfrom algorithm with added 0's to produce a smoothly interpolated curve. The dashed line is a smooth window function used to filter out the first-neighbor shell EXAFS from the noise and higher-order shells.

space are most distorted by Fourier filtering.

An additional point that must be emphasized here is that while the magnitude of the Fourier transform shown in Fig. 13 looks like the radial distribution function $g(r)$, this is most definitely not the case. The major peaks do correspond to shells of neighboring atoms, but the Fourier transform is only a modified version of the true radial distribution function. Equation (1.1) can be generalized for the case of a continuous radial distribution function to give

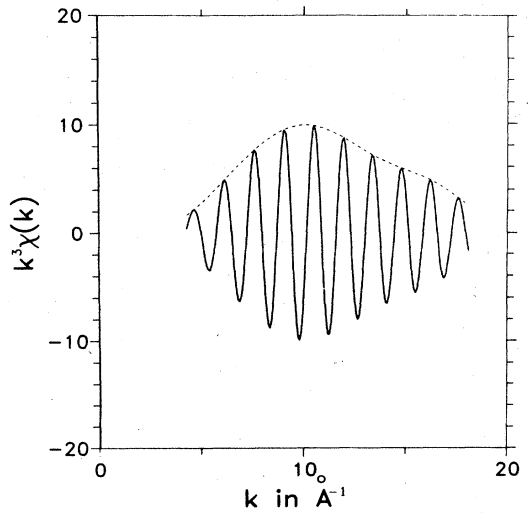

FIG. 14. Inverse transform of Fourier transformed data in Fig. 12(b) after multiplication by window function. Note that all higher frequency noise and higher-order shells have been removed. Dashed curve is the amplitude function derived using the Fourier transform.

$$\chi(k) = -\int_0^\infty \frac{g(r)}{kr^2} \sin[2kr + \psi(k)]\,dr\,. \tag{4.1}$$

Here the inelastic and Debye-Waller factors have been dropped since they are already included in $g(r)$. In addition, $|f(k,\pi)|$ has been assumed to be unity with only one kind of atom pair in the system, so that only a single $\psi(k)$ is needed. Hence, $\chi(k)$ is given by a modified Fourier transform of $g(r)$. If $\psi(k)$ is either known in advance or can be assumed to be closely approximated by a straight line, and if $\chi(k)$ is known for values of k from 0 to ∞, inversion of Eq. (4.1) to get $g(r)$ is possible. In real data, however, k covers only the range from $k_{\min}$ about 3 or 4 Å^{-1}, to $k_{\max}$, usually no more than about 16 Å^{-1}. Only an approximation of $g(r)$, i.e., one which has been effectively low-pass and high-pass filtered in k, can be calculated. The lack of high-k information limits the resolution of the Fourier transform and later analysis, and the absence of low-k information filters out all slowly varying components in $g(r)$ as a function of r. As already mentioned in Sec. III.D, this can produce very peculiar results in the EXAFS study of amorphous materials or other systems with a large amount of thermal disorder (Eisenberger and Brown, 1979; Hayes *et al.*, 1978a, 1978b). In particular, it is found that EXAFS can predict a *shrinkage* of interatomic distances with increasing temperature rather than the actual thermal expansion, along with a *decrease* in the number of nearest neighbors by as much as an order of magnitude. This is due to the fact that the shape of the radial distribution function changes as the temperature (or disorder) is increased. Since EXAFS "sees" only the more sharply peaked or rapidly varying (large-k) parts of $g(r)$ and since thermal expansion is due to an increase in width and a distortion of $g(r)$ due to anharmonic terms in the interatomic potential, only the more ordered part of the distribution, which is the part at shorter distances, is observed in the EXAFS spectrum. The area under the $g(r)$ curve in this close-approach region decreases with increasing temperature, so the apparent coordination number determined by EXAFS also decreases.

D. Decomposition into amplitude and phase

The Fourier transform has the ability to decompose a sine wave into a unique amplitude and phase function. This is done by the following method. Given an arbitrary amplitude modulated sine wave

$$z(k) = A(k)\sin\Phi(k)\,, \tag{4.2}$$

where $\Phi(k)$ is written in place of $2kr + \psi(k)$, we can rewrite $z(k)$ as

$$z(k) = \frac{1}{2i} A(k) e^{+i\Phi(k)} - \frac{1}{2i} A(k) e^{-i\Phi(k)}\,. \tag{4.3}$$

If $z(k)$ is Fourier transformed to $Z(r)$ and if $z(k)$ is sufficiently bandlimited in r (guaranteed by filtering), then the $e^{+i\Phi(k)}$ term in Eq. (4.3) corresponds to positive r values and the $e^{-i\Phi(k)}$ term to negative ones. If, before transforming $Z(r)$ back to $z(k)$, the negative r part of $Z(r)$ is replaced by zero, then the resulting inverse transform produces

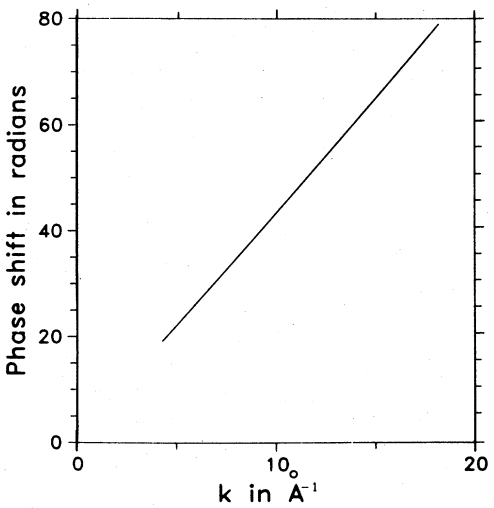

FIG. 15. Total phase $2kr+\psi(k)$ of the sine wave in Fig. 14 produced by Fourier transform decomposition. This curve looks like a straight line because $2kr$ is much larger than $\psi(k)$.

$$\hat{z}(k)=\frac{1}{2i}A(k)e^{+i\Phi(k)}. \tag{4.4}$$

It is then a simple matter to extract $A(k)$ and $\Phi(k)$ as

$$A(k)=2|\hat{z}(k)|, \qquad \Phi(k)=\arg[\hat{z}(k)]+\frac{\pi}{2}. \tag{4.5}$$

The amplitude function derived in this way is the dashed envelope curve in Fig. 14. The phase function $\Phi(k)$ is shown in Fig. 15.

E. Empirical phase shifts and chemical transferability

The phase function contains two terms, $2kr_j$ and $\psi_j(k)$. In order to determine r_j we clearly must first know $\psi_j(k)$. Recall from Sec. III that $\psi_j(k)$ is the sum of the phase shifts associated with the absorbing hole-state atom and the neutral backscattering atom(s). Theoretical work has been done to calculate the absorbing atom and the backscattering phase shifts separately, whereas the EXAFS experiment always measures the sum. In what follows we describe an empirical procedure for using these *total* phase shifts from EXAFS data to demonstrate the concept of chemical transferability. This idea states that at sufficiently high photoelectron kinetic energies, typically above 50 eV where EXAFS scattering processes are dominated by core electrons, phase shifts are insensitive to chemical environment. Determination of $\psi_j(k)$ for an atom pair in a given model system of known distance r_j^m enables the determination of distance r_j^u in an "unknown" (i.e., different) system containing the same atom pair.

We start with the first nearest-neighbor distance in the model system of crystalline Ge to determine the Ge-Ge distance in the unknown system of molecular digermane, Ge_2H_6. The hydrogen atoms are very weak electron scatterers and thus contribute negligible EXAFS; in essence, digermane may be considered a diatomic germanium molecule. The EXAFS data of Ge_2H_6 are analyzed using the same procedures described so far for polycrystalline Ge, namely, removing the background, multiplying by k^3, Fourier filter, and separating the amplitude and phase. The phase function obtained for Ge_2H_6 is $\Phi^u(k')=2k'r^u+\psi^u(k')$, where r^u is the distance to be determined and the prime notation indicates the possibility of a k scale different than that for polycrystalline Ge. The next step is to take the difference between the model and unknown phase functions, $\Phi^u(k')-\Phi^m(k)$. This is plotted in Fig. 16(a) as a function of k, where the solid line is

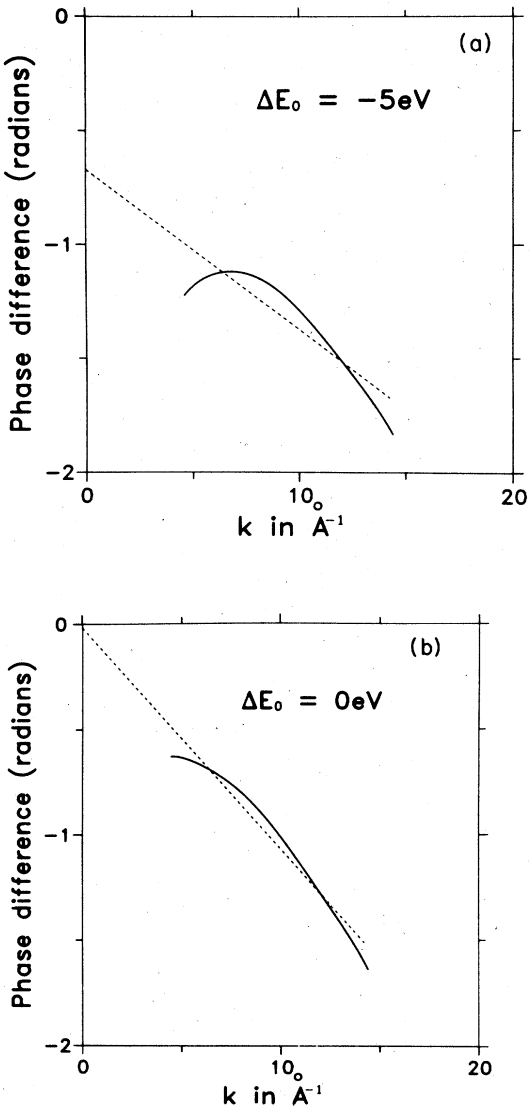

FIG. 16. (a) Demonstration of chemical transferability using total phase shifts from "model" and "unknown" systems, in this case crystalline Ge and gaseous Ge_2H_6, respectively. ΔE_0 has been deliberately set 5 eV too low to demonstrate that the extrapolated straight-line fit to the phase difference (dashed line) does not pass through the origin, indicating apparent violation of the assumption of phase-shift transferability. (b) Here ΔE_0 has been set to 0, and the phase-difference fitted line does pass through the origin. The value of r derived here for the "unknown" system (Ge_2H_6) agrees very well with the known distance.

the phase difference and the dashed line is a linear least-squares fit to the difference. E_0 has been chosen 5 eV lower than the best value. As a consequence, the extrapolated dashed straight-line fit does not pass through the origin, which it would have had the correct value of E_0 been used (and assuming chemical transferability to be valid). In Fig. 16(b) E_0 has been adjusted so that the extrapolated straight-line fit does pass through the origin. The slope of the straight line is then simply $2k(r^u - r^m)$. Using the known first nearest-neighbor distance of $r^m = 2.450$ Å in Ge the analysis predicts a value of $r^u = 2.398 \pm .002$ Å for Ge_2H_6. This result compares very favorably with the interatomic distance of $2.405 \pm .005$ Å determined from electron diffraction. As already emphasized in Sec. III.H the procedure of varying E_0 is valid because changes in E_0 affect mainly the low-k part of the phase shift, while changes in r affect the high-k part, i.e., the two parameters E_0 and r are not strongly correlated. The fact that the analysis predicts distances accurately is taken as a strong indication that chemical transferability is indeed a viable concept. A closely related analysis method of varying E_0 until the "slope" $[\Phi^u(k) - \Phi^m(k)]/k$ remains constant over a large range of k has been used successfully by Martens *et al.* (1978a). The k^{-1} factor weighs the low-k data more heavily than in our method, but Martens *et al.* compensate for this by cutting off low-k information, thus making the two methods roughly equivalent.

It is important to consider the *precision* of the results determined by our analysis procedure. The quoted error bars of ± 0.002 Å represent the precision of the linear least-squares fit only. (Systematic errors, which affect the *accuracy* of the result, are not included in this error; these are discussed separately below.) The estimated error in the least-squares fit is determined by two factors, the size of the phase residuals in the fit and the number of truly independent data points in the phase difference curve. The phase residuals for the fit shown in Fig. 16(b) are given in Fig. 17. From this figure a qualitative assessment

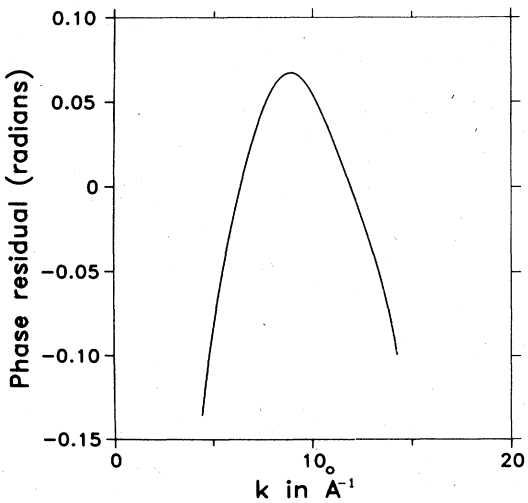

FIG. 17. Plot of phase residuals from Fig. 16(b). The size of the residuals, along with other systematic errors, determines the error bars for the distance value.

of the precision of the fit can be determined simply from $\Delta r = \Delta\psi/2k$. At $k = 10$ Å^{-1}, for example, and a mean value of $\Delta\psi = 0.1$ we have $\Delta r = 0.005$ Å. The number of independent points in the phase-difference curve is just the number of degrees of freedom less the number of adjustable parameters in the fit (Bevington, 1969). The former can be estimated from the ratio of the width of the filter window function to the Fourier-transform resolution, which is determined by the length of the data set, $\Delta k = k_{max} - k_{min}$ (Brillouin, 1962):

$$N_{free} \approx \frac{2\Delta r_{filt}\,\Delta k}{\pi} . \tag{4.6}$$

For a filter window width of about 1 Å and a Δk of 12 Å^{-1}, N_{free} is about 7. This result clearly points out the futility of trying to fit filtered data with complicated multiparameter fitting models.

In order to assess the accuracy of the quoted result, systematic errors must be included in the final error estimate. This includes the effects of the various data analysis procedures used, as well as any systematic errors in the data such as non-EXAFS background modulation due to multiple excitations, the presence of other absorption edges, etc. The analysis procedures can be tested by analyzing artificial data with different amounts of noise or other introduced errors. The procedures outlined so far generally introduce no more than about 0.005 Å total systematic error. All this leads to a conservative total error estimate for first shell distances of about ± 0.01 Å for high quality data such as those shown in Fig. 1.

Although solid Ge and gaseous Ge_2H_6 are quite different materials, the above demonstration of chemical transferability cannot be regarded as very demanding, since the model and unknown comparison is made between first nearest-neighbor atoms of very similar covalent character. A more stringent test is to look at a material in which the formal charges of the atom pairs are substantially different from the charge of the model compound. This is the case of GeO_2 crystal, where the Ge atoms are second nearest neighbors and are significantly more positively charged than in Ge crystal. Fig. 18 shows the analogous spectra for GeO_2 as presented in the Ge-Ge_2H_6 comparison. Following exactly the same steps as above (and using the Fourier filter technique to separate out the first nearest-neighbor Ge-O peak), the Ge-Ge distance in GeO_2 is predicted to be 3.150 ± 0.01 Å, in excellent agreement with the value of 3.153 Å determined from x-ray diffraction.

Another illustrative example of transferability is demonstrated for gaseous Br_2 and CBr_4. In the former the atoms are covalently bonded and are separated by 2.283 ± 0.005 Å, whereas in tetrahedral CBr_4 the Br atoms are not directly bonded, have a net negative charge, and are separated by 3.171 ± 0.005 Å. With Br_2 as the model compound and using the Fourier filter technique to remove the Br–C contribution, a Br–Br distance in CBr_4 of 3.165 ± 0.007 Å is predicted, again in excellent agreement with the electron diffraction result. These representative examples lend much credibility to the concept of phase-shift transferability. Ad-

ditional examples of this concept applied to a wide variety of materials (solid, liquid, gaseous, biological, inorganic, etc.) appear throughout this review, especially in Sec. V.

A final comment about the above analysis procedure of varying E_0 to obtain phase-shift transferability is that it is closely related to the Fourier-transform method used by Lee and Beni (1977) in their comparison of theoretical and experimental phase shifts. In their work, $\chi(k)$ was first multiplied by a number of theoretically calculated factors, including $ke^{+2\sigma^2k^2}/|f(k,\pi)|$, and an estimate of the mean-free-path effect. In addition, a factor of $e^{-i\psi(k)}$ was included, also calculated from theory. The resulting curve was then Fourier transformed. As can be seen from Eq. (1.1), these prefactors essentially cancel the amplitude and phase factors for a given $\sin[2kr_j+\psi_j(k)]$ term (if only positive values of r are examined in the Fourier transform), and hence the transform is just that of a simple sine wave from $k_{\min}$ to $k_{\max}$. The imaginary part of the transform,

$$-\mathrm{Im}\int_{k_{\min}}^{k_{\max}} \sin[2kr_j+\psi(k)]e^{-i[\psi(k)+2kr]}dk, \tag{4.7}$$

is just

$$F(r)=\frac{1}{2(r_j-r)}\cos[(k_{\max}+k_{\min})(r_j-r)] \times \sin[(k_{\max}-k_{\min})(r_j-r)]. \tag{4.8}$$

This function is plotted in Fig. 19. Here $k_{\min}$ is 6 Å^{-1}, $k_{\max}$ is 10 Å^{-1}, and r_j is 2.5 Å. These somewhat artificial values serve to illustrate the qualitative features of Eq. (4.8). The dashed line is

$$A(r)=\left|\frac{1}{2(R-r)}\sin[(k_{\max}-k_{\min})(R-r)]\right|. \tag{4.9}$$

This is the magnitude of the Fourier transform. Note that the function $F(r)$ peaks at the proper value of r, in this case 2.5 Å, and that the magnitude peaks in the same place. If instead of the correct $\psi(k)$ an E_0-shifted $\psi(k')$ were used, the two curves would not peak in the same place, in exact analogy with the extrapolated phase difference curve in Fig. 16(a) not passing through the origin. Hence, the matching of the peaks can be used as a way of adjusting E_0. In fact, in some cases the Fourier transform method might be more desirable. Since it is not really necessary to use theoretical values for the phase-shift and amplitude factors, use of empirical functions (such as those in Figs. 14 and 15 after appropriate subtraction of $2kr$) with the transform analysis would have the effect of narrowing the peaks, as well as shifting them to their correct radial positions. Of course, in a system with different kinds of atoms this would only work for those peaks corresponding to shells containing the proper atoms.

F. Amplitude functions

The amplitude function produced by Fourier-transform filtering contains information about the number

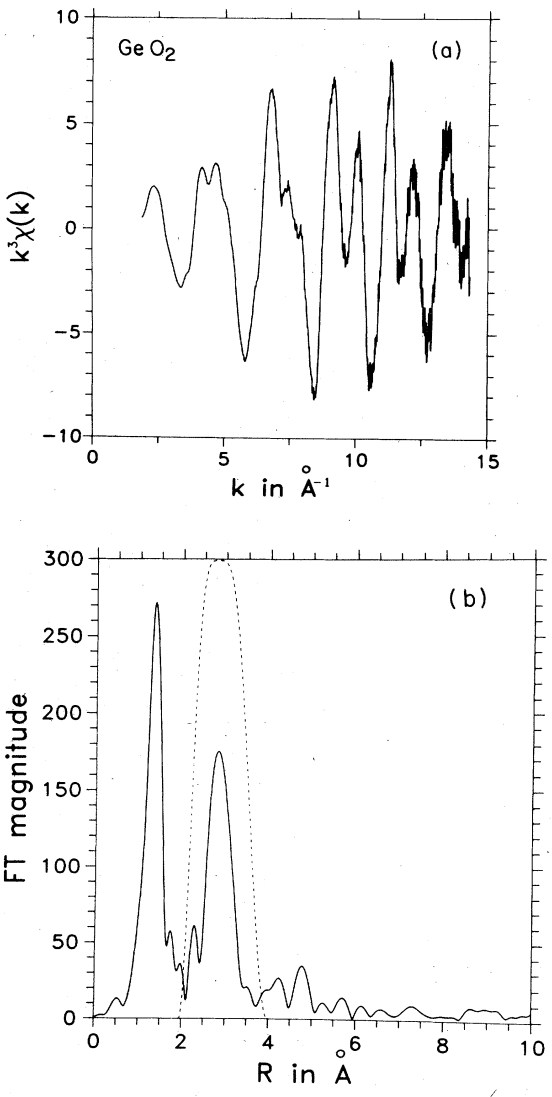

FIG. 18. (a) $k^3\chi(k)$ for crystalline GeO_2. Note the nonsinusoidal nature of the curve, indicating two or more values of r. (b) Fourier transform magnitude for GeO_2. The second peak is the Ge-Ge peak.

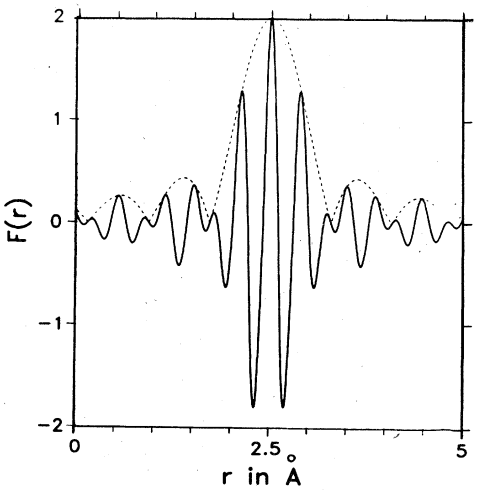

FIG. 19. Plot of $F(r)$ and $A(r)$ from Eq. (4.8) and (4.9) with $r=2.5$ Å.

of nearest neighbors, the kind of atoms involved, the amount of disorder, the effective photoelectron mean free path, and other inelastic and/or intrinsic loss factors. It is possible in principle to extract these quantities assuming chemical transferability of amplitudes, i.e., using model compounds as standards for unknown systems. We discuss below how this is done.

The procedure of amplitude transferability itself is quite straightforward (Stern *et al.*, 1975). Using the simplest expression for $\chi(k)$, Eq. (1.1), the amplitude function for a single shell of N identical atoms is given by

$$A(k) = \frac{N}{kr^2} |f(k, \pi)| e^{-2k^2\sigma^2} e^{-2r/\lambda(k)} . \tag{4.10}$$

Denoting the model and unknown systems by m and u, respectively, the logarithm of their ratio gives

$$\ln\left(\frac{A_m(k)}{A_u(k)}\right) = \ln\left(\frac{N_m}{N_u}\frac{r_u^2}{r_m^2}\right) + 2k^2(\sigma_u^2 - \sigma_m^2) + 2\left(\frac{r_u}{\lambda_u(k)} - \frac{r_m}{\lambda_m(k)}\right) . \tag{4.11}$$

If it is assumed that $\lambda_u(k) \approx \lambda_m(k)$ and $(r_u - r_m) \ll \lambda(k)$, then the third term becomes negligible. A plot of the left-hand term versus k^2, along with the known values of N_m, σ_m, and the quantities r_u and r_m determined from the analysis procedure discussed above, enables the evaluation of N_u and σ_u.

There are several difficulties that can be encountered with this approach. The first involves the empirical determination of $A(k)$. If the data length in k space is too short or if the signal-to-noise ratio is not very high, the amplitude of the Fourier transform will be relatively more affected than will be its phase. The second consideration in using Eq. (4.11) is the relative disorder in the model and unknown systems. As mentioned in Secs. III.G and IV.C a very disordered material can lead to apparently incorrect distances and coordination numbers because of the inability to separate amplitude and phase completely. The third factor is the relative mean free paths in the two systems. Differences of as little as 1–2 Å at a given value of k are actually nonnegligible because of the logarithmic form of Eq. (4.11) (Citrin *et al.*, 1979). The uncertainty of our knowledge of these inelastic loss factors and their sensitivity to chemical environment was discussed in Sec. III.G.

The problems of amplitude transferability have been addressed in recent studies by Eisenberger and Lengeler (1980) and Stern *et al.* (1980). In these extensive studies the transferability between the same and different atom pairs in different structural and chemical environments was investigated. The role of thermal disorder was studied by testing transferability between a given system at 77 K and room temperature. One interesting result is that particularly large discrepancies were observed when the same nearest-neighbor scatterers in different systems were of low Z, i.e., in the first row of the Periodic Table. This is illustrated in Fig. 20, taken from Eisenberger and Lengeler (1980), which shows the amplitude function for the first shell C scatterer in $K_2Fe(CN)_6$, $K_3Fe(CN)_6$, and ferrocene, $Fe(C_5H_5)_2$. Note that the shape of the amplitude function for ferrocene is significantly different in a way that cannot be accounted for by a Debye-Waller factor correction. It was not possible to tell whether the discrepancy was due to $|f(k, \pi)|$ or to inelastic losses in the medium. The situation appeared to improve significantly for nearest neighbor backscatterers in the second row. The procedure outlined in Eq. (4.11) produced first-shell coordination number determinations of better than ±10% in many cases, even though detailed examination of the amplitude functions themselves showed discrepancies below $k = 5$–6 Å^{-1}. Amplitude transferability rapidly broke down for the same atom pairs in different chemical environments when they were not nearest neighbors, e.g., Co-Co in CoO, CoF_2, and CoS_2. Presumably, the loss factor of the medium varied not only in magnitude, but also in k dependence depending on the chemical environment. This conclusion was also reached by Stern *et al.* (1980) (see Sec. III.G). The general picture that emerges from these studies is that unlike phase transferability, many factors can adversely affect amplitude transferability.

In analyzing EXAFS amplitude functions it is often possible to determine the nature of the backscattering atoms. This is best done, of course, when the composition and stoichiometry of the material is already established and when the scatterers (assuming more than one kind) are significantly different in Z. The existence of Ramsauer-Townsend-type resonances (Mott and Massey, 1965) (see Sec. III.D) in the backscattering amplitude functions are particularly helpful for distinguishing between scatterers. In fact, if the atom is sufficiently high in Z (typically $Z > 40$), the Fourier-transformed data exhibit an additional peak at lower values of k. Aside from its usefulness for atom fingerprinting, this peak can complicate the determination of $A(k)$ because its amplitude and position may be sus-

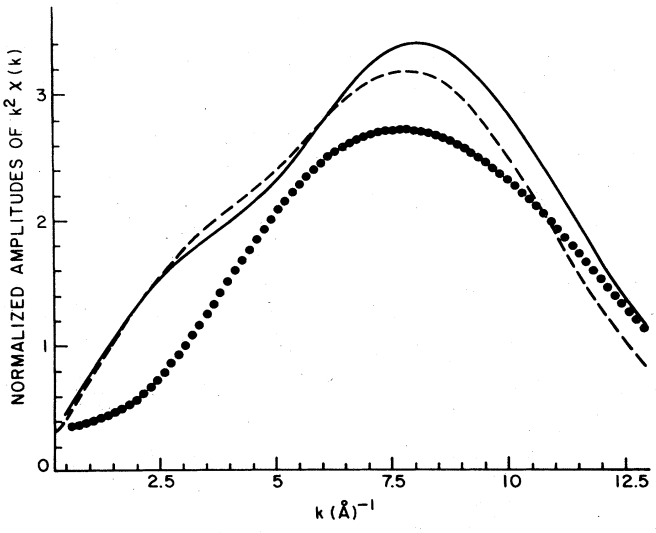

FIG. 20. Backscattering amplitude extracted from the first shell (carbon backscattering) of $K_4Fe(CN)_6$ (solid line), $K_3Fe(CN)_6$ (dashed line), and ferrocene, $Fe(C_2H_5)_2$ (dotted line). All data are taken all at 77K. Normalization is achieved by multiplying $k^2\chi(k)$ by $\gamma^2_{Fe\text{-}C}$ and dividing by the coordination number (from Eisenberger and Lengeler, 1980).

ceptible to such factors as the signal-to-noise ratio, data length, and possible systematic errors in background subtraction. The lower k peak can be filtered out using a smooth window function, with only the absolute magnitude of the amplitude being in error. However, using a model compound containing the same backscattering atoms and applying the same window function, Citrin *et al.* (1978) have shown the relative amplitudes to produce internally consistent results.

Finally, with regard to determining $A(k)$ from the raw data, it should be realized that higher harmonics in the beam can make sample thickness an important fact or in comparing different systems for extracting values of N (Greegor and Lytle, 1980b).

G. Curve fitting: General

Rather than give an extensive discussion of data fitting techniques, something that is often done in the literature, this section reviews some general aspects of curve fitting that have proved useful in EXAFS analysis.

By curve fitting, we mean the solution of the nonlinear least-squares unconstrained minimization problem, that is, finding the best set or vector of parameters $\mathbf{x}$ such that

$$f(\mathbf{x}) = \mathbf{r}(\mathbf{x})^T \mathbf{r}(\mathbf{x}) = \sum_{i=1}^{N} r_i(\mathbf{x})^2 \tag{4.12}$$

is minimized. Here $\mathbf{r}$ is the vector of residuals whose components are given by

$$r_i(\mathbf{x}) = y_i - g(t_i; \mathbf{x}), \tag{4.13}$$

where y_i is the ith data point and $g(t_i;\mathbf{x})$ is the fitting function evaluated at the point t_i with the fitting parameters $\mathbf{x}$. If we write $f(\mathbf{x})$ as a Taylor series expansion about the point $\mathbf{x}_0$ and keep only terms up to second order, we get

$$f(\mathbf{x}) = f(\mathbf{x}_0) + (\mathbf{x} - \mathbf{x}_0)^T \nabla f(\mathbf{x}_0) + \tfrac{1}{2}(\mathbf{x} - \mathbf{x}_0)^T \mathbf{H} (\mathbf{x} - \mathbf{x}_0). \tag{4.14}$$

$\mathbf{H}$ is the Hessian of f, given by

$$\mathbf{H} = \nabla^2 f(\mathbf{x}) = J^T J + \sum_{i=1}^{N} r_i \nabla^2 r_i, \tag{4.15}$$

where the Jacobian matrix $J(\mathbf{x})$ is

$$J(\mathbf{x}) = \frac{\partial r_i(\mathbf{x})}{\partial x_i}. \tag{4.16}$$

If we write the Taylor expansion of Eq. (4.15) around the (possibly not unique) parameter vector μ where the function is minimized, the gradient term vanishes, and we have

$$f(\mathbf{x}) = f(\mu) + \tfrac{1}{2}(\mathbf{x} - \mu)^T \mathbf{H} (\mathbf{x} - \mu). \tag{4.17}$$

Without going into more detail about how actual computer programs find μ given a starting guess, we can notice several interesting things about Eq. (4.17), which is a quadratic approximation to the actual fitting problem. If $\mathbf{x}$ is near μ, then the level curves of f, i.e., the surfaces on which f is constant, are ellipsoids. This is a consequence of the positive definite nature of $\mathbf{H}$ at a true minimum. In general, the principal axes of the ellipse do not lie along the coordinate axes in the N-dimensional parameter space, nor are they necessarily all the same length, which would correspond to a spherical level surface. If λ_i is the ith eigenvalue of $\mathbf{H}$, then it is easy to show that the ith principal axis of the ellipsoid is in the direction of the corresponding eigenvector of H and has a length $\lambda_i^{-1/2}$ (Lanczos, 1956). If the fitting problem is poorly posed, with strong correlations among parameters, then the matrix H is nearly singular. The eigenvectors corresponding to very small eigenvalues are directions along which there is little change in the value of f for relatively large changes in $\mathbf{x}$. The error bars for these linear combinations of parameters are thus very large. In the rubredoxin problem discussed in the next section, the strong correlation between the spread in distances and the Debye-Waller factor is just such a nearly singular behavior. In that case, the correlation is easy to identify since it involves only two out of a small total number of parameters and is readily understood. In more complicated cases, however, the correlation may involve more than just two parameters, and in this situation an examination of the eigenvalues and eigenvectors of H often proves useful. Not only do nearly singular situations show up clearly, but perhaps unsuspected correlations among fitting parameters show up as well. It is highly recommended that this kind of analysis be used whenever nonlinear least-squares curve fitting is attempted (Lawson and Hanson, 1974).

H. Curve fitting: Applications

It is clear that for systems with only a single distance present in each peak of the Fourier transform, the decomposition method described in Sec. III.C is adequate. Therefore the only need for curve fitting is to separate two or more radial distribution function peaks which are not resolved by the Fourier transform technique. Let us consider two shells with radii r_1 and r_2. The sum of two sine waves at different frequencies produces beating in the amplitude with a period of $2k(r_1 - r_2)$. If the data extend to $k_{\max}$ such that

$$k_{\max} \geq \frac{\pi}{2} (r_1 - r_2)^{-1}, \tag{4.18}$$

the minimum in the amplitude as well as the associated kink in the phase-shift function can be measured. Martens *et al.* (1977) have taken advantage of this to resolve the second and third shell distances in CuO which differ by 0.19 Å. They were able to determine the bond lengths with an accuracy of 0.02 Å. However, $k_{\max}$ is typically limited to about 15 Å^{-1} and Eq. (4.18) places a limit on distance resolution of ~0.1 Å. In principle, if the measurements have arbitrarily good signal and noise, and if all the parameters that enter into the basic EXAFS formula are accurate, the resolution of the different distances can be increased. In reality, however, there are limits to how far this can be pushed, and one of the first problems that is encountered in curve fitting is the correlation between various fitting parameters (this was discussed in general terms in the preceding section).

Parameter correlation is illustrated in the study of the Fe-S bond length in the protein rubredoxin (Shulman, Eisenberger, Teo, Kincaid, and Brown, 1978).

It had been reported that of the four Fe-S bonds, one was anomalously short by approximately 0.25 Å (Watenpaugh *et al.*, 1973). From EXAFS measurements it was found that this change in distance, while enormous on the scale of the 0.01 Å accuracy of the single-distance analysis, was small enough to be unresolvable from the three other Fe-S distances using the Fourier transform. Model compounds having Fe-S bonds and crystallographically measured structures were available, and curve fitting was used, showing that there was no anomalously short bond to within about 0.05 Å. Since this small a distance difference is nearly the same as the thermal vibrational amplitude for these bonds, the key role in the electron transfer energetics of the protein postulated for the short bond was ruled out (Shulman, Eisenberger, Teo, Kincaid, and Brown, 1978). However, the curve-fitting problem in this limit of small differences between bond lengths becomes increasingly poorly conditioned, i.e., nearly numerically singular, because a small spread in distances cannot be distinguished from a Debye-Waller factor in a data set of limited length.

To see the reason for the correlation between these two factors, consider the EXAFS spectrum resulting from three long distances and one short distance:

$$\chi(k) \approx \mathrm{Im}(3e^{2ikr_1+\psi(k)} + e^{2ikr_2+\psi(k)}) . \tag{4.19}$$

Rewriting Eq. (4.19) in terms of the mean r and the standard deviation σ of the distribution of distances, we obtain

$$\chi(k) \approx \mathrm{Im}[e^{2ikr+\psi(k)}(3e^{2\sqrt{3}ik\sigma/3} + e^{-2\sqrt{3}ik\sigma})] . \tag{4.20}$$

The term in the inner parentheses represents the modulation introduced by the spread in distances and can be decomposed into amplitude and phase as

$$A(k) = \left[10 + 6\cos\left(8\frac{\sqrt{3}}{3}\sigma k\right)\right]^{1/2} e^{i\Phi(k)} , \tag{4.21}$$

where

$$\Phi(k) = \tan^{-1}\left[\tan^3\left(2\frac{\sqrt{3}}{3}\sigma k\right)\right] . \tag{4.22}$$

Notice that the phase correction due to the spread in distances is of order $(\sigma k)^3$, and so for data with a limited range in k a small σ will produce a very small effect on the phase. Expanding $A(k)$ in Eq. (4.21) for small k, we get

$$A(k) \approx 4(1 - 2\sigma^2 k^2) , \tag{4.23}$$

which is the same to order $(\sigma k)^2$ as $4e^{-2\sigma^2 k^2}$, the Debye-Waller factor. If, however, the signal-to-noise ratio is good enough and the systematic errors in the data analysis are small enough, a curve-fitting program should be able to detect the presence of the higher-order terms in Eq. (4.23) and hence extract more information than just the rms variation from the average distance. The practical limit in the rubredoxin work, though, was the aforementioned 0.05 Å rms determination.

A method of analysis which takes advantage of these facts has been applied to the analysis of rubredoxin EXAFS data (Sayers *et al.*, 1976; Bunker and Stern, 1977). Since the spread in distances shows up in the apparent Debye-Waller factor, it was possible to extract the spread in distances using the procedure described in Sec. IV.F. This involves plotting $\ln[A^m(k)/A^u(k)]$ versus k^2 (m = model, u = unknown), with the extrapolated ordinate being $\ln[N^m r_m^2/N^u r_u^2]$ and the slope being $\sigma_u^2(k) - \sigma_m^2(k)$. In the case of rubredoxin the $\sigma_u(k)$ due to thermal contributions was known, so any differences between $\sigma_u^2(k) - \sigma_m^2(k)$ over and above that due to thermal Debye-Waller factors [$\sigma_m(k)$ is also known] are simply a reflection of the rms spread in distances.

A final example of curve fitting is the study of the protein hemoglobin (Eisenberger *et al.*, 1978), which is one of the more complicated systems analyzed to date. The complexity here lies in the fact that the first peak in the Fourier transform contains three distances, one from the four in-plane porphyrin ring Fe–N bonds (~1.98 Å), one from a single axial nitrogen in the proximal histidine (~2.15 Å), and (in oxy-hemoglobin) one from the oxygen in the bound O_2 molecule (~1.75 Å). The aim was to determine the in-plane Fe-N distance accurately enough to see if there was any strain in the out-of-plane porphyrin ring atoms. Oxygen and nitrogen have similar backscattering amplitudes and, as shown above, a direct curve-fitting approach suffers from correlations between the many parameters required for the fit. Instead, the approach taken made use of the fact that the spectrum is dominated by the four in-plane nitrogen atoms and that the other two distances are almost sufficiently different to be resolved. When the phase curve was extracted from the first Fourier transform peak assuming a single bond length, it was found to contain a small oscillation as expected on the basis of Eq. (4.22). The phase curve was then fitted with a theoretical phase function under the assumption of equal Debye-Waller and loss factors for all three distances and a simple scaling by atomic number of the oxygen and nitrogen backscattering amplitudes. Furthermore, the oxygen and axial nitrogen distances were taken from model systems. The in-plane distance (1.98 ± 0.01 Å) obtained from the fit was found to be relatively insensitive to the assumed out-of-plane distances. This analysis procedure was tested on model compounds and was found to give excellent results. The more general point to be emphasized here is that for complicated systems containing multiple unresolved distances, many parameters must be assumed to be known before any useful information can be extracted.

V. EXAMPLES: STRENGTHS AND LIMITATIONS

There are a number of reviews on the general application of EXAFS (Stern, 1978; Eisenberger and Kincaid, 1978) and reviews with special emphasis on biology (Shulman, Eisenberger, and Kincaid, 1978; Cramer and Hodgson, 1979), chemistry (Sandstrom and Lytle, 1979; Teo, 1980), and catalysis (Lytle *et al.*, 1980). Therefore we shall not attempt to compile a comprehensive list of EXAFS experiments here. Instead, we have chosen a number of examples to illustrate on the one hand the strength and uniqueness of EXAFS as a structural tool, and on the other hand

its limitations. We have made an effort to be constructively critical in our review, and in doing so compare (when possible) EXAFS with other techniques applied to the same problem. At the same time, it is not possible to analyze the potential pitfalls in each individual case without going into excessive details. Thus our remarks are more concerned with pointing out generic problems in a given area of application rather than debating the merits of each individual experiment. The reader who wishes to use the results of an individual experiment may wish to exercise more caution.

Some of the limitations of EXAFS have already been discussed in Sec. IV. For example, while EXAFS typically measures first-shell distances with an accuracy of 0.01 Å, the resolution of different bond lengths is much poorer, of the order of only ~0.2 Å. With much work and in favorable circumstances the limit can be pushed down to ≲0.10 Å, as was done in the example of rubredoxin (Shulman, Eisenberger, Teo, Kincaid, and Brown, 1978). When there is a continuous spread in the distances, such problems become even more severe. This situation is discussed under the general heading of disordered systems. We have up to now concentrated our discussions on bond length determination. In many cases it is of interest to determine both the number and species of neighbors, and this requires an understanding of the EXAFS amplitude. These and other problems will be illustrated by a variety of examples.

A. Disordered systems

One of the earliest applications of EXAFS was to disordered materials. It was recognized that EXAFS can provide information about the immediate environment of an individual atomic species in a multicomponent system, whereas conventional probes such as x-ray or neutron radial distribution function (RDF) studies measure distances between all possible pairs. (Combining x-ray and neutron powder diffraction data or diffraction using anomalous dispersion may overcome this deficiency.) Sayers *et al.* (1975) used EXAFS to study amorphous GeO_2. According to the random network model the glass structure consists of Ge surrounded by four O atoms in a tetrahedral arrangement. The tetrahedra are connected to each other by sharing the oxygen at the corner. By studying the Ge K edge, Sayers *et al.* found that the nearest-neighbor Ge-O bond is similar in the amorphous and crystalline form, whereas the Ge-Ge peak is almost entirely suppressed in the amorphous EXAFS spectrum. This is shown in Fig. 21. Their analysis showed that this could be explained by a disorder parameter $\sigma = 0.077$ Å for the Ge-Ge distance, or a 6.5° fluctuation about the Ge–O–Ge bond angle of 130°. Comparison with RDF studies of the same material shown in Fig. 22 points to both the strength and weakness of EXAFS. [For a review of RDF on glasses, see Wright and Leadbetter (1976).] The RDF showed several sharp structural features out to a radius of 5 Å. On the other hand, O-O distances also appear in the RDF and it is difficult to analyze the structures beyond the first few peaks. The Ge-Ge distance, while very close to the O-O peak, is relatively sharp and resolved.

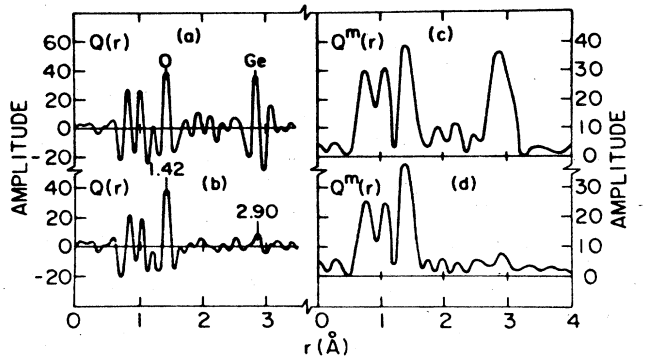

FIG. 21. (a) and (b) are the real part and (c) and (d) the magnitude of the Fourier transform of the Ge edge in crystalline (a, c) and amorphous (b, d) GeO_2 (from Sayer *et al.*, 1975).

To see the reason for the loss of higher shells in EXAFS we assume that the disorder is Gaussian and model its effect by a Debye-Waller type term $\exp(-2\sigma_0^2 k^2)$. The data beyond $k = \sigma_0^{-1}$ are then effectively cut off. Furthermore, since EXAFS data are difficult to analyze for $k \lesssim 3$ Å^{-1} a lower cutoff is usually required in producing the Fourier transform $F(r)$. Thus the amount of data available to a Fourier transform is greatly reduced and the resulting peak height in $|F(r)|$ space is suppressed. The loss of low k information in EXAFS ($k = 3$ Å^{-1} corresponds to the first 6 Å^{-1} in diffraction due to the $2kr$ factor) may limit the usefulness of EXAFS in severely disordered materials, as emphasized recently by Eisenberger and Brown (1979). In general, RDF provides low-k information, while EXAFS provides only the high-k information. This means that EXAFS is more sensitive to short-range (i.e., small r) information, while RDF is sensitive to large r features.

Understanding the effects of disorder played a key

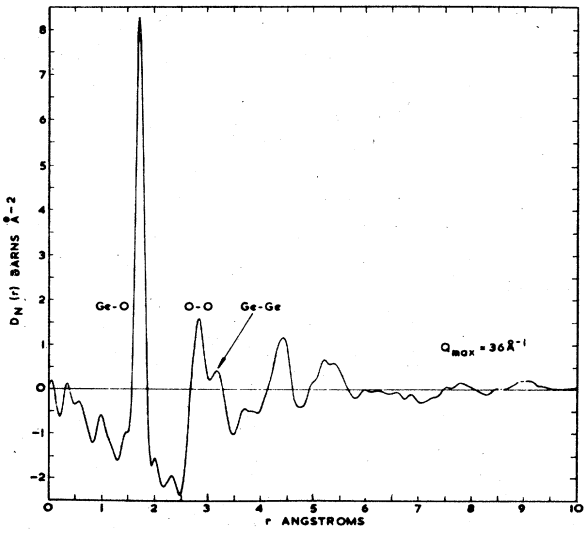

FIG. 22. Radial distribution function for amorphous GeO_2 by neutron scattering (from Sinclair *et al.*, 1974).

role in interpreting EXAFS data on AgI in the superionic phase (Boyce *et al.*, 1977). Fig. 23 shows the Fourier transform of the Ag K edge EXAFS data. The most striking feature is a reduction of the overall amplitude by about a factor of 2 in the superionic phase. In their initial work Boyce *et al.* showed that the models used previously to interpret x-ray and neutron powder diffraction results are inconsistent with the EXAFS data. This illustrates the EXAFS sensitivity and the RDF insensitivity to short-range structural information. The initial studies led Hayes, Boyce, and Beeby (1978) [see also Boyce and Hayes (1979)] to propose an excluded volume model in which the RDF of the iodine atom about each Ag develops a long tail in the superionic phase, in sharp contrast to the usual Gaussian behavior. The long tail provides an explanation of the overall amplitude reduction mentioned earlier. However, while it has been shown that the excluded volume model is consistent with the data, the precise behavior of the long tail cannot be extracted using the EXAFS analysis. Furthermore, no information on the correlation between Ag atoms is obtained. It is interesting to note that RDF analysis, with its greater sensitivity to long-range information, may well provide a more detailed test of the model in the tail region. Neutron diffraction data from single crystal AgI are now available (Cava *et al.*, 1977, 1979). The detailed Ag density map is in agreement with the site occupation proposed on the basis of the EXAFS data.

The above example, together with the studies on Zn at high temperature (Eisenberger and Brown, 1979; Crozier and Seary, 1980) illustrates that in many cases the effective Debye-Waller approximation is inadequate in disordered systems and that one has to resort to modeling to obtain meaningful results. These examples also illustrate that extreme care must be exercised in attempts to determine coordination number using EXAFS. Unless a considerable amount of information is already known about the system, it is not easy to differentiate between a reduction in coordination and an increase in disorder, particularly disorder that cannot be described by an effective Debye-Waller factor. The message here is that whenever possible, EXAFS should be used to complement other structural methods. It is unrealistic to go to a completely unknown and complicated system and expect EXAFS alone to provide the correct answer.

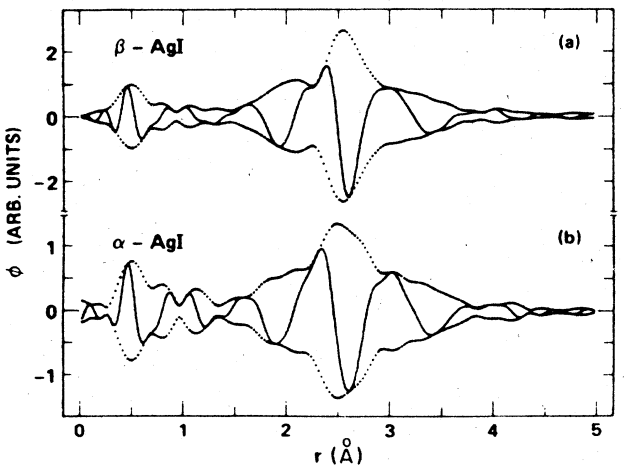

FIG. 23. Real part (solid line) and the magnitude of the Fourier transfrom of the Ag K-edge EXAFS in AgI (a) at 10 °C (normal phase) and (b) at 198 °C (superionic phase). Note the scale change between (a) and (b) (from Boyce *et al.*, 1977).

We mention three other examples of disordered systems where the nature of the nearest-neighbor coordination shell already provides considerable information. The first example is the study on metallic glass by Hayes, Allen, Tauc, Giessen, and Hansen (1978). These authors analyzed the K edge in amorphous $Pd_{0.8}Ge_{0.2}$ and concluded that the Ge atom is surrounded by 8.6 ± 0.5 Pd at a distance of 2.49 ± 0.01 Å with a rms half-width of less than 0.1 Å. They also concluded that there is less than one Ge nearest neighbor, well under the two Ge nearest neighbors expected from a random arrangement of atoms. While a similar picture has emerged from the neutron diffraction studies on $Pd_{0.84}Si_{0.16}$ by Sadoc and Dixmier (1977), Hayes *et al.* argue that a similar diffraction experiment would be difficult for the Pd-Ge system because the Ge–Ge covalent bond length is very close to the Ge-Pd distance.

A second example is a study of the three component chalcogenide glass $As_2S_3Se_3$ (Pettifer, 1979). Using glassy As_2S_3 and As_2Se_3 as model compounds he found that the As edge EXAFS of the ternary system can be fitted by 0.33 ± 0.01 and 0.69 ± 0.02 fraction of Se and S neighbors, respectively. The Se and S backscattering amplitudes and phase are sufficiently different to make this analysis possible. Since we are dealing with relatively heavy Z scatterers as nearest neighbors, amplitude transferability is likely to be applicable in this case (see Sec. IV.F).

A third example is the study of Nb_3Ge film (Brown *et al.*, 1977). Nb_3Ge is the highest T_c superconductor presently known. The material is unstable in the bulk and the transition temperature is sensitive to the method of preparation. Films prepared by sputtering onto a substrate at 1050 K are known to be crystalline $A15$ with a high T_c, while films deposited at 875 K exhibit almost no diffraction lines and have a T_c of ~5 K. EXAFS data showed that the latter samples are characterized by a bond-length reduction of 0.21 Å from the crystalline case and a reduction of the mean coordination number from 12 to 8 ± 2 with only a small change in the effective Debye-Waller factor. Furthermore, data from films produced by electron-beam coevaporation onto sintered microcrystalline Al_2O_3 substrates were interpreted by a superposition of the crystalline and amorphous signals. Thus EXAFS has clearly been helpful in identifying and characterizing the amorphous phase in these interesting materials. On the other hand, T_c is known to change rapidly for deposition temperatures in the vicinity of 1000 K, whereas no change was observed in the Ge-Nb distance determined by EXAFS. Therefore the key question of relative structural information as a function of T_c remains unanswered.

B. Catalysts

1. Supported catalysts

Probably the most complex systems actively under study by EXAFS are supported catalysts. These systems consist of transition metals, typically Pt, Mo, or Ru, which are highly dispersed on a large area silica substrate. The individual clusters are so small that a significant fraction of the atoms is on the surface. Such catalysts have important commercial applications [for an EXAFS review on catalysts see Lytle *et al.* (1980)]. The chemical environment of the dispersed catalyst is of considerable interest and has been studied by following the systematics in the edge structure (Lytle *et al.*, 1979, Gallezot *et al.*, 1979).

One application of EXAFS is simply as a fingerprint to identify the molecules in the course of a reaction. An example of this is the study of the oxidation of a supported Ru catalyst (Lytle *et al.*, 1977). By comparison with Ru metal and RuO_2 standards it was found that exposure to oxygen at 25 °C can be described by chemisorption, whereas at 400 °C bulk oxidation occurred.

A second application of EXAFS is the study of the metallic clusters themselves. While the metal dispersion, defined as the ratio of surface atoms to total atoms in the clusters, can be determined by chemisorption methods (Sinfelt, 1977) and the cluster size distribution can be studied by electron microscopy, there has not been any information on the bond lengths, atomic vibrations, and coordination number of these clusters. EXAFS analysis on a variety of metals such as Os, Ir, and Pt (Via *et al.*, 1979) showed an increase in the Debye-Waller factor typically by a factor of 2 and an average coordination number of $\sim(8-10)\pm2$ compared with the close-packed bulk value of 12. The increased Debye-Waller factor may be due to thermal vibration or static disorder. These effects are consistent with the large fraction of surface atoms in the small clusters. Greegor and Lytle (1980a) have attempted to extract the cluster shape from these data. In view of the correlation between the coordination number and the Debye-Waller factor and the possible deviation from Gaussian distribution in these rather disordered systems (see preceding section), the accuracy of the average coordination number and shape determination must be viewed with some caution at present. Recently, EXAFS work has been extended to bimetallic cluster catalysts (Sinfelt *et al.*, 1980) such as silica-supported Ru-Cu (1 wt. % Ru, 0.63, wt. % Cu). In view of the fact that Cu and Ru have very limited bulk miscibility, the structure of the bimetallic cluster is particularly interesting. Comparison was made between the Ru and Cu edges in the bimetallic system with the pure silica-supported Ru or Cu. The results indicate that Ru is surrounded by 90% Ru and 10% Cu in its first shell, while Cu has about 50% Ru and 50% Cu as neighbors. These results are consistent with a bimetallic cluster consisting of a Ru rich core coated by a thin layer of chemisorbed copper. This picture is confirmed by EXAFS data obtained after O chemisorption, which show that Cu interacts more extensively with O than with Ru. In combination with other techniques (Sinfelt, 1979), EXAFS has greatly increased our knowledge of the microscopic structure of these technologically important catalysts.

Another interesting example of work on metallic clusters is the report of a sizable shrinkage in bond length for small Cu and Ni clusters evaporated on C substrates (Apai *et al.*, 1979) with particle size down to 8 Å. The bond length was found to be reduced by about 10% with a correlated shift in the absorption edge. To assure that the bond-length reduction is a real effect and not an apparent reduction due to the increasing disorder for decreasing cluster size these authors also reported that the phase function was not distorted in the way discussed in Eq. (3.25).

2. Homogeneous catalysts

Reed *et al.* (1977) have made a study of Wilkinson's catalyst, $RhCl(PPh_3)_3$, and polymer-bound Wilkinson's catalyst. The nearest neighbor shell of the Rh in $RhCl(PPh_3)_3$ consists of one Cl and three P atoms. The phase shifts and amplitudes of Cl and P are sufficiently different so that direct curve fitting can be used to extract bond lengths and coordination number. Interestingly, it was found that the polymer-bound catalyst is best fitted by two P neighbors and two Cl atoms. The only reasonable model is that a chloro-bridged dimer is formed when it is attached to the polymer. The dimer formation is correlated with the reduction of catalytic activity of the polymer-bound catalyst. This work was performed on a catalyst supported on a polystyrene crosslinked with 2% divinylbenzene. It is known that the degree of crosslinking has a major influence on the catalytic activity (Grubbs, 1976). In a subsequent study Reed *et al.* (1978) showed that in a catalyst supported on a 20% crosslinked polymer dimer formation was substantially reduced. These studies suggest that there is probably some degree of crosslinking between 2 and 20% which is optimal for the catalytic activity.

C. Solution

It has been possible to obtain EXAFS from ions in solution (Eisenberger and Kincaid, 1975, Crozier *et al.*, 1977, Sanstrom *et al.*, 1977, Sanstrom and Lytle, 1979). The K edge EXAFS measurements for Br in dilute aqueous $CuBr_2$ solution were found to be damped, indicative of a loosely bonded coordination shell of water molecules. Just as in the disordered systems discussed in Sec. V.A, such damping greatly restricts the amount of k space available for determination of distances and coordination numbers. Recently, studies have been carried out in more concentrated solutions (Fontaine *et al.*, 1978, 1980). It has been known from neutron diffraction and Raman spectroscopy that strong Ni-Ni correlation exists in $NiCl_2$ solution. Fontaine *et al.* found that for 4.5 molar concentration of $CuBr_2$ the EXAFS resembles crystalline $CuBr_2$, but with an overall amplitude reduction factor of 2 and with some evidence of O neighbors at low k. They attempted to fit the data without Fourier filtering and interpreted their results as being consistent with ions that are 50%

locally ordered and 50% surrounded by a shell of hydration. The reduction factor of a half is reminiscent of the reduction factor in superionic AgI (see Sec. V.A) and raises questions about the uniqueness of the interpretation. Again we see that while EXAFS permits the immediate identification of short-range ordering, the presence of strong disorder implies that meaningful information obtained from EXAFS of such systems is limited and can be extracted only by modeling.

D. Inorganic chemistry—metal-metal bonds

EXAFS has been used to detect and characterize metal-metal bonds in a number of inorganic complexes. Very often the complexes exist either in solution or in nonsingle crystalline form, so that x-ray diffraction is not possible. An example is the study of Mo(IV) ions in HCl solution. There has been considerable controversy on the question of whether Mo exists in dimer or monomer form. In particular, a structure has been proposed in which two Mo atoms are bridged by two O atoms and each Mo is surrounded by four H_2O molecules. In the EXAFS experiment (Cramer, Gray, Dori, and Binu, 1979), a Mo–Mo bond at 2.51 Å is clearly seen. Furthermore, the spectrum can be fitted with two short Mo–O bonds at 1.95 Å and four long ones at 2.15 Å, the latter presumably arising from the hydration sphere. It is also concluded that Cl is not in the first coordination sphere. The authors are careful to remark that while the EXAFS data are consistent with the dimer model, the correlation between the Debye-Waller factor and coordination number in the fitting procedure does not permit an unambiguous structural determination.

A second example is the study of the Co–Co bond in the neutral and singly ionized complex $[CpCoPPh_2]_2$ ($Cp = \eta^5 - C_5H_5$, $Ph = C_6H_5$) by Teo *et al.* (1978). The structure of the neutral dimer has been determined by x-ray diffraction, but the diffraction has not been successful with the ionized dimer because of air and moisture sensitivity. EXAFS of the neutral dimer was fitted using calculated amplitude and phase functions in a three-term fit (5C +2P +1Co). Upon oxidation the metal-metal bond was weakened to the point that a similar fit for the ionized complex did not give sensible results (this is because the fitting was dominated by the C and P). The data were analyzed with a procedure whereby first a two-term fit with only C and P neighbors was performed and then the difference between that result and the original data was Fourier filtered and fitted by a one-term Co–Co bond. The resulting Co–Co bond length of 2.65 Å (slightly lengthened from 2.57 Å in the neutral complex) was sufficiently different from the Co–C and Co–P bond lengths of 2.07 and 2.22 Å, respectively, to make this subtraction procedure viable (the Co-Co distance was resolved in the Fourier transform of the raw data as a shoulder of the Co-C, Co-P main peak). By this fitting procedure Teo *et al.* (1978) concluded that in addition to the slight stretching, the Debye-Waller factor was increased by roughly $\sqrt{3}$ upon oxidation, so that the metal-metal stretching force constant was interpreted to have decreased by a factor of 3.

E. Defects and impurities

EXAFS should be ideally suited to studies of local distortions around impurities or defects. The use of fluorescence detection, particularly with array detection schemes of the type described in Sec. II (Hastings *et al.*, 1979), should permit measurements of very low impurity concentrations. Such data should be forthcoming in the near future. Here we review two independent studies on Cu precipitates in Al done by Fontaine, Lagarde, Nandon, Raoux, and Spanjaard (1979) and by Lengeler and Eisenberger (1980).

It is known that under proper heat treatment Cu precipitates out of Al-Cu solid solutions in the form of platelets [the Gunier-Preston (GP) zone]. There has not been any technique, however, which directly measures the local structure in the GP zone. The two EXAFS studies arrived at the similar conclusion that Cu precipitates in a single (100) plane and that the d spacing to the neighboring Al plane is contracted to ~1.68 Å compared with 2.0225 Å for the Al matrix. Fontaine *et al.* fitted the data assuming the distance inside the zone to be the nearest-neighbor spacing in the matrix, 2.86 Å, and the composition in the zone plane to be 50% Cu and 50% Al. Lengeler and Eisenberger, on the other hand, allowed the zone plane distance to vary and obtained a best fit at the same matrix spacing of 2.86 Å, thus confirming the conventional picture. This latter work provided an example of the danger of the fitting procedure. These authors' initial data were rather noisy and went out to only $k \sim 11$ Å^{-1}. A best fit to that data disagreed with the conventional picture for a GP zone. Subsequent data taken with greater accuracy and to higher k (15 Å^{-1}) gave a best fit in agreement with the conventional model as discussed above. The danger of false minima in fitting noisy data over a limited k space cannot be overstated. If such situations are unavoidable, it is best to be content with testing the consistency of particular models rather than attempting multiparameter fits.

F. Biology

In many biological systems the active sites are in the vicinity of a heavy metal ion. Conventional diffraction requires the growth of single crystals and solving the structure of extremely large molecules. EXAFS would seem ideal for providing information on the immediate environment of the heavy ion. A special advantage is that crystals are not required and one can often work with solutions of the metalloproteins. In most cases, however, the heavy atoms are very dilute and are responsible for only a small part of the total absorption. Fluorescence detection is usually the preferred measurement technique, and one is often forced to work with spectra of less than ideal signal-to-noise quality. A further complication is that care must be taken to avoid x-ray damage of the biological samples. The best hope for improvement in the experimental situation lies in improvement in the efficiency of the fluorescence detectors. Since the fluorescence radiation is of a given frequency, energy discrimination before detection can separate the signal from unwanted background. Methods

of energy discrimination include use of filters (Stern and Heald, 1979) and use of Bragg diffraction from crystals of graphite (Hastings *et al.*, 1979) or LiF (Marcus *et al.*, 1980).

EXAFS experiments have been performed on a large number of macromolecules of interest to biochemistry [see review by Cramer and Hodgson (1979)]. Our review here is of necessity limited in scope. Experiments in biology can roughly be divided into two groups. The first involves proteins where the ligands of the metal ion are already known from diffraction and EXAFS is used to obtain more accurate bond length and geometry information. We review the work on rubredoxin and hemoglobin as examples of this group. The second group of experiments deals with proteins where some or all of the ligands are unknown and the goal is to determine the coordination number, the bond lengths, and ultimately the local structure. The work on nitrogenase is such an example. In all these studies model compounds play an important role in aiding the analysis and establishing confidence in the results.

Rubredoxin is a small protein of molecular weight 6000 with one Fe atom tetrahedrally coordinated to four S atoms. Prior to the EXAFS work its crystal structure, determined by x-ray diffraction (Watenpaugh *et al.*, 1973), showed three Fe–S bonds at 2.30 Å and a fourth bond at 2.05 Å. The standard deviation of each bond length was 0.045 Å. It was thought that appreciable strain energy was stored in the short bond, thereby affecting the redox potential of rubredoxin. The early EXAFS data on rubredoxin were obtained by transmission detection (Shulman *et al.*, 1975, Sayers *et al.*, 1976). These were moderately noisy and limited to relatively small k, but it was already claimed that the data were inconsistent with a large spread in bond lengths. Careful analysis of improved data obtained by fluorescence detection as described in Sec. IV.H put the difference in bond length at 0.0 ± 0.1 Å (Shulman, Eisenberger, Teo, Kincaid, and Brown, 1978). Furthermore, the average distances determined in oxidized and reduced rubredoxin were found to be the same as those in a model compound not showing an anomalously short bond by either diffraction or EXAFS. Since that time, further refinements of improved diffraction data have yielded an Fe–S bond-length difference of only 0.1 Å. Studies on Fe-S proteins have been extended to other proteins containing two or four Fe atoms, such as ferredoxin (Teo *et al.*, 1979). Since the nearest neighbors include both Fe and S, theoretical amplitude and phase function were used to fit the data. The data analysis procedure was tested on model compounds with excellent results. Comparisons between model compounds and proteins in oxidized and reduced forms show that the models are excellent representations of the active sites of the proteins.

A second biological system under intensive study is hemoglobin. Each hemoglobin molecule contains four active and well separated Fe sites, with each Fe atom surrounded by a prophyrin ring so that it has four N neighbors roughly in a plane. In addition, there is an axial N neighbor that connects the Fe-prophyrin system to the rest of the molecule. Oxygen molecules may be bound to an Fe atom opposite the axial N. However, the binding energy of O_2 on the Fe site may differ by 3 kcal between the high- or low-affinity form of hemoglobin, depending on whether or not one or more of the other Fe sites has already bound an oxygen molecule. Thus, two questions arise which may be answered by EXAFS. First, one would like to know whether there is structural difference localized in the vicinity of the active site between the high- and low-affinity forms of hemoglobin. This question was answered by comparing the EXAFS spectra of a low-affinity hemoglobin with a mutant high-affinity hemoglobin Kemsey (Eisenberger *et al.*, 1976). The Fe–N bond lengths in the prophyrin ring were found to be identical within ± 0.02 Å. A second question relates to the pathway of the remarkable conversion between the low- and high-affinity forms of hemoglobin: How is the binding of O_2 on one Fe site communicated to the other Fe sites? Perutz (1970) and Hoard (1971) have proposed that the Fe is forced out of the plane in deoxyhemoglobin and into the plane in oxyhemoglobin by a shortening of the bond length between the Fe and the planar N upon oxygenation. The motion of the iron was postulated to be as much as 0.7 Å, acting as a "plunger" that communicated the strain energy to the other Fe sites. EXAFS data on both the oxy- and deoxyhemoglobin were obtained (Eisenberger *et al.* 1978). Analysis was difficult because the two Fe-N distances and the Fe–O bond in oxyhemoglobin were unresolved within the first Fourier transform peak. By making use of information obtained from model systems, a rather involved data analysis (see Sec. IV.H) yielded the bond length between the Fe and the inplane N to be 2.055 ± 0.01 and 1.98 ± 0.01 Å for the deoxy- and the oxyhemoglobin, respectively. Using additional information on the relaxed prophyrin ring, the relatively small difference in bond lengths appears to rule out the large-scale motion postulated by Perutz and Hoard as being driven by the lengthening of the Fe–N bond. The lack of bond orientation from the currently available information EXAFS data precludes more detailed structural modeling. The reader is referred to Perutz (1979) for a discussion of his point of view in light of the EXAFS findings.

We now turn our attention to the second group of experiments performed on systems where the ligands of the metal are unknown. A series of measurements on the enzyme nitrogenase illustrates the kind of contribution EXAFS can make in such systems. Nitrogenase is a protein found in nitrogen-fixing bacteria and contains two Mo and approximately 24 Fe atoms out of a total molecular weight of 220 000. It has long been suspected that Mo is the active site of nitrogen reduction. However, information on the local environment of Mo is almost entirely lacking. In a study of both the edge structure and EXAFS of nitrogenase and by comparison with a large class of model compounds, Cramer, Hodgson, Gillum, and Mortenson (1978) concluded that the nearest neighbors of Mo consist of S and Fe. Oxygen ligands were convincingly ruled out. [In contrast, a later study of a different Mo enzyme, sulphite oxidase, showed the presence of both O and S ligands (Cramer, Gray, and Rajagophalen (1979)]. These findings were confirmed by studies on

nitrogenase obtained from different bacteria, as well as from a low molecular weight cofactor containing the Mo-Fe-S complex isolated from the protein (Cramer, Gillum, Hodgson, Mortenson, Steifel, Chisnell, Brill, and Shah, 1978). All of these systems were found to have the same EXAFS spectra. Still further advance was made in the recent synthesis of a model system (Wolff *et al.*, 1978), the structure of which was inferred from diffraction as consisting of Mo substituting Fe in a Fe_4S_4 cube configuration and the Mo atoms in two such cubes being bridged by three S atoms. By comparison of EXAFS of the model system and of nitrogenase, Wolff *et al.* concluded that the local structure of the Mo in nitrogenase is similar to that in the model compound. The EXAFS was analyzed by a curve-fitting procedure by Cramer, Hodgson, Gillum, and Mortenson (1978), who argued that a three-term fit consisting of three Fe neighbors at 2.72 Å, 3 or 4 S atoms at 2.35 Å, and 1 or 2 S atoms at 2.55 Å was required. Unfortunately, the fitting procedure assumed a simple power law for the scattering amplitude $|f(k,\pi)|$, which is known to be inaccurate for heavier elements like Fe and to some extent for S (see Sec. III.E). This is particularly worrisome because the improvement in the fit between a single Mo-S distance and two different Mo-S distances lies mostly at low k where the power law assumption is most inaccurate. This limitation was recognized by the authors, who pointed out that an alternate model consisting of a single Mo bridging two sulfurs cannot be ruled out. Teo and Averill (1979) have produced a variant of this second model consisting of a single Mo bridging two Fe_4S_4 cubes by S ligands. Thus we have seen how EXAFS has greatly enhanced our knowledge of the structure of nitrogenase. Instead of our being totally ignorant about the nature of ligrands, the discussion now centers on the choice between a few structural models. Future experimentation and synthesis of model systems will no doubt narrow the choice still further.

G. Adsorption and intercalculated systems

There has been considerable work on adsorbed atoms and molecules on exfoliated graphite (grafoil). The large surface area of oriented graphite planes has made possible the application of bulk techniques, such as specific heat and x-ray and neutron diffraction, as well as studies of surface properties (Dash, 1978). The system of Br_2 adsorbed on grafoil was studied in some detail by EXAFS as a function of temperature and bromine coverage (Heald and Stern, 1978). It was found that Br_2 is adsorbed as a molecule because a Br backscattering signal was clearly visible. In addition, the C scattering was observed and used to provide information on bond lengths and bonding site. By studying the change in the Br signal when the x-ray polarization is either perpendicular or parallel to the graphite basal plane, Heald and Stern concluded that at 0.6 and 0.9 monolayer coverage the Br_2 molecule lies flat in the basal plane with the Br-Br distance stretched by approximately 0.03 Å to accommodate partially the lattice mismatch. At 0.2 monolayer coverage such anisotropy and stretching was not observed. This they interpreted as an indication that the Br-Br axis is tilted out of the plane and free to rotate. Heald and Stern also studied Br intercalated graphite and Caswell *et al.* (1979) have studied K as an intercalant. EXAFS has provided information on the short-range structure not readily obtained by diffraction. On the other hand, it has relatively little to add to questions concerning long-range order such as order-disorder and commensurate-incommensurate transitions studied in detail by x-ray diffraction for adsorbed rare gases (Stephens *et al.*, 1979).

H. Surface EXAFS

The determination of the location and bond length of adsorbed atoms on clean single-crystal surfaces is an important problem in surface science. The conventional technique for obtaining surface structural information is low-energy electron diffraction (LEED). The analysis of LEED data requires complicated multiple-scattering computer codes, and the accuracy in distance determinations are usually of the order of ±0.1Å (Jona, 1977). It is clear that if EXAFS were observed from the adsorbate, a much more accurate (~±0.01 Å) bond-length determination would be possible. Furthermore, it should be possible to discriminate between adsorption sites by studying either the dependence of the amplitude with synchrotron polarization direction or the nature of second nearest-neighbor distances. The problem, of course, is that a monolayer of adsorbated atoms is an extremely dilute system as far as x-ray absorption is concerned. A surface sensitive detection scheme must be used. The suggestion was made that Auger electrons from the adsorbate be collected and energy analyzed to discriminate against background electrons (Lee, 1976; Landman and Adams, 1976). Because the number of Auger electrons is proportional to the number of core holes created, it is proportional to the absorption by the adsorbate [this is just the nonradiative analog of the fluorescence detection scheme (Jaklevic *et al.* (1977)]. The first surface-EXAFS (SEXAFS) experiments were performed by Citrin *et al.* (1978) on the L_3 edge of iodine adsorbed on Ag(111) by detecting the characteristic I ($L_3M_{4,5}M_{4,5}$) Auger electrons. Alternatively, it is possible to detect the secondary electrons with or without energy discrimination (partial or total yield) (Lukirski and Brytov, 1964; Gudat and Kunz, 1972; Martens *et al.*, 1978b; Stöhr *et al.*, 1978, 1979; Citrin *et al.*, 1979, 1980). For low Z atoms the adsorbate and/or substrate photoemission peaks are swept through the energy analyzer window so that the detection of secondaries is the preferred mode (Stöhr *et al.*, 1978, 1979). In general, there is a trade-off between the high count rate in total yield versus the background discrimination in Auger measurements.

In the $\frac{1}{3}$-monolayer coverage of I on Ag(111), the I–Ag bond length was determined with an accuracy of ±0.03 Å and the adsorption site was assigned to be in the threefold hollow by examination of the SEXAFS amplitude. These results agreed with the earlier LEED work of Forstmann *et al.* (1973) on the same system but were considerably more precise. Since that experiment, the availability of the synchrotron source in dedicated running conditions and the use of

total yield instead of Auger detection schemes has greatly enhanced the signal-to-noise level so that bond-length precisions of ±0.01 Å can now be achieved in even $\frac{1}{4}$-monolayer systems (Citrin *et al.*, 1980). A notable development is the systematic use of the dependence of the SEXAFS amplitude on the synchrotron polarization vector for site discrimination (Citrin *et al.*, 1980). This is illustrated in Table III, in which the effective coordination numbers N_s determined experimentally are compared with theoretical ones for the most probable adsorption sites of I adsorbed on Cu(111) and Cu(100) surfaces. In that table we also list the relative amplitude, i.e., the ratio of N_s for different angles of polarization with respect to the surface. It is found that the use of the relative amplitudes ratio combined with the absolute amplitudes permits unambiguous identification of the three and fourfold hollow sites. Since the chemical environment of the adsorbed atoms is quite different from that of the bulk standards, the application of absolute amplitude transferability alone would be viewed with some caution (see Secs. III.G and IV.F), but as seen in Table III the absolute amplitude offers a comfortable margin in distinguishing between the different high-symmetry adsorption sites. For $L_{2,3}$ edges, in general, the use of relative amplitude functions alone is usually not sufficient because the angularly dependent term in Eq. (3.18) is supplemented by an angularly independent factor. In this regard K edges represent the more favorable case for determining adsorption sites using only relative amplitude functions due to the absence of this isotropic term [see Eq. (3.22)]. Still another aid towards site determination is the measurement of the adsorbate-substrate second nearest-neighbor distance. This has been recently observed in I adsorbed on the quenched Si(111) surface (Citrin *et al.*, 1981). This system is particularly interesting because SEXAFS identified the primary adsorption site as the one-fold on-top site, whereas Cl on similarly prepared Si(111) was found by photoemission to occupy primarily the threefold hollow (Schlüter *et al.*, 1976).

SEXAFS experiments have also been extended to the soft x-ray region, ~0.2–1 keV. Relative to the I experiments at ~4.5 keV, the significantly lower photon fluxes in this energy range due to the current lack of comparably efficient monochromators makes the sensitivity of these measurements much lower and the ability to determine adsorbtion sites much more difficult. Nevertheless, important information can still be obtained. In the study of ~1 monolayer oxygen coverage on Al(111) (Johansson and Stöhr, 1979), not only was the O-Al distance observed, but the adsorbate-adsorbate distance was also seen. The polarization dependence was very helpful in identifying and separating the O-O contribution. The O–Al bond was measured to be 1.75 ± 0.05 Å, substantially different from the value 2.12 ± 0.05 Å given by analysis of LEED data (Martinson *et al.*, 1979, Yu *et al.*, 1980). The LEED study has been criticized by Jona and Marcus (1980) for not having compared a large enough number of beams. On the other hand, these authors also suggest the possibility that the SEXAFS work contained oxygen in a more advanced stage of the chemisorption process (with oxygen inside the substrate). Hopefully the discrepancy can be resolved when higher fluxes are available to enhance the sensitivity at lower adsorbate coverages.

TABLE III. Calculated versus experimental N_s values for I on Cu.

Cu{111}	atop	bridge	hollow	Expt[a]
$\epsilon_{\parallel}$	0.5	1.1	1.7	1.6 ± 0.2
$\epsilon_{\perp}$[b]	1.0	1.8	2.5	3.0 ± 0.6
$\epsilon_{\perp}/\epsilon_{\parallel}$	2.1	1.7	1.5	1.9 ± 0.4
Cu{100}	atop	bridge	hollow	Expt[a]
$\epsilon_{\parallel}$	0.5	1.1	2.4	1.9 ± 0.2
$\epsilon_{\perp}$[b]	1.0	1.8	3.1	2.8 ± 0.6
$\epsilon_{\perp}/\epsilon_{\parallel}$	2.1	1.7	1.3	1.5 ± 0.3

[a] Absolute values of N_s for surface normalized to N_B for bulk polycrystalline model compound CuI.

[b] The nominal perpendicular polarization direction is actually ~70° with respect to the surface plane.

A limitation of SEXAFS compared with LEED is that it appears difficult to apply it to the study of reconstruction of clean surfaces. In this case the signal will be a combination of bulk and surface contributions, making analysis extremely difficult. Bianconi and Bachrach (1979) reported a study on the clean Al(111) and Al(100) faces. Their data extended only to ~50 eV above the edge and consisted of perhaps a single oscillation. This is really not a region in which the EXAFS theory is valid. Their attempt to extract a surface relaxation parameter is not creditable and their conclusion is at odds with LEED work. The LEED conclusion has been confirmed by careful reanalysis (Jona *et al.*, 1980).

With the availability of high-quality data (good S/N and sufficiently large k range), SEXAFS appears to be well on its way towards its development as a major surface structural tool. For well characterized surfaces, there is now sufficient sensitivity for reliable bond-length and site geometry determination for heavy adsorbates. In the near future it should also be possible to extract thermal Debye-Waller factor information. With the development of more efficient monochromators in the soft x-ray energy range and the utilization of dedicated synchrotron sources, studies of low Z adsorbates will be greatly improved and the capabilities for addressing more subtle surface structural questions, e.g., molecular orientation, multiple overlayers and sites, etc., should be enhanced considerably for the full range of adsorbates.

VI. OTHER RELATED TECHNIQUES

There are several other techniques that are closely related to EXAFS. The first is inelastic electron scattering, in which a high-energy electron beam (hundreds of keV in energy) is sent through a thin foil (several hundred Å thick) and the electrons scattered in a given direction are energy analyzed. The differential cross section for such a weak scattering event is given by

$$\frac{d^2\sigma}{d\Omega\, d\omega} = \frac{4r_0^2}{(\hbar q/mc)^4}\, S(q,\omega), \tag{6.1}$$

where $r_0^2 = e^4/m^2c^4$. Here,

$$S(q,\omega) = \sum_{i,f} \left| \left\langle f \left| \sum_j e^{i\mathbf{q}\cdot\mathbf{r}_j} \right| i \right\rangle \right|^2 \delta(\omega_f - \omega_i - \omega). \quad (6.2)$$

The momentum transfer q for particles of incident momentum q_i and for nearly elastic collisions is determined by the scattering angle $q = 2q_i \sin(\theta/2)$.

If $|i\rangle$ is a core state with a radius r_c and $qr_c \ll 1$ (dipole approximation), and if the electrons are independent (Hartree approximation),

$$S(q,\omega) = q^2 \sum_f |\langle f | \hat{\epsilon}_q \cdot \mathbf{r} | i \rangle|^2 \delta(\omega_f - \omega_i - \omega). \quad (6.3)$$

Here $\hat{\epsilon}_q$ is a unit vector in the $\mathbf{q}$ direction. Hence the electron scattering rate is proportional to the optical absorption cross section at frequency ω with polarization $\hat{\epsilon}_q$.

The loss mechanism of interest to us is the excitation of core electrons. Other excitation processes include (i) bulk and surface plasmon losses of energy ranging between 5 and 30 eV, (ii) interband and optical transitions of energy between 1 and 10 eV, and (iii) Cherenkov losses, usually in the 1 to 5 eV range. To avoid losses from these mechanisms, as well as loss of electrons due to elastic scattering at angles larger than the angular acceptance of the electron analyzer, the optimal sample thickness is usually several hundred angstroms. This places rather serious demands on sample preparation. EXAFS has been observed above the Al $L_{2,3}$ edge (Ritsko *et al.*, 1974) and the carbon K edge (Kincaid *et al.*, 1978)—see Fig. 24. Since that time EXAFS has been observed in the K edge of Be, O, Mg, Al, and Si, and the L edge of Si, Ti, Ni, and Cu. Quantitative comparison with theory has been made for C in graphite and Ti in titanium metal (Kincaid, 1980, unpublished).

A comparison between electron energy-loss measurements and absorption using synchrotron radiation was made by Kincaid *et al.* (1978), who concluded that for low Z elements inelastic electron scattering may offer better signal-to-noise. This has been strikingly demonstrated by Batson and Craven (1979), who showed that EXAFS data can be obtained by focusing an electron microscope to a probe size of approximately nanometers in radius, sampling as few as 10^4 atoms in a time as short as four minutes. The use of the scanning electron microscope to perform inelastic energy-loss experiments was recently reviewed by Joy and Maher (1979). Needless to say, the advantages in obtaining synchrotron radiationlike intensities in a lab-sized electron energy-loss machine are substantial.

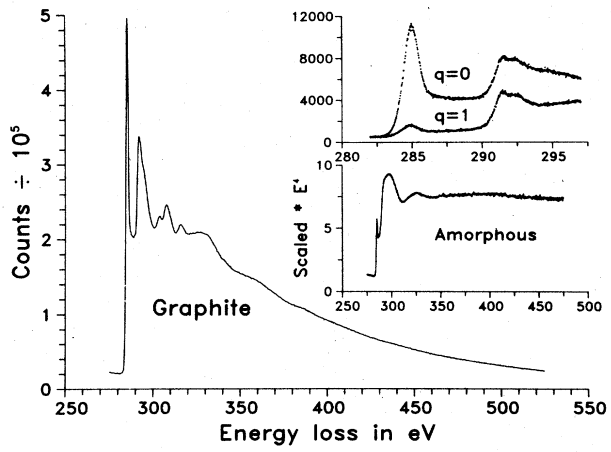

FIG. 24. Electron energy-loss spectra of crystalline graphite. Insert in upper right shows the near-edge structure for momentum transfer $q = 0$ and 1 Å^{-1}. The second insert shows the spectrum for amorphous carbon, scaled by E^4 (from Kincaid *et al.*, 1978).

A second phenomenon that is closely related to EXAFS is the extended appearance potential fine structure (EAPFS). This refers to EXAFS-like oscillations above the appearance potential threshold (Cohen *et al.*, 1978). In this experiment a beam of relatively low-energy electrons (~1 keV) strikes a sample and the total secondary electron yield is monitored as a function of incident electron energy. Above the threshold for excitations of the ($2s$ or $2p$) core states, oscillations are observed in the second derivative spectra. The incident electron with energy E_0 excites a core state with binding energy E_b. The final state consists of a core hole, an electron with energy, E, and an inelastically scattered electron with energy $E_0 - (E_b + E)$. Thus, unlike excitation with photons, the final-state electron does not have a unique energy, and the usual EXAFS expression must be integrated over the final-state energy E. The transition matrix element to each final state should have EXAFS-like oscillations, but the effects will be largely washed out by the E integration. However, there is a relatively sharp lower cutoff on the energy E, namely, it must be above the Fermi level. By looking at the derivative spectra, transitions to electrons with energy just above the Fermi energy can be effectively picked out, thus explaining the oscillations observed. The basic physics is similar to EXAFS except that the dipole selection rule no longer applies in the transition matrix element. A theory of this effect has been worked out by Laramore (1978) and by Laramore *et al.* (1980). Experimental results have been reported on V surfaces (Cohen *et al.*, 1978; Elam *et al.*, 1979) and the Al–O bond in oxidized Al (denBoer *et al.*, 1980). Clearly this technique has the advantage of being surface sensitive and requiring lab-size equipment. Further experimentation and quantitative comparison with theory will no doubt be forthcoming.

REFERENCES

Apai, G., J. F. Hamilton, J. Stöhr, and A. Thompson, 1979, Phys. Rev. Lett. **43**, 165.
Ashley, C. A., and S. Doniach, 1975, Phys. Rev. B **11**, 1279.
Azaroff, L. V., 1963, Rev. Mod. Phys. **35**, 1012.
Batson, P. E., and A. J. Craven, 1979, Phys. Rev. Lett. **42**, 893.
Beni, G., P. A. Lee, and P. M. Platzman, 1976, Phys. Rev. B **13**, 5170.
Beni, G. and P. M. Platzman, 1976, Phys. Rev. B **14**, 9514.
Berreman, D., 1979, Phys. Rev. B **19**, 560.
Bevington, P. R., 1969, *Data Reduction and Error Analysis For the Physical Sciences* (McGraw-Hill, New York).
Bianconi, A., and R. Z. Bachrach, 1979, Phys. Rev. Lett. **42**, 104.

Böhmer, W. and P. Rabe, 1979, J. Phys. C **12**, 2465.
Bomben, K. D., 1980, M. K. Bahl, J. K. Gimzewski, S. A. Chambers, and T. D. Thomas, Phys. Rev. A **20**, 2405
Boyce, J. B., and T. M. Hayes, 1979, in *Physics of Superionic Conductors*, Topics in Current Physics, edited by M. B. Salamon (Springer-Verlag, Berlin), Vol. 15, p. 5.
Boyce, J. B., T. M. Hayes, W. Stutius, and J. C. Mikkelson, Jr., 1977 Phys. Rev. Lett. **38**, 1362.
Brillouin, L., 1962, *Science and Information Theory*, 2nd ed. (Academic, New York).
Brown, F. C., 1974, *Solid State Physics*, edited by H. Ehrenreich, F. Seitz, and D. Turnbull (Academic, New York), Vol. 19, p. 1.
Brown, G. S., L. R. Testardi, J. H. Wernick, A. B. Hallak, and T. H. Geballe, 1977, Solid State Commun. **23**, 875.
Bunker, B., and E. A. Stern, 1977, Biophys. J. **19**, 253.
Caswell, N., S. A. Solin, T. M. Hayes, and S. J. Hunter, 1979, Bull. Am. Phys. Soc. **24**, 375.
Cava, R. J., R. Reidinger, and W. J. Wuensch, 1977, Solid State Commun. **24**, 411.
Cava R. J., F. Reidinger, and W. J. Wuensch, 1979, *Fast Ion Transport in Solid*, edited by P. Vashista *et al.*, (North-Holland, Amsterdam).
Cerino, J., J. Stöhr, N. Hower, and R. Z. Bachrach, 1980, Nucl. Instrum. & Methods **172**, 227.
Citrin, P. H., P. Eisenberger, and B. M. Kincaid, 1976, Phys. Rev. Lett. **36**, 1346.
Citrin, P. H., P. Eisenberger, and R. C. Hewitt, 1978, Phys. Rev. Lett. **41**, 309.
Citrin, P. H., P. Eisenberger, and R. C. Hewitt, 1979, Surf. Sci. **89**, 28.
Citrin, P. H., P. Eisenberger, and R. C. Hewitt, 1980, Phys. Rev. Lett. **45**, 1948.
Citrin, P. H., J. E. Rowe, P. Eisenberger, and R. C. Hewitt, 1981, to be published.
Cohen, P. I., T. L. Einstein, W. T. Elam, Y. Fukuda, and R. L. Park, 1978, Appl. Surf. Sci. **1**, 538.
Cooley, W., and J. Tukey, 1965, Mat. Comput. **19**, 297.
Cramer, S. P., W. O. Gillum, K. O. Hodgson, L. E. Mortenson, E. I. Steifel, J. R. Chisnell, W. J. Brill, and V. K. Shah, 1978, J. Am. Chem. Soc. **100**, 3814.
Cramer, S. P., H. B. Gray, Z. Dori, and A. Binu, 1979, J. Am. Chem. Soc. **101**, 2770.
Cramer, S. P., H. B. Gray, and K. V. Rajagophalen, 1979, J. Am. Chem. Soc. **101**, 2772.
Cramer, S. P., and K. O. Hodgson, 1979, in *Progress in Inorganic Chemistry*, edited by S. J. Lippard (Wiley, New York), Vol. 25, p. 1.
Cramer, S. P., K. O. Hodgson, W. O. Gillum, L. E. Mortenson, 1978, J. Am. Chem. Soc. **100**, 3398.
Cramer, S. P., K. O. Hodgson, E. I. Steifel, and W. E. Newton 1978, J. Am. Chem. Soc. **100**
Crozier, E. D., F. W. Lytle, D. E. Sayers, and E. A. Stern, 1977, Can. J. Chem. **55**, 1968.
Crozier, E. D., and A. J. Seary, 1980, Can. J. Phys. **58**, 1388.
Dash, J. G., 1978, Phys. Rep. **38C**, 178.
deBoor, C., 1968, J. Approx. Th. **1**, 219.
deBoor, C., 1972, J. Approx. Th. **6**, 50.
Dehmer, J., and D. Dill, 1976, J. Chem. Phys. **65**, 5327.
denBoer, M. T., T. L. Einstein, W. T. Elam, R. L. Park, L. D. Roelofs, and G. E. Laramore, 1980, Phys. Rev. Lett. **44**, 496.
Deslattes, R. D., 1980, Nucl. Instrum. Meth. **172**, 201.
Eisenberger, P., and G. S. Brown, 1979, Solid State Commun. **29**, 481.
Eisenberger, P. M., and B. M. Kincaid, 1975, Chem. Phys. Lett. **36**, 134.
Eisenberger, P. M., and B. M. Kincaid, 1978, Science **200**, 1441.
Eisenberger, P., and B. Lengeler, 1980, Phys. Rev. B **22**, 3551.
Eisenberger, P. M., R. G. Shulman, G. S. Brown, and S. Ogawa, 1976, Proc. Natl. Acad. Sci. USA **73**, 491.
Eisenberger, P. M., R. G. Shulman, B. M. Kincaid, G. S. Brown, and S. Ogawa, 1978, Nature, **274**, 30.
Elam, W. T., P. I. Cohen, L. Roelofs, and R. L. Park, 1979, Appl. Surf. Sci. **2**, 636.
Fontaine, A., P. Lagarde, A. Naudon, D. Raoux, and D. Spanjaard, 1979, Philos. Mag. B **40**, 17.
Fontaine, A., P. Lagarde, D. Raoux, and J. M. Esteva, 1979, J. Phys. F **9**, 2143.
Fontaine, A., P. Lagarde, D. Raoux, M. P. Fontana, G. Maisano, P. Migliardo, and F. Wanderlingh, 1978, Phys. Rev. Lett. **41**, 504.
Fontaine, A., P. Lagarde, D. Raoux, A. Sadoc, and P. Migliardo, 1980, J. Chem. Phys.
Forstmann, F. W. Berndt, and P. Büttner, 1973, Phys. Rev. Lett. **30**, 17.
Fox, P. A., A. D. Hall, and N. L. Schryer, 1976, "The PORT Library Mathematical Subroutine Library," Bell Laboratories Computing Science Technical Report No. 47.
Gallezot, P., R. Weber, R. A. Dalla Betta, and M. Boudart, 1979, Z. Naturforschung **34a**, 40.
Golovchenko, J., R. A. Levesque, and P. L. Cowan, 1981 Rev. Sci. Instrum. **52**, 509.
Greegor, R. B., and F. W. Lytle, 1980a, J. Catal. **63**, 476.
Greegor, R. B., and F. W. Lytle, 1980b, Boeing Co. preprint.
Grubbs, R. H., 1976, Strem. Chem. **4**, 3.
Gudat, W., and C. Kunz, 1972, Phys. Rev. Lett. **29**, 169.
Haensel, R., and C. Kunz, 1967, Ann. Rev. Phys. **23**, 276.
Hartree, D. R., R. de L. Kronig, and H. Petersen, 1934, Physica **1**, 895.
Hastings, J., 1977, J. Appl. Phys. **48**, 1576.
Hastings, J. B., P. Eisenberger, B. Lengeler, M. L. Perlman, 1979, Phys. Rev. Lett. **43**, 1807.
Hayes, T. M., J. W. Allen, J. Tauc, B. G. Giessen, and J. J. Hauser, 1978, Phys. Rev. Lett. **40**, 1282.
Hayes, T. M., J. B. Boyce, and J. L. Beeby, 1978, J. Phys. C **11**, 2931.
Hayes, T. M., P. N. Sen, and S. H. Hunter, 1976, J. Phys. C **9**, 4357.
Heald, S. M., and E. A. Stern, 1977, Phys. Rev. B **16**, 5549.
Heald, S. M., and E. A. Stern, 1978, Phys. Rev. B **17**, 4069.
Hedin, L. and S. Lundqvist, 1969 in *Solid State Physics*, edited by F. Seitz, D. Turnbull, and H. Ehrenreich (Academic, New York), Vol. 23, p. 1.
Hedin, L., and B. I. Lundqvist, 1971, J. Phys. C **4**, 2064.
Hoard, J. L., 1971, Science **174**, 1295.
Horowitz, P., and J. A. Howell, 1976, Science **191**, 1172.
Huang, H. W., S. H. Hunter, W. K. Warburton, and S. C. Moss, 1979, Science **204**, 191.
Jaklevic, J., T. A. Kirby, M. P. Klein, A. S. Robertson, G. S. Brown, and P. Eisenberger, 1977, Solid State Commun. **23**, 679.
James, R. W., 1965, *The Optical Principles of the Diffraction of X-Ray* (Cornell University Press, Ithaca).
Johansson, L. I. J., and J. Stohr, 1979, Phys. Rev. Lett. **43**, 1882.
Jona, F., 1977, Surf. Sci. **68**, 204.
Jona, F., D. Sandericker, and P. M. Marcus, 1980, J. Phys. C **13**, L155.
Jona, F., and P. M. Marcus 1980, J. Phys. C **13**, L477.
Joy, D. C., and D. M. Maher, 1979, Science, **206**, 162.
Kevan, S. D., D. H. Rosenblatt, D. Denley, B.-C. Lu, and D. A. Shirley, 1978, Phys. Rev. Lett. **41**, 1565.
Kincaid, B. M., 1980, unpublished.
Kincaid, B. M., 1977, J. Appl. Phys. **48**, 2684.
Kincaid, B. M., and P. Eisenberger, 1975, Phys. Rev. Lett. **34**, 1361.
Kincaid, B. M., A. E. Meixner, and P. M. Platzman, 1978, Phys. Rev. Lett. **36**, 326.
Kono, S., C. S. Fadley, N. F. T. Hall, and Z. Hussain, 1978,

Phys. Rev. Lett. 41, 117.
Kossel, W., 1920, Z. Phys. 1, 119.
Kostarev, A. I., 1941, Zh. Eksp. Theor. Fiz. 11, 60.
Kostarev, A. I., 1950, Zh. Eksp. Theor. Fiz. 20, 811.
Knapp, G. S., H. Chen, and T. E. Kleppert, 1978, Rev. Sci. Instrum. 49, 1658.
Kozlenkov, A. T., 1961, Bull. Acad. Sci. USSR, Phys. Ser. 25, 968.
Kronig, R. deL., 1931, Z. Phys. 70, 317.
Kronig, R. deL., 1932, Z. Phys. 75, 468; 76, 468.
Lagarde, P., 1976, Phys. Rev. B 13, 741.
Lanczos, C., 1956, *Applied Analysis* (Prentice-Hall, Englewood Cliffs).
Landman, U., and P. L. Adams, 1976, Proc. Nat. Acad. Sci. USA 73, 2550.
Laramore, G. E., 1978, Phys. Rev. B 18, 5254.
Laramore, G. E., T. L. Einstein, L. D. Roelofs, and R. L. Park, 1980, Phys. Rev. B 21, 2108.
Launois, H., M. Rawiso, E. Holland-Moritz, R. Pott, and D. Wholleben, 1980, Phys. Rev. Lett. 44, 1271.
Lawson and Hanson, 1974, *Solving Least Squares Problems* (Prentice-Hall, Englewood Cliffs, and EISPACK Library Subroutine MINFIT, Argonne National Laboratory, Applied Mathematics Division).
Lea, K. R., 1978, Phys. Rep. 43, 338.
Lee, P. A., 1976, Phys. Rev. B 13, 5261.
Lee, P. A., and G. Beni, 1977, Phys. Rev. B 15, 2862.
Lee, P. A., and J. B. Pendry, 1975, Phys. Rev. B 11, 2795.
Lee, P. A., B. K. Teo, and A. L. Simons, 1977, J. Am. Chem. Soc. 99, 3856.
Lengeler, B., and P. Eisenberger, 1980, Phys. Rev. B 21, 4507.
Li, C. H., and S. Y. Tong, 1979, Phys. Rev. Lett. 43, 526.
Liebsch, A., 1974, Phys. Rev. Lett. 32, 1203.
Liebsch, A., 1976, Phys. Rev. B 13, 544.
Lukirski, A. P., and I. E. Brytov, 1964 Fiz. Tverd. Tela (Leningrad) 6, 43 [Sov. Phys.–Solid State 6, 33 (1964)].
Lytle, F. W., 1966, in *Advances in X-ray Analysis*, edited by G. R. Malett, M. Fay, and W. M. Mueller (Plenum, New York), Vol. 9, p. 398.
Lytle, F. W., D. E. Sayers, and E. A. Stern, 1977, Phys. Rev. B 15, 2426.
Lytle, F. W., G. H. Via, and I. H. Sinfelt, 1977, J. Chem. Phys. 67, 3831.
Lytle, F. W., H. Via, and J. H. Sinfelt, 1980, in *Synchrotron Radiation Research*, edited by H. Winick and S. Doniach (Plenum, New York).
Lytle, F. W., P. S. P. Wei, R. B. Gregor, G. H. Via, and J. H. Sinfelt, 1979, J. Chem. Phys. 70, 4849.
Marcus, M., L. Powers, A. R. Storm, B. Chance, and B. M. Kincaid, 1980, Rev. Sci. Instrum. 51, 1023.
Martens, G., P. Rabe, N. Schwentner, and A. Werner, 1977, Phys. Rev. Lett. 39, 1411.
Martens, G., P. Rabe, N. Schwentner, and A. Werner, 1978a, Phys. Rev. B 17, 1481.
Martens, G., P. Rabe, N. S. Schwenter, and A. Werner, 1978b, J. Phys. C 11, 3125.
Martin, R. L., and E. R. Davidson, 1977, Phys. Rev. A 16, 1341.
Martin, R. M., J. B. Boyce, J. N. Allen, and F. Holtzberg, 1980, Phys. Rev. Lett. 44, 1275.
Martinson, C. W. B., S. A. Flodström, J. Rundgren, and P. Westvin, 1979, Surf. Sci. 89, 102.
Massey, H. S. W., 1969, *Electronic and Ionic Impact Phenomena* (Oxford University Press, Oxford), p. 692.
Meldner, H. W., and J. D. Perez, 1971, Phys. Rev. A 4, 1388.
Morawitz, H., W. D. Gill, P. Grant, G. B. Street, and D. Sayers, 1979 in *Quasi One-Dimensional Conductors* II, edited by S. Barišić, A. Bjeliš, J. R. Cooper, and B. Leontić (Lecture Notes in Physics, Vol. 96) (Springer-Verlag, Berlin), p. 390.
Mott, N. F., and H. S. W. Massey, 1965, *Theory of Atomic Collision*, 3rd ed. (Clarendon, Oxford).
Muller, J. E., O. Jepsen, O. K. Anderson, and J. W. Wilkins, 1978, Phys. Rev. Lett. 40, 720.
Natoli, C. R., D. K. Misemer, S. Doniach, and F. W. Kutzler, 1980, Phys. Rev. A 22, 1104.
Noguera, C., D. Spanjaard, and J. Friedel, 1979, J. Phys. F 9, 1189.
Parratt, L. G., 1939, Phys. Rev. 56, 295.
Perutz, M. F., 1970, Nature 228, 726.
Perutz, M. F., 1979, Ann. Rev. Biochem. 48, 327.
Pettifer, R. F., 1979, 4th EPS Gen. Conf. 522.
Pettifer, R. F., and P. W. McMillan, 1977, Philos. Mag. 35, 871.
Rabe, P., G. Tolkiehn, and A. Werner, 1979a, J. Phys. C 12, 899.
Rabe, P., G. Tolkiehn, and A. Werner, 1979b, J. Phys. C 12, L545.
Rabiner, L. R., and C. M. Rader, editors 1972, *Digital Signal Processing* (IEEE, New York).
Reed, J., P. Eisenberger, B. K. Teo, and B. M. Kincaid, 1977, J. Am. Chem. Soc. 99, 5217.
Reed, J., P. Eisenberger, B. K. Teo, and B. M. Kincaid, 1978, J. Am. Chem. Soc. 100, 2375.
Rehr, J. J., E. A. Stern, R. L. Maratin, and E. R. Davidson, 1978, Phys. Rev. B 17, 560.
Ritsko, J. J., S. E. Schnatterly, and P. C. Gibbons, 1974, Phys. Rev. Lett. 32, 671.
Sadoc, J. F. and J. Dixmier, 1977, in *The Structure of Non-Crystalline Materials*, edited by P. H. Gaskell (Taylor and Francis, London), p. 85.
Sandstrom, R., H. W. Dodgen, and F. W. Lytle, 1977, J. Chem. Phys. 67, 473.
Sanstrom, D. R., and F. W. Lytle, 1979, Ann. Rev. Phys. Chem. 30, 215.
Sayers, D. E., E. A. Stern, and F. W. Lytle, 1971, Phys. Rev. Lett. 27, 1204.
Sayers, D. E., E. A. Stern, and F. W. Lytle, 1975, Phys. Rev. Lett. 35, 584.
Sayers, D. E., E. A. Stern, and J. R. Herriot, 1976, J. Chem. Phys. 64, 427.
Schaich, W., 1973, Phys. Rev. B 8, 4078.
Schlüter, M., J. E. Rowe, G. Magaritondo, K. M. Ho, and M. L. Cohen, 1976, Phys. Rev. Lett. 37, 7632.
Schmit, V. V., 1961 Bull. Acad. Sci. USSR Phys. Ser. 25, 988; 27, 392.
Sevillano, E., H. Meuth, J. J. Rehr, 1979, Phys. Rev. B 20, 4908.
Shiraiwa, T., T. Ishimura, and M. Sawada, 1958, J. Phys. Soc. Jpn 138, 848.
Shulman, R. G., P. Eisenberger, W. E. Blumberg, and N. A. Stombaugh, 1975, Proc. Natl. Acad. Sci. USA 72, 4003.
Shulman, R. G., P. Eisenberger, and B. M. Kincaid, 1978, Ann. Rev. Biophys. Bioeng. 17, 559.
Shulman, R. G., P. Eisenberger, B. K. Teo, B. M. Kincaid, and G. S. Brown, 1978, J. Mol. Biol. 124, 305.
Shulman, R. G., Y. Yafet, P. Eisenberger, and W. E. Blumberg, 1976, Proc. Natl. Acad. Sci. USA 73, 1384.
Sinclair, R. N., D. A. G. Johnson, J. C. Dore, J. H. Clarke, and A. C. Wright, 1974, Nucl. Instrum. Meth. 117, 445.
Sinfelt, J. H., 1977, Science 195, 641.
Sinfelt, J. H., 1979, Rev. Mod. Phys. 51, 569.
Sinfelt, J. H., G. H. Via, and F. W. Lytle, 1980, J. Chem. Phys. 72, 4832.
Stephens, P. W., P. Heiney, R. J. Birgeneau, and P. M. Horn, 1979, Phys. Rev. Lett. 43, 47.
Stern, E. A., 1974, Phys. Rev. B 10, 3027.
Stern, E. A., D. E. Sayers, and F. W. Lytle, 1975, Phys. Rev. B 11, 4836.
Stern, E. A., 1978, Contemp. Phys. 19, 289.
Stern, E. A., and S. M. Heald, 1979, Rev. Sci. Instrum. 50, 1579.
Stern, E. A., S. M. Heald, and B. Bunker, 1979, Phys. Rev.

Lett. **42**, 1372.
Stern, E. A., B. A. Bunker, and S. M. Heald, 1980, Phys. Rev. B. **21**, 5521
Stöhr, J., D. Denley, and P. Perfetti, 1978, Phys. Rev. B **18**, 4132.
Stöhr, J., L. Johansson, I. Lindau and P. Pianetta, 1979, Phys. Rev. B **20**, 664.
Teo, B. K., 1980, Acc. Chem. Res. **13**, 412.
Teo, B. K., 1981 J. Am. Chem. Soc. **103**, 3990.
Teo, B. K., and B. A. Averill, 1979, Biochem. Biophys. Res. Commun. **88**, 1454.
Teo, B. K., P. Eisenberger, and B. M. Kincaid, 1978, J. Am. Chem. Soc. **100**, 1735
Teo, B. K., and P. A. Lee, 1979, J. Am. Chem. Soc. **101**, 2815.
Teo, B. K., P. A. Lee, A. L. Simons, P. Eisenberger, and B. M. Kincaid, 1977, J. Am. Chem. Soc. **99**, 3854.
Teo, B. K., R. G. Shulman, G. S. Brown, and A. E. Meixner, 1979, J. Am. Chem. Soc. **101**, 5624.
Tullius, T., P. Frank, and K. O. Hodgson, 1978, Proc. Natl. Acad. Sci. USA **75**, 4069.
Via, G. H., J. H. Sinfelt, and F. W. Lytle, 1979, J. Chem. Phys. **71**, 690.
Watenpaugh, K. D., L. C. Sieker, J. R. Herriott, and J. H. Jensen, 1973, Acta Crystallogr. B **29**, 943.
Williams, G. P., F. Cerrina, I. T. McGovern, and G. J. Lapeyre, 1979, Solid State Commun. **31**, 15.
Winick, H., 1980, in *Synchrotron Radiation Research*, edited by H. Winick and S. Doniach (Plenum, New York).
Wolff, T. E., J. M. Berg, C. Warrick, K. O. Hodgson, and R. H. Holm, 1978, J. Am. Chem. Soc. **100**, 4630.
Woodruff, D. P., D. Norman, B. W. Holland, N. V. Smith, H. H. Farrell, and M. M. Traum, 1978, Phys. Rev. Lett. **41**, 1130.
Wright, A. C., and A. J. Leadbetter, 1976, Phys. Chem. Glass Glass, **17**, 122.
Yu, H. L., M. C. Muñoz, and F. Soria, 1980, Surf. Sci. **94**, L184.